Title
High-precision in vivo imaging of the mouse visual pathway by adaptive optical two-photon fluorescence microscopy

Author
Yang, Yuhan

Publication Date
2022

Peer reviewed|Thesis/dissertation

High-precision *in vivo* imaging of the mouse visual pathway by adaptive optical two-photon fluorescence microscopy

by

Yuhan Yang

A dissertation submitted in partial satisfaction of the

requirements for the degree of

Doctor of Philosophy

in

Physics

in the

Graduate Division

of the

University of California, Berkeley

Committee in charge:

Professor Na Ji, Chair
Professor Laura Waller
Professor Oskar Hallatschek

Fall 2022

High-precision *in vivo* imaging of the mouse visual pathway by adaptive optical two-photon fluorescence microscopy

Abstract

High-precision *in vivo* imaging of the mouse visual pathway by adaptive optical two-photon fluorescence microscopy

by

Yuhan Yang

Doctor of Philosophy in Physics

University of California, Berkeley

Professor Na Ji, Chair

Two-photon fluorescence microscopy (2PFM) is a superior alternative to conventional fluorescence microscopy with its higher contrast and deeper tissue penetration. It has become a method of choice for biological imaging of complex samples, such as the mammalian brain. For high-resolution imaging, however, 2PFM suffers from optical aberrations induced by the sample and imaging system, which lead to degraded image quality. Adaptive optics (AO) has been applied to 2PFM to remove these aberrations, hence improving image resolution and enhancing image contrast.

This thesis explores two applications of AO in 2PFM to achieve high-precision imaging of neurons in the mouse brain.

The first application is divergence-based remote focusing (Chapter 2). Capable of imaging through scattering and opaque tissues, 2PFM has been widely applied to three-dimensional (3D) imaging of biological samples. Remote focusing by controlling the divergence of excitation light is a common approach to scan the focus axially. However, changing the beam divergence induces distortion to the excitation wavefront, which leads to an aberrated focus and degraded image quality away from the natural focal plane. To maintain the focal quality, we used indirect-wavefront-sensing-based AO to measure and correct divergence-induced aberrations and achieved diffraction-limited resolution during remote focusing.

The second application is *in vivo* mouse retinal imaging (Chapter 3). The retina, behind the transparent optics of the eye, is the only neural tissue whose physiology and pathology can be non-invasively probed by optical microscopy. The aberrations intrinsic to the mouse eye, however, prevent high-resolution investigation of retinal structure and function *in vivo*. To characterize and correct mouse ocular aberration, we applied direct-wavefront-sensing-based AO to *in vivo* two-photon imaging of the mouse retina. We demonstrated the capability of AO-2PFM in longitudinally tracking structural and functional changes of the mouse retina

with high accuracy. Our method represents an important advancement in microscopic investigation of retinal pathology and pharmacology *in vivo* for disease diagnosis and treatment.

Besides technological developments of AO, this thesis also presents the applications of 2PFM in functional studies of mouse primary visual cortex (V1) and visual thalamus (Chapter 4) with *in vivo* calcium imaging. Measuring the neuronal activities of V1 neurons and their thalamocortical afferents in response to visual stimuli, we investigated the spatial organization of orientation tuning in V1 and found significant tuning similarities among nearby neurons in both L2/3 and L4 of V1.

This thesis is dedicated to the people who support me throughout my educations. I couldn't have seen this adventure through to the end without you.

Contents

List of Figures

Acknowledgments

Foremost, I would like to express my deepest gratitude to my advisor Prof. Na Ji for providing invaluable guidance and help throughout my PhD studies. Her insightful ideas and prompt feedback steered me in the right direction of the research. Specifically, I would like to thank her for her support and encouragement during my transition from academia to industry. I still remember the valuable life changing suggestion she gave me: jump out of the comfort zone. I sincerely appreciate it and am making small steps every day.

I am grateful to all of my labmates and collaborators. Specifically, I would like to thank Dr. Katharine Borges and Dr. Ryan Natan who are the Ji lab's experts in neuroscience. As a physics student, neuroscience was a completely new field to me before I joined the Ji lab. They helped me get started and prepare myself as a neuroscientist. I am also thankful to Dr. Qinrong Zhang and Dr. Wei Chen. They have taught me a lot of knowledge about optics and microscopy. Every discussion with them was inspiring and insightful. I would also like to extent my sincere thanks to Kevin Fan, Anna Yoon, Peijia Yu, Dr. Olivia Gozel and Prof. Brent Doiron, whom I had the pleasure of working with on the projects. I couldn't have made the achievements without their inspiration and help.

Life is not easy as a PhD student. I spent more than twenty years in school to earn the doctorate degree and it's finally paid off. Although I don't become an excellent scientist eventually and have to switch to industry, the scientific training I received and the friends I made during the journey benefit me for a lifetime. Lastly, this amazing adventure could not even be possible without my family. They are my strong backings and support me in any ways. Thank them for always trusting me and being proud of me.

While I did not mention everyone here, I hold appreciation for all who support me throughout my educations. Graduation from PhD is not the end but the beginning of bigger challenges to face. I know I am not alone on the journey.

Chapter 1

Introduction

1.1 Adaptive optical two-photon fluorescence microscopy

Two-photon fluorescence microscopy (2PFM) [1] was developed as a superior alternative to conventional widefield fluorescence microscopy for tissue imaging. Conventional widefield fluorescence microscopy uses visible light to excite fluorescent molecules in the specimen with the emitted photons collected by a camera. Its application has been limited to thin samples such as cultured cells or ultrathin tissue sections. This is because the fluorescence signals generated outside the focal plane of the microscope objective are also detected by the camera, and can overwhelm the in-focus signals in thick samples. More complex technologies, such as confocal [2, 3] and structured illumination [4–6] microscopy, have been developed to eliminate the unwanted background fluorescence in order to achieve optical sectioning. However, their imaging depth and contrast are still limited by light scattering for deep tissue imaging of opaque and highly scattering samples [7, 8].

2PFM avoids these pitfalls by using near infrared (NIR) light for excitation and relying on nonlinear interactions between photons and fluorescent molecules for optical sectioning. In 2PFM, a fluorophore in the sample absorbs two photons simultaneously and emits one fluorescence photon. This nonlinear interaction only happens at a confined region about the focal point. As a result, it suffers much less contamination from out-of-focus signals. Furthermore, using NIR light as the excitation source substantially reduces light scattering. Benefiting from both effects, 2PFM provides higher contrast and deeper tissue penetration [9]. This has made 2PFM a popular technique of choice for applications involving thick biological samples. In particular, 2PFM has become very useful for imaging the brain *in vivo*.

Adaptive optics

Having tackled issues of background fluorescence contamination and light scattering with 2PFM, one remaining challenge is to reduce the image quality deterioration resulting from aberrations of complex samples. Ideally, excitation light is focused to a diffraction-limited spot by the microscope objective and forms a spherical wavefront. However, due to the optical inhomogeneity of complex samples such as mammalian brains, refractive index varies across the imaging volume. This results in an aberrated wavefront, which reduces signal, contrast and resolution. Originally developed by astronomers to fight atmospheric distortion [10–12], adaptive optics (AO) is implemented in 2PFM [13, 14] to counteract these aberrations, hence improving image quality and enhancing image contrast.

A typical AO procedure consists of two steps: wavefront measurement and wavefront correction. Wavefront measurement can be generally divided into two categories: direct (used in Chapter 3) and indirect (used in Chapter 2) wavefront sensing [14–16]. Direct wavefront sensing [17–21] relies on a wavefront sensor, e.g. Shack-Hartmann (S-H) sensor [22, 23], to measure the wavefront distortion. It consists of a lenslet array and a sensor camera. Each lenslet segments the wavefront and focuses light within each lenslet segment into a single spot on the camera forming a SH image of an array of foci. By measuring the deviation of each spot from its aberration-free position, the local phase gradient can be calculated to reconstruct the wavefront. On the contrary, techniques of indirect wavefront sensing characterize aberrations without a dedicated wavefront sensor. Many sensorless AO methods have been developed and applied to a variety of microscopes. These include zonal-based [24–26], modal-based [27–29] and computational methods (e.g. phase retrieval [30, 31] and machine learning [32–34]). Once the aberrated wavefront is known, an opposite corrective wavefront is applied to a wavefront shaping device, such as a deformable mirror (DM) or spatial light modulator (SLM), to compensate for the aberrations.

The effectiveness of AO-2PFM in improving image quality and eliminating out-of-focus signals has been validated in both *ex vivo* and *in vivo* samples. For example, people have compared AO-2PFM with widefield imaging in fixed mouse brain slices (Thy1-GFP line M, Fig. 1.1 [35]). AO improved resolution, signal and contrast of images from both widefield and two-photon imaging. It allowed fine structures such as dendritic spines to be better resolved (Fig. 1.1 A-D). However, due to the lack of optical sectioning in widefield, both in- and out-of-focus signals were enhanced by AO leading to minimal improvements in the contrast (Fig. 1.1 F). In contrast, fluorescence background signals were rejected by 2PFM and therefore not changed substantially after aberration correction (Fig. 1.1 G). As a result, higher resolution and contrast were observed in the two-photon images.

Remote focusing

Because it is capable of imaging through scattering and opaque tissues [9], 2PFM has been widely applied to three-dimensional (3D) imaging of complex samples both *in vitro* and *in vivo*. 2PFM scans the focal point in two dimensions (2D) with a pair of optical scanners

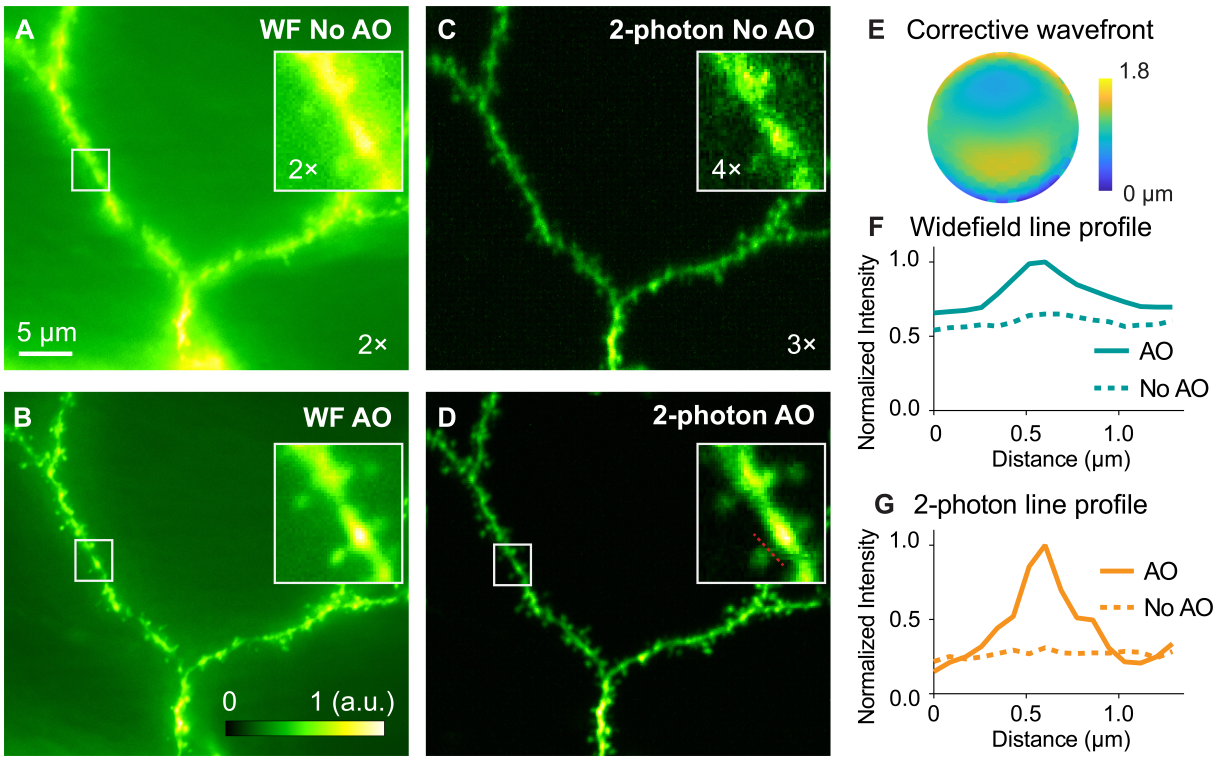

Figure 1.1: Widefield and two-photon imaging of Thy1-GFP line M brain slices (adapted from Li et al. 2020 [35]). (A-D) Maximum intensity projections of 8-μm-thick widefield and two-photon image stacks, taken (A, C) without and (B, D) with AO, respectively. For each pair of images, signal was normalized to the AO condition (0 to maximum intensity of the image with AO). Signal from images without AO was artificially increased for better visualization (ratios shown in each image). (E) Corrective wavefront. (F, G) Line profiles across a dendritic spine neck [red dashed line in (D)]. a.u., arbitrary units.

and records fluorescence signal in each position with a photon detector (typically, a photomultiplier tube). For typical 3D imaging, the excitation focus is shifted axially relative to the sample by translating the microscope objective, and a 2D image is acquired at each axial position. This approach can achieve sub-second volumetric imaging speeds over axial ranges of tens of microns, but is nevertheless limited by the inertia of the objective lens [16]. An alternative method to axially scan the laser focus is to control the divergence of excitation light, which avoids the temporal delay due to inertia from objective motion between successive 2D scans. This divergence-control-based method is called remote focusing.

For high-resolution imaging, however, remote focusing suffers from the fact that microscope objectives are designed to have optimal imaging performance for light of specific divergence. For example, infinity-corrected microscope objectives used for 2PFM only form diffraction-limited excitation focus for collimated beams. As a result, changing the beam divergence induces distortion to the excitation wavefront, leading to an aberrated focus and degraded image quality away from the natural focal plane [36–39]. To maintain focal qual-

ity during remote focusing, many methods have been proposed, e.g. two-objective remote focusing [40–42] and modal-based AO [43]. However, minimal and moderate improvements in image quality were observed with these approaches. In our work [44] (Chapter 2), we applied indirect-wavefront-sensing AO to correct the aberrations induced by divergence-based remote focusing and achieved unprecedented imaging performance for large axial scanning ranges.

1.2 Applications of two-photon fluorescence microscopy in mouse visual pathway studies

Compared to conventional fluorescence microscopes, 2PFM causes less photobleaching and photodamage with the confined focal volume. It provides deep tissue penetration and optical sectioning. With these advancements, 2PFM has become a preferred tool for biological studies both *in vivo* and *in vitro*. Capable of resolving fine structures, such as dendritic spines and axonal boutons, 2PFM has been widely applied to morphological imaging to track anatomical changes of neuronal structures. For example, several studies [45–47] chronically recorded structural changes in synapses by 2PFM to investigate synaptic plasticity in normal and diseased mouse models. 2PFM has also been applied to chronic imaging of blood flow [48–50], neuroglia- neurovasuclar interaction [51, 52] etc. The capability to do longitudinal study of neuronal structures with 2PFM brought us many new discoveries that couldn't be observed from histological studies in fixed tissues.

In addition to morphological imaging, 2PFM is also used in functional imaging of neuronal activity. When the summed synaptic inputs to a neuron reach a threshold level of depolarization, calcium ions flow into the membrane following the opening of voltage-gated calcium channels. Neuronal structures can be labeled by genetically encoded calcium indicators [53–55], which are molecules that change their fluorescence intensity when bound to calcium ions. Neural activity is monitored by recording the fluorescent signals with 2PFM. Compared to electrophysiology recording, calcium imaging with 2PFM [8, 56] offers superior synapse-resolving spatial resolution and the ability to characterize hundreds of neurons with genetically defined cell type.

My PhD research is mainly focused on using 2PFM to study the mouse visual pathway from the retina to the brain both morphologically and functionally. Visual information is extracted by the retina and sent to the central visual system for further analysis. The visual pathway includes lateral geniculate nucleus (LGN) of dorsal thalamus and primary visual cortex (V1). Specifically, my research covers (1) imaging of retinal ganglion cells, microglia and vasculature in the retina; and (2) measuring activity of thalamic boutons and neurons in the V1 in response to external visual stimuli across different behavioral states.

1.2.1 Imaging mouse retina

Retina is a layered tissue of neurons and glia in the back of the eye that transduces light into electrochemical signals to be further processed by the brain for visual perception and cognition [57]. As one of the most energy-demanding tissues, the retina is metabolically sustained by an intricate vasculature with several laminar plexuses [58]. Vascular and neuronal abnormalities in the retina are associated with both ocular [59] and systemic diseases [60–62], underscoring the importance of studying retinal pathology and pharmacology.

Situated behind highly transparent mouse eye optics (i.e., cornea and crystalline lens), the retina is uniquely accessible to light and the only part of the nervous system that can be probed non-invasively by optical imaging. Recent advances in mouse genetics have enabled fluorescence microscopy investigations of vasculature [63] as well as neurons and glial cells [64–66] of the mouse retina. Among fluorescence microscopy techniques, 2PFM is particularly suited for retinal imaging because its intrinsic optical sectioning capability permits depth-resolved 3D imaging throughout the retina. With the retinal photoreceptors minimally responsive to NIR light, 2PFM is also an ideal tool for functional studies of retina [67, 68]. However, as a far-from-perfect imaging system [69], the optics of the mouse eye introduce severe aberrations to the NIR excitation light, preventing high-resolution visualization of subcellular features *in vivo*. In our work, we used AO to correct mouse ocular aberrations, which allowed us to carry out microvascular and cellular investigations of retinal physiology.

1.2.2 Imaging mouse visual thalamus and primary visual cortex

LGN of the thalamus receives visual input from retina and projects this information to V1 via thalamic axons. V1, essential for processing visual information in the neocortex, is divided into six distinct layers (L1 to L6) based on structure and functionality [70]. As the major synaptic target of LGN, L4 in V1 processes the sensory information and passes the output to L2/3. To understand how cortical circuits encode and compute visual information, high-precision measurement of neuronal activity in cortex as well as its thalamocortical afferents in response to visual stimuli are required.

Among all properties of V1 neurons, we are mostly interested in the spatial organization of orientation selectivity (OS). Prior studies have shown that many neurons in the visual cortex respond strongly to bars of a certain orientation, but not as much to the orthogonal orientation. Such tuning properties have been demonstrated in many mammals [71] ever since the first discovery from cat V1 by Hubel and Wiesel in 1963 [72]. In rodents, OS tuning has long been believed to have no clear spatial organization [73], instead forming a "salt-and-pepper" style map. However, no accurate characterization of the spatial correlations across a large population of neurons was carried out to validate the hypothesis. In our work, we measured OS tuning properties of L2/3 and L4 neurons in V1 with drifting gratings. A fine-scale spatial clustering of similar tuning preference localized within $\sim 20\ \mu m$ was found. Having demonstrated our ability to functionally image thalamic inputs to V1, we can

better understand the emergence of the clustering from the perspective of thalamocortical interaction with more experiments carried out in the future.

1.3 Data analysis of calcium imaging

We processed the large-scale calcium imaging data with custom-written MATLAB® codes. A typical calcium data analysis pipeline consists of the following steps: (1) motion correction on the raw time-lapse two-photon images; (2) detection of regions of interest (ROIs), such as neurons; (3) calcium transient computation for each ROI; (4) analysis of tuning or other properties.

To improve our data analysis pipeline, we devised a more reliable method to estimate neuropil contamination. Neuropil contamination is a common problem when imaging neurons that express calcium indicators throughout their cytosol. Ideally, the detected fluorescence signals only come from cell bodies of identified neurons. However, axons and dendrites passing through the target region can also express the calcium indicator [74]. Hence the fluorescence signals from cell bodies are contaminated by the surrounding neuropils. The neuropil signals are spatially diffuse and can obscure the tuning properties of neurons. Sometimes, overestimation or underestimation of neuropil signals may lead to opposite conclusions in the research [75, 76]. Therefore, neuropil subtraction must be performed to extract the accurate response of the neurons. Although many methods have been proposed to estimate the neuropil signals [77, 78], none of them is fully validated by experiments. We propose a more reliable and robust method for neuropil subtraction with nuclear-targeted calcium data as the groundtruth.

1.4 Thesis highlights

This thesis is organized as follows:

Chapter 2 introduces the technique of aberration-free single-objective remote focusing. The aberrations induced by remote focusing are characterized for systems with different NAs. This chapter presents its applications in imaging neurites and synapses in the mouse brain.

Chapter 3 discusses how AO-2PFM is adapted and optimized for mouse retinal imaging. It presents an important advancement in enabling high-resolution longitudinal studies of retinal pathology and pharmacology for disease diagnosis and treatment.

Chapter 4 presents the applications of two-photon microscopy in functional imaging of mouse thalamus and primary visual cortex. “Micro-clustering” organization of orientation tuning was discovered in L2/3 and L4 in mouse V1. The chapter also covers the data analysis pipeline for calcium imaging.

Chapter 2

Single-objective remote focusing for adaptive optical two-photon fluorescence microscopy[1]

2.1 Introduction

2PFM has been widely applied to 3D imaging, given that it provides thin optical sections of samples by constraining the focal spot in a limited volume. For typical 3D imaging, in addition to acquire a 2D image by raster scanning the focus laterally, the laser focus also needs to move axially to obtain a 3D image stack. The simplest way to move the focus relative to the sample is by translation of the microscope objective. However, the volumetric imaging speed is limited by the time delay between consecutive 2D scans due to inertia of the objective lens. In order to avoid the limitations posed by inertia from objective motion, people came up with an alternative method to axially move the laser focus by controlling the excitation beam divergence. Variable-focus lenses such as electrically tunable lenses [79] and ultrasound lenses [80] are commonly employed, where the shape or refractive index distribution of the lens is varied to control beam divergence of the transmitted light. Another type of devices are deformable mirrors (DM) and liquid-crystal spatial light modulators (SLM), which vary the beam divergence by spatially modulating the wavefront of the reflected light waves [36, 81]. Acousto-optical deflectors have also been used to control beam divergence and can allow random access 2PFM in 3D [82, 83].

However, those divergence-control-based remote focusing methods offer higher volumetric imaging speed at the cost of reduced spatial resolution. Infinity-corrected microscope objectives, which is typically used for 2PFM, have optimal diffraction-limited imaging performance for collimated beam only. Therefore, changing the beam divergence leads to an aberrated

[1] Adapted from "Yang, Y., Chen, W., Fan, J. L., & Ji, N. (2021). Adaptive optics enables aberration-free single-objective remote focusing for two-photon fluorescence microscopy. Biomedical Optics Express, 12(1), 354-366."

focus and degraded image quality away from the natural focal plane [36–39]. Botcherby et al. [40–42] proposed a two-objective remote focusing approach to avoid this issue by passing the excitation light through two objectives so that their divergence-induced aberrations cancel each other. However, incorporating another objective substantially decreases power efficiency. A more power-efficient way to maintain focal quality during remote focusing is by using a single objective while directly measuring and correcting the aberrations using adaptive optics (AO) [13]. Previously, AO has been applied to point-scanning 2PFM in the context of single-objective remote focusing using a modal-based aberration measurement method [43], where minimal and moderate improvements in image quality were observed for objectives of 0.45 NA and 0.65 NA, respectively. For high-resolution imaging applications where subcellular features such as synapses need to be resolved, higher-NA objectives are required. In this work, using a zonal wavefront measurement method, we systematically characterized the aberrations introduced to excitation light via divergence-based remote focusing through microscope objectives of NA 0.45, 0.8, and 1.05. We found that with the increase of excitation NA, defocusing wavefronts of increasingly large amplitudes were required to generate the same amount of axial focal shift, and introduced more severe degradation of image quality. We used AO to fully correct the aberrations induced by beam divergence and achieved diffraction-limited imaging performance for axial ranges of up to 800 μm. We further demonstrated aberration-free remote focusing for in vivo imaging of neurites and synapses in the mouse brain.

2.2 Remote focusing and AO-2PFM

The schematic of our two-photon fluorescence microscope was described previously [24] (Fig.2.1A). In order to achieve the desired excitation NA, a motorized variable beam expander (model 56c-30-2-8x; Special Optics) was used to control the beam size of the collimated 920-nm output from a femtosecond laser (Insight DeepSee; Newport). Two-dimensional raster scanning in the focal plane was carried out by a pair of galvanometer scanners (6210H; Cambridge Technology) optically conjugated by two telecentric f-θ lenses (focal length: 30 mm; Special Optics). The galvos were further conjugated to a reflective liquid-crystal SLM (512×512 Spatial Light Modulator, HSP512; Meadowlark Optics) with a telecentric f-θ lens pair (focal length: 30 mm and 150 mm; Special Optics). The SLM was conjugated to the rear pupil plane of the microscope objective with another telecentric f-θ lens pair (focal length: 120 mm and 240 mm; Special Optics), with the divergence of the excitation beam and the axial focal position controlled by the phase pattern applied on the SLM (Fig. 2.1B). By varying the phase pattern on the SLM, the excitation focus was shifted upwards or downwards along the optical axis of the objective without translating the objective or the sample stage. Three microscope objectives, a 25× 1.05-NA objective (Olympus), a 16× 0.8-NA objective (Nikon), and a 10× 0.45-NA objective (Nikon), were used, respectively, with the variable beam expander set to overfill their rear pupil.

Under sine condition, we derived the remote-focusing (RF) phase pattern ("RF pattern")

required to shift the focus by z relative to the natural focal plane of a collimated beam [84]

$$\phi(r) = n \cdot k \cdot z \cdot \sqrt{1 - \frac{(r \cdot M)^2}{(n \cdot f)^2}} = n \cdot k \cdot z(1 - \frac{(r \cdot M)^2}{2(n \cdot f)^2} + \frac{(r \cdot M)^4}{8(n \cdot f)^4}) \tag{2.1}$$

where n is the refractive index of the immersion medium, k is the wave vector of the laser beam, f is the focal length of the objective, z is the desired focus shift, M is the magnification from the SLM to the rear pupil, and r is the radial coordinate on the SLM. To check the effectiveness of the RF pattern, we performed a simulation using a vector diffraction model [85] to calculate the point spread function (PSF) with the RF pattern applied at the rear pupil. It successfully directed the focus to the designed axial position and maintained the intensity and resolution at the shifted focus. We also tested the performance of the second term in the expanded expression of the RF pattern, which was the Zernike defocus term commonly used for remote focusing in lower NA systems [43, 86]. In simulation, the Zernike defocus term led to substantial PSF degradation especially at high NA. For both the RF pattern and the Zernike defocus pattern, infinity-corrected microscope objectives introduce extra aberrations, which need to be measured and removed to recover diffraction-limited resolution.

We used the same SLM for the measurement and correction of the divergence-induced aberrations via an indirect wavefront sensing method based on pupil segmentation [24]. Aberrations of the microscope system without the introduction of RF pattern were corrected prior to all experiments using the same method. We first focused the collimated excitation beam on a 2-μ-diameter fluorescent bead. We then displayed a RF pattern (for the 1.05-NA objective) or a Zernike defocus pattern (for the 0.8- and 0.45-NA objectives) on the SLM which shifted the focus to within 1 μm of the designed axial position. Next, we moved the sample stage along the optical axis to refocus the bead. To measure the aberrations, we illuminated 1/25 of the pupil area at a time and recorded the bead image. Neighboring illuminated pupil segments had 50% overlap, resulting in 81 total bead images after all pupil segments were illuminated. Aberrations introduced a non-zero phase gradient for each wavefront segment, which led to a lateral focal shift and therefore a displacement of the bead image. From the ratio of the image displacement and the focal length of the objective, we obtained the phase gradient for each segment and determined the phase slope on the SLM required to move the focus of each wavefront segment back to the same position. A zonal wavefront reconstruction algorithm [87] was then used to calculate the corrective wavefront from the phase slopes. We then overlaid the corrective wavefront on the RF or the Zernike defocus pattern to achieve aberration-free remote focusing.

2.3 Mouse sample preparation and *in vivo* imaging

Thy1-GFP line M and wild-type mice were used for *in vivo* imaging, after recovering from virus injection (only for wild-type mouse) and cranial window implantation [88]. Mice were

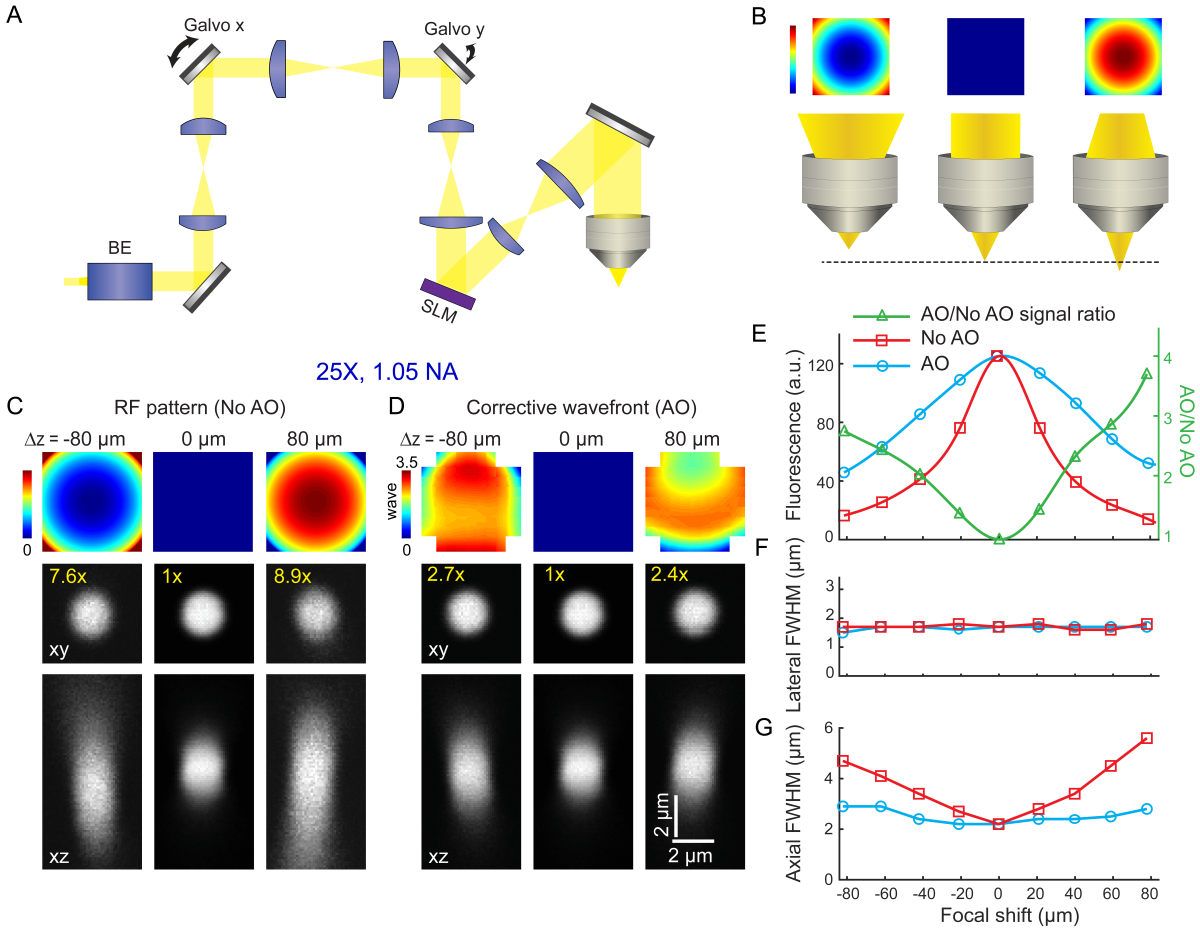

Figure 2.1: Aberration-free remote focusing two-photon fluorescence microscopy (2PFM) through a 25×, 1.05-NA microscope objective. (A) Schematic of the 2PFM. BE: beam expander; SLM: spatial light modulator. SLM is optically conjugated with the objective back pupil. It's used to control the beam divergence and correct the divergence-induced aberrations. (B) Beam divergence controls axial focal shift. Top: example two-dimensional (2D) phase patterns of converged, collimated, and diverged beams, respectively, at objective back pupil. (C) Top: remote-focusing (RF) patterns on the SLM to shift the focus by -80 μm, 0 μm, and 80 μm from the natural focal plane, respectively. Middle and Bottom: lateral (xy) and axial (xz) images of a 2-μm-diameter bead measured with the RF patterns only (without adaptive optics (AO) correction). Images at -80 μm and 80 μm have their brightness artificially increased by 7.6× and 9.5×, respectively, to improve visibility. (D) Top: Additional corrective AO patterns applied to SLM for the focal shifts in (C). Middle and Bottom: lateral (xy) and axial (xz) images of the 2-μm-diameter bead measured with AO. Images at -80 μm and 80 μm have their brightness artificially increased by 2.7× and 2.4×, respectively, to improve visibility. (E) Fluorescence signal of the bead measured with (blue) and without AO (red), and their ratio (green) and (F) Lateral and axial FWHMs of the bead images at different focal shifts.

given the analgesic buprenorphine subcutaneously (0.3 mg per kg of body weight) at the start of surgery and anesthetized with 1–2% isoflurane by volume in O_2 throughout the length of the surgery. A 3-mm craniotomy was performed over the primary visual cortex. Virus injection was performed using a glass pipette beveled at 45° with a 15-20-μm opening and back-filled with mineral oil. A hydraulic manipulator (MO10; Narishige) controlled a fitted plunger, which was inserted into the pipette and used to load and inject the viral solution into the cortex 350 μm below pia. 30 nL of 3×10^{13} GC/mL of AAV2/1-syn-GCaMP6s was injected at every injection site. 2-μm-diameter fluorescent microspheres (F-8826; Invitrogen) diluted in saline were then applied on the cortical surface for later measurement of aberrations. A cranial window made of a single glass coverslip (No. 1.5; Fisher Scientific) was embedded in the craniotomy and sealed in place with Vetbond (Vetbond; 3M). We then attached a titanium headpost to the skull with cyanoacrylate glue and dental acrylic. *In vivo* imaging was performed 2–4 weeks after virus injection, with the mice head-fixed and under deep anesthesia.

2.4 Aberration-free remote focusing through objectives with different NAs

We first carried out aberration-free remote focusing 2PFM through a 1.05-NA water-dipping objective (Fig. 2.1C-F). Applying a series of RF patterns to the SLM, we generated up to ± 80 μm axial focal shifts (Δz) and observed increasing degradation in image resolution and brightness. Under the same post-objective excitation power, at -80 μm and +80 μm focal shifts, the brightness of a 2-μm-diameter bead decreased by 7.6× and 9.5×, respectively, with a concurrent increase in its axial full width at half maximum (FWHM) (Fig. 2.1C), indicative of degradation in axial resolution. With the corrective wavefront applied, the brightness of the bead at -80 μm and +80 μm focal shifts increased by 2.8× and 4.0×, respectively, and its axial FWHM became substantially smaller (Fig. 2.1D). As expected, larger axial shifts by the RF pattern were accompanied by stronger aberrations and lower fluorescence brightness (Fig. 2.1E, red), and benefitted from greater signal recovery after aberration correction (Fig. 2.1E, green). Because axial resolution is more sensitive to the presence of aberrations, we observed minimal changes in the lateral FWHM (Fig. 2.1F) but increasingly severe degradation of axial FWHM of the 2-μm-diameter bead with increasing focal shift (Fig. 2.1G, red). AO correction substantially decreased axial FWHM to values close to that at the natural focal plane (Fig. 2.1G, blue).

We also tested the performance of remote focusing and AO on a 0.8-NA water-dipping objective and a 0.45-NA air objective (Fig. 2.2). Here, because the excitation NA was smaller, instead of applying the RF pattern to the SLM, we used Zernike defocus patterns for remote focusing over larger axial shift ranges (±200 μm for 0.8-NA and ±400 μm for 0.45-NA objectives, respectively). Similar to the 1.05-NA objective, larger axial shifts by Zernike defocus pattern led to more severe degradation in the signal and axial profiles of

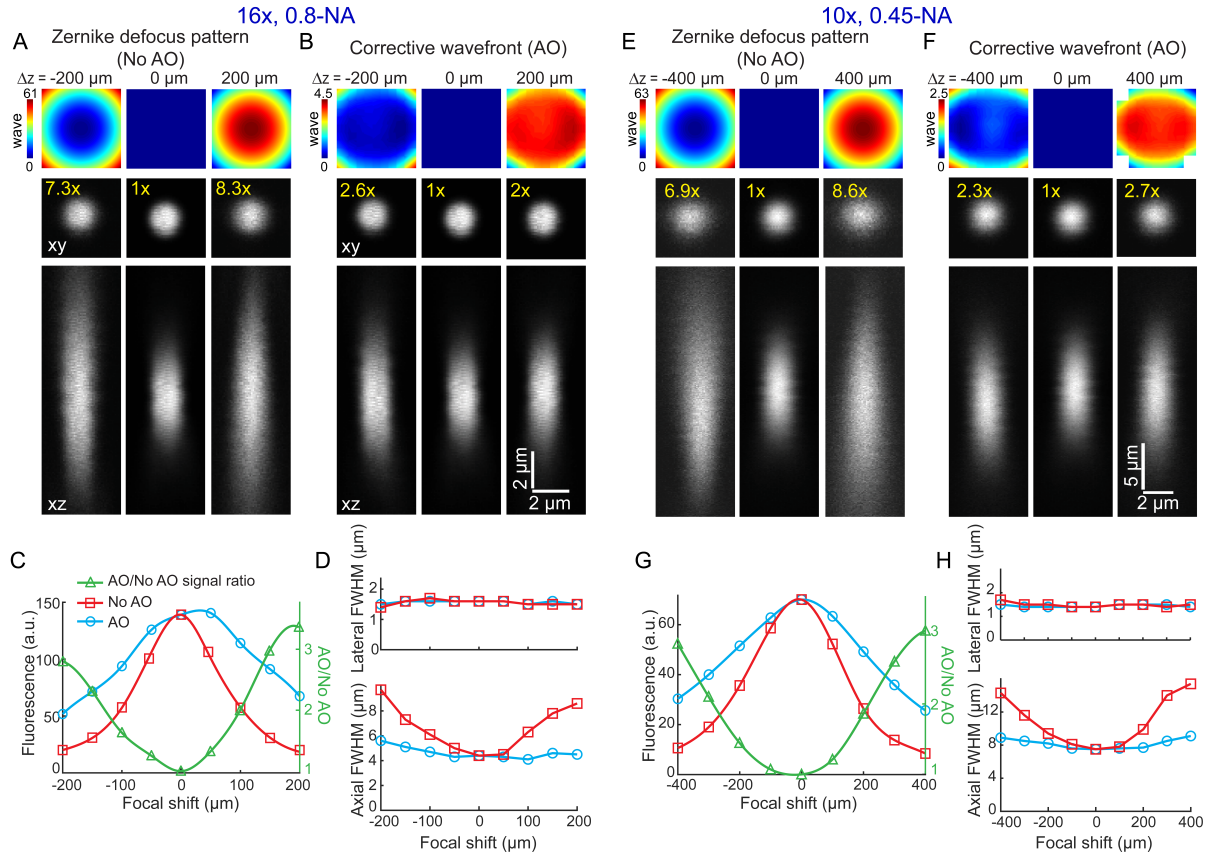

Figure 2.2: Aberration-free remote focusing 2PFM through (A-D) a 16×, 0.8NA objective and (E-H) a 10×, 0.45NA objective. (A,E) Zernike defocus patterns on the SLM to shift the focus away from the natural focal plane. Middle and Bottom: lateral (xy) and axial (xz) images of a 2-μm-diameter bead measured with the Zernike defocus patterns only (without AO correction). Images at non-zero focal shifts have their brightness artificially increased to improve visibility. (B,F): Top: Additional corrective AO patterns applied to SLM for the focal shifts in (A,E). Middle and Bottom: lateral (xy) and axial (xz) images of the 2-μm-diameter bead measured with AO. Images at non-zero focal shifts have their brightness artificially increased to improve visibility. (C,G) Fluorescence signal of the bead measured with (blue) and without AO (red), and their ratio (green). (D,H) Lateral and axial FWHMs of the bead images at different focal shifts measured with (blue) and without AO (red).

2-μm-diameter beads (Fig. 2.2C and 2.2G). At -200 μm and +200 μm focal shifts, the brightness of a 2-μm-diameter bead imaged by the 0.8-NA objective decreased by 7.3× and 8.3×, respectively (Fig. 2.2A). At -400 μm and +400 μm focal shifts, the brightness of a 2-μm-diameter bead imaged by the 0.45-NA objective decreased by 6.9× and 8.6×, respectively (Fig. 2.2E). Aberration correction with AO led to larger improvement in fluorescence signal at larger z displacement (Fig. 2.2B, 2.2C and 2.2F, 2.2G). Similar trends were observed in the axial FWHMs, where AO correction reduced the axial FWHM to close to that at the natural focal plane for both objectives (Fig. 2.2D and 2.2H).

2.5 Lack of full recovery of imaging performance due to limited efficiency of SLM

Comparing the remote focusing performance through all three objectives, we found that, with the increase of NA, defocusing wavefronts of increasingly large amplitudes were required for the same axial focal shift and led to more severe image degradation. Consistently across all three objectives, we found that AO correction of the divergence-induced aberrations did not fully recover the brightness and resolution at the natural focal plane, even though the measured post-objective power were the same. At the largest focal shifts, even with AO correction, remote focusing still led to decrease of bead fluorescence signal and slight degradation of their axial profiles. We carried out a series of experiments to investigate what the source for the signal and resolution degradation was.

First, we tested whether the imaging performance degradation arose from residual aberrations. With our indirect wavefront sensing method based on pupil segmentation [24], the corrective wavefront was composed of wavefront segments with constant phase slopes. A phase reconstruction algorithm [87] was used to compute the final corrective wavefront based on these slopes. We have found previously that for aberrations of very large magnitudes, uncorrected residual aberrations may lead to less-than-100% recovery of fluorescence signal [89]. To test whether the current method was able to fully correct the divergence-induced aberrations, we fit the aberrations measured at the largest focal shifts for all three objectives (opposite of the corrective wavefronts in Figs. 2.1D and 2.2B,F) with Zernike modes, and then displayed them on the SLM. These aberrations reduced signal strength but did not shift the images of 2-μm-diameter beads away from the natural focal plane (Figs. 2.3A,C,E). For all three objectives, our AO method was able to completely recover the signal and axial image of 2-μm-diameter beads (Figs. 2.3B,D,F). These measurements indicated that the signal and resolution decreases observed at large focal shifts were not caused by residual aberrations, and that our AO method was capable of fully reversing the effect of divergence-induced aberrations.

Comparing Figs. 2.3A,C,E with Fig. 2.1C and Figs. 2.2A,E, we noticed that displaying the divergence-induced aberrations alone on the SLM did not decrease the bead signal as much as when the RF or Zernike defocus patterns were applied. This observation provided

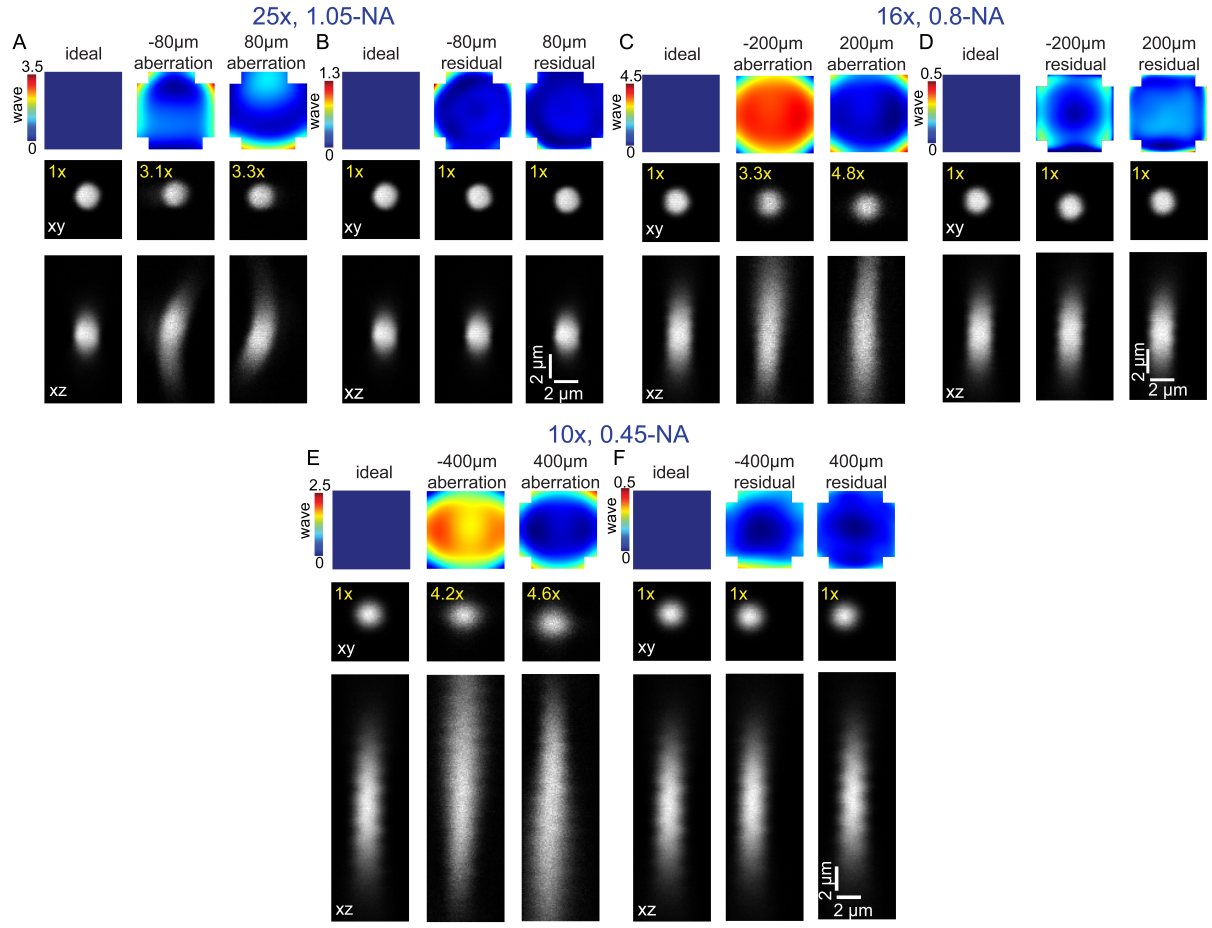

Figure 2.3: AO fully recovers diffraction-limited imaging performance from divergence-induced aberrations in a (A,B) 25×, 1.05-NA, (C,F) 16×, 0.8-NA, and (E,F) 10×, 0.45-NA objective. Top in (A,C,E): Wavefronts applied to the SLM that correspond to the divergence-induced aberrations in Figs. 2.1 and 2.2. Top in (B,D,F): Residual wavefronts on the SLM after AO correction. Middle and Bottom: lateral (xy) and axial (xz) images of a 2-μm-diameter bead measured with the corresponding phase patterns on the SLM. Some images have their brightness artificially increased to improve visibility.

further evidence that part of the signal drop observed in Fig. 2.1C and Figs. 2.2A,E did not arise from optical aberrations and thus could not be recovered by AO. Since the only difference in these two cases was that in the latter case, a defocus pattern was applied to the SLM, we thus investigated how the application of such a defocus pattern reduced excitation efficiency via a mechanism that was not related to optical aberration.

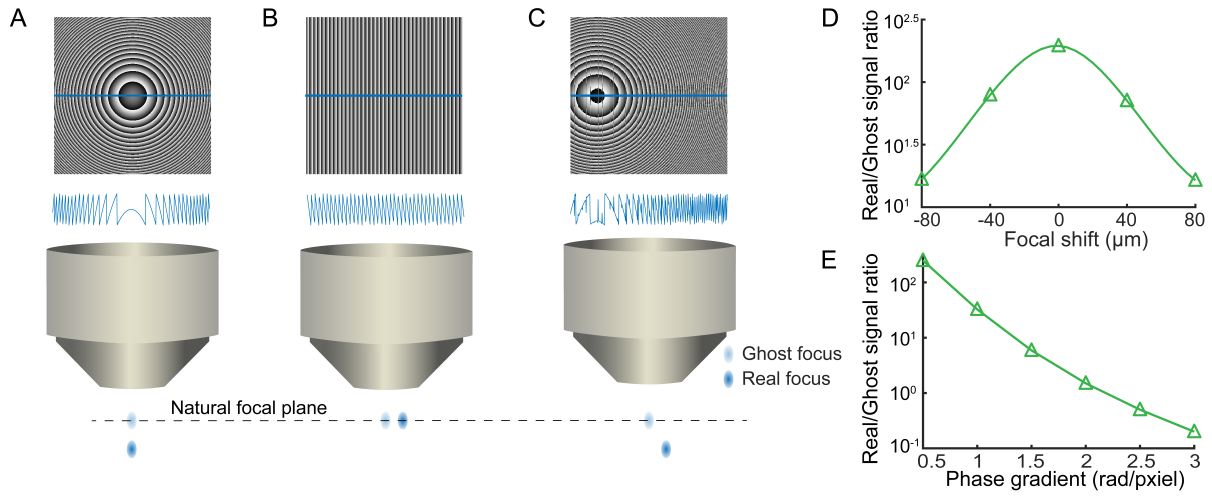

Figure 2.4: Modulated and unmodulated light by the SLM form a real and a ghost focus, respectively. (A-C) Schematics showing phase patterns on SLM and resulting real (dark blue) and ghost (light blue) foci, of (A) defocus pattern, (B) global phase ramp, and (C) the superposition of defocus and global phase ramp. Top: phase patterns on SLM; Middle:cross-sectional phase profiles along the horizontal blue lines. (D) Signal ratios of real (with AO) versus ghost images of a 2-μm-diameter fluorescent bead at different axial focal shifts. (E) Signal ratios of real (with AO) versus ghost images of a 2-μm-diameter fluorescent bead at different global phase gradients.

Unlike deformable mirrors where the physical deformation of mirror surface leads to ∼100% wavefront modulation for the reflected light, liquid-crystal SLMs do not have 100% efficiency. When we applied defocus patterns, in addition to the shifted "real" focus, a portion of the excitation light did not pick up the defocus modulation on its wavefront and this unmodulated beam formed a "ghost" focus at the natural focal plane (Fig. 2.4A). To prevent the ghost focus from interfering with the phase-modulated focus, in all wavefront modulation experiments involving a SLM (e.g., aberration measurement and correction during AO), we applied a global phase gradient to the entire SLM to shift the modulated focus away from the ghost focus (Fig. 2.4B). When using the SLM to shift the focus axially, we overlaid the defocus pattern with the global phase ramp. At nonzero defocus, the ghost focus was displaced from the modulated focus (the "real" focus) both laterally and axially (Fig. 2.4C). When applying all phase patterns, because liquid-crystal SLMs were designed to generate 2π phase shift, we wrapped any phase pattern with peak-to-valley value larger than 2π to $[0, 2\pi]$ before displaying them on the SLM (Figs. 2.4A-C).

Using phase patterns that were overlays of RF and global ramp patterns, we acquired images of 2-μm-diameter beads excited by the ghost and real foci (Fig. 2.4C), respectively, at different focal shifts with the 25× 1.05-NA objective. Comparing the fluorescence signals of the real image and ghost image of the bead (Fig. 2.4D), we found more excitation energy became unmodulated at larger axial focal shifts, indicating that at constant post-objective power, less energy was deposited to the modulated focus and led to a decrease of fluorescence signal. Same trend was observed for the 16× 0.8-NA and 10× 0.45-NA objectives. This explained why AO did not fully recover the signal strength at large focal shifts.

We speculated that the decrease of modulation efficiency at larger defocus was caused by phase wrapping. The rapid changes in gray levels for SLM pixels abutting the phase wrapping borders reflected large voltage differences between these neighboring pixels, which caused strong crosstalk, also known as fringing field effect, and resulted in phase deviations [90, 91]. Larger defocus patterns led to more frequent phase wrapping on the SLM and thus less efficient wavefront modulation. To verify this effect in our system, we applied a global phase ramp to the entire SLM, which after phase wrapping appeared as a blazed grating (Fig. 2.4B), and acquired images of 2-μm-diameter beads excited by the ghost and the real foci, respectively. With the increase of phase gradient, the ghost image formed by the undiffracted light appeared at the same position, while the real images showed up at increasing lateral displacements. The signal ratio between the real and the ghost images, as expected, decreased with increasing gradient (Fig. 2.4E), supporting our conclusion that the SLM became less efficient as larger focal shifts due to larger number of phase wraps.

In addition to causing signal drop, less efficient diffraction at large phase gradients by the SLM also explained the enlargement of axial profiles in the AO-corrected bead images at large focal shifts. Because phase gradient increases towards the edge of the pupil, marginal rays were less efficiently delivered to the focus than central rays. The reduction in marginal ray energy therefore led to a decrease of the effective excitation NA.

2.6 Remote focusing for 3D *in vivo* brain imaging

We applied this single-objective remote focusing approach for 3D imaging of the mouse brain *in vivo*. In the first example, we imaged the cortex of a mouse with neurons expressing the fluorescent protein GCaMP6s [92] using the 0.8-NA objective (Fig. 2.5). In order to measure the wavefront distortion caused by beam divergence alone, we placed a 2-μm-diameter fluorescent bead on top of dura under the cranial window during surgical preparation. With the bead at the natural focal plane using collimated excitation light, we measured and corrected the aberrations introduced by the cranial window. We then followed the same procedure as in 2.2 to obtain corrective wavefronts for up to ±200 μm axial focal shifts using the same bead. Setting the natural focal plane (Δz=0) at 230 μm below dura, we acquired images of neurons from 30 μm (Δz=-200 μm) to 430 μm (Δz=200 μm) below dura with varying Zernike defocus patterns every 50 μm in depth (Fig. 2.5). At each axial position, images were acquired both without and with correction for divergence-induced aberrations (Fig.

2.5A). Substantial increases of fluorescent signal and contrast were observed for both fine neurites (insets, Fig. 2.5A; upper panels, Fig. 2.5B) and neuronal cell bodies (lower panels, Fig. 2.5B) at focal displacement of 100 μm and above. Larger improvements were observed for neurites than for cell bodies, consistent with previous observations that images of smaller structures are more degraded by aberrations [93].

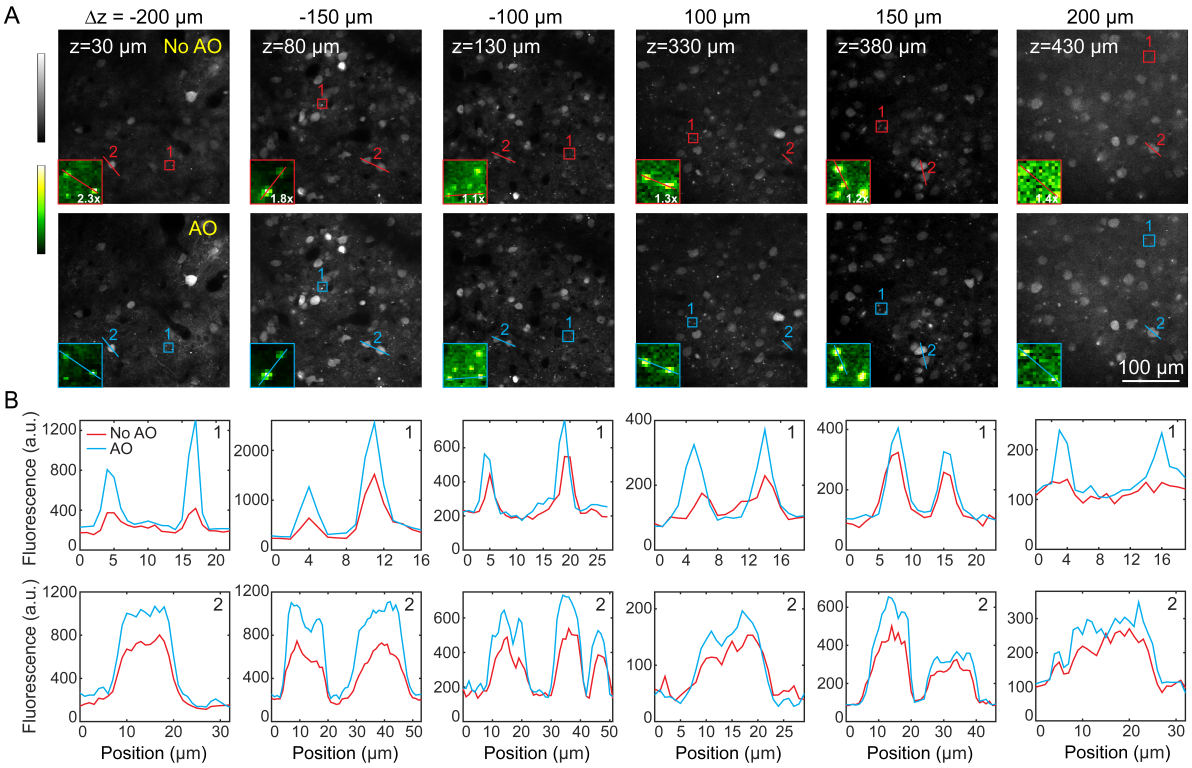

Figure 2.5: *In vivo* three-dimensional (3D) imaging of GCaMP6s-expressing neurons in the mouse brain with single-objective remote focusing through a 16×, 0.8-NA objective. (A) Images measured without (top) and with (bottom) AO correction for divergence-induced aberrations at different depths. Δz: focal shifts relative to the natural focal plane; z: depths below dura. Insets: zoomed-in views of neurites in boxes; "No AO" zoomed-in views have brightness artificially increased to improve visibility. All pairs of images normalized to the AO images. (B) Line signal profile comparisons of images measured without and with AO. Top: line profiles across neurites; Bottom: line profiles across cell bodies.

We also tested the performance of aberration-free single-objective remote focusing on imaging synaptic terminals such as dendritic spines and axonal boutons *in vivo* with a high-NA objective. Using the 1.05-NA objective, we imaged GFP-expressing cortical neurons through the cranial window in a Thy1-GFP line M mouse. Setting the natural focal plane (Δz=0) at 75 μm below dura, we acquired images of neurons from 5 μm (Δz=-70 μm) to 145 μm (Δz=70 μm) below dura with varying RF patterns every 1 μm in depth. Instead of measuring corrective patterns every 1-μm focal shift, which would be time-consuming, we obtained corrective patterns every 20 μm using a 2-μm-diameter fluorescent bead on dura

and interpolated from them corrective patterns every 1 μm. We came up with two algorithms for interpolation (see Ref. [94] for more details of the code). In a modal approach [95–97], we fit the measured corrective wavefronts with and obtained the coefficients for the first 45 Zernike modes. We then fit the two coefficients for each mode measured 20 μm apart with a linear function and interpolated the corresponding coefficient value for the desired focal shift. The corrective wavefront was then calculated from these coefficients. In a zonal approach based on the aberration measurement method described in 2.2, where 81 phase gradients were measured for each corrective wavefront, we linearly fit the corresponding phase gradient values for the two corrective wavefronts measured 20 μm apart and interpolated the phase gradient values for the desired focal shift. The 81 interpolated phase gradient values were then used to calculate the final corrective wavefront. For images presented in Fig. 2.6A, the zonal approach was used for interpolation.

Due to the sparse fluorescence labeling in the Thy1-GFP line M mouse cortex, we plotted the maximal intensity projections of image stacks to facilitate the visualization of synaptic terminals (Fig. 2.6). At focal shifts of a few tens of microns, the aberrations introduced by the 1.05-NA objective were already large enough to cause easily perceived differences in signal and resolution for images of synapses (zoomed-in views, Fig. 2.6A). Applying corrective patterns substantially improved image quality and increased the brightness of synapses by up to 2.3×. As expected, larger improvements were observed at larger focal shifts. At largest focal shifts, the improvement in resolution can be appreciated even in the lateral xy images (e.g., leftmost and rightmost zoomed-in views, Fig. 2.6A).

2.7 Discussion

Shifting focal plane by controlling the divergence of image-forming light has become a popular method for volumetric imaging in microscopy. Even though it is widely appreciated that such a divergence-based approach can reduce image quality, a systematic characterization over large focal shift ranges, especially at high NA, had not been carried out. Here, we characterized how divergence-based single-objective remote focusing degraded image quality of 2PFM for microscope objectives of NA 0.45, 0.8, and 1.05. For all microscope objectives, image quality, as measured from 2-μm-diameter fluorescent beads, degraded with axial shift away from the natural focal plane. This effect became more severe with the increase of NA. For the 0.45-NA objective, it took 400 μm of focal shift for the signal to drop below 15% of the value at natural focus. In contrast, it took 200 μm of focal shift through the 0.8-NA and 80 μm of focal shift through the 1.05-NA objectives for similar amount of signal drop. Our results suggest that when designing a divergence-based single-objective remote focusing system, a compromise between the achievable axial shift range and the desired NA for the image-forming light exists and needs to be considered explicitly to reach the optimal combination of imaging volume and resolution.

AO has been widely used to correct optical aberrations originating from both microscopy systems and samples. Here, we demonstrated that AO can fully correct the aberrations

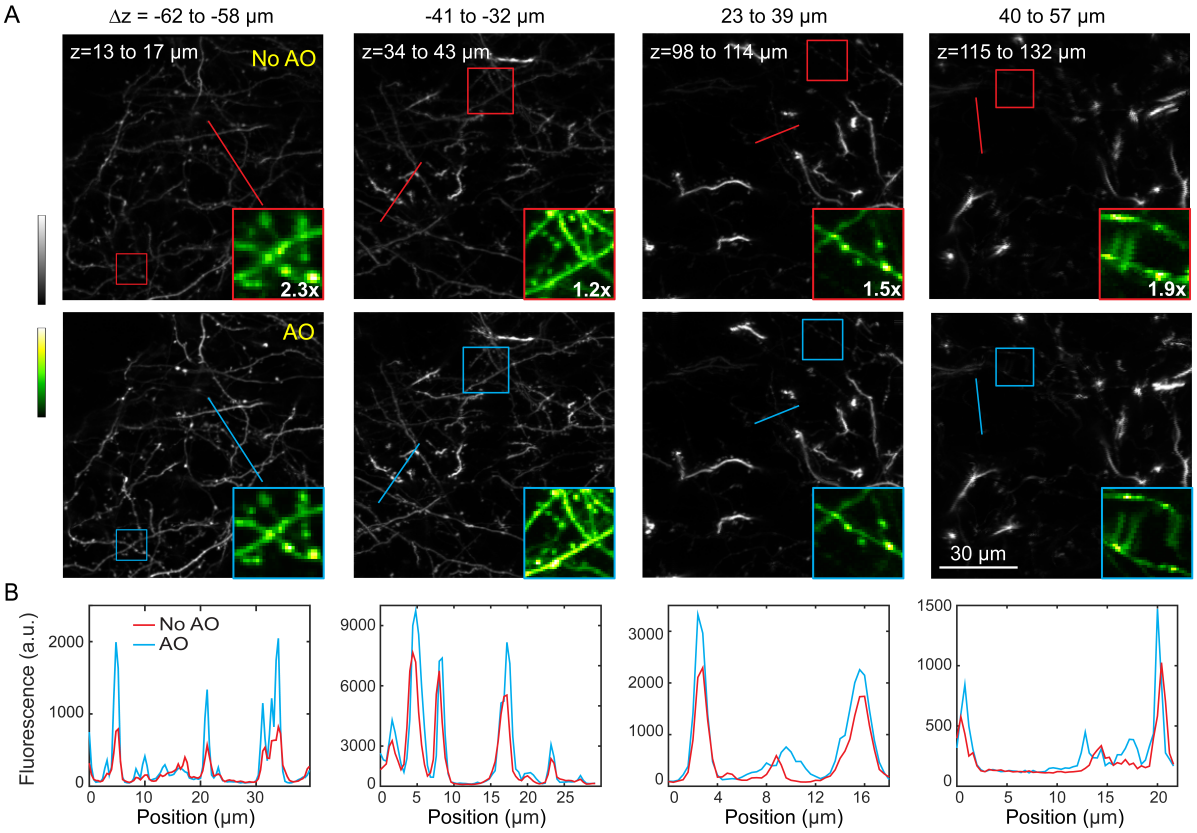

Figure 2.6: ***in vivo*** **3D imaging of neurites and synapses in the brain of a Thy1-GFP line M mouse with single-objective remote focusing through a 25×, 1.05-NA objective.** (A) Images measured without (top) and with (bottom) AO correction for divergence-induced aberrations at different depths. Δz: focal shifts relative to the natural focal plane; z: depths below dura. Insets: zoomed-in views of neurites and synapses in boxes; "No AO" zoomed-in views have brightness artificially increased to improve visibility. All pairs of images normalized to the AO images. (B) Line signal profile comparisons of images measured without and with AO.

introduced by divergence. Consistently across all three objectives, correcting aberrations associated with divergence increased the signal and improved resolution of the 2PFM images, but it did not fully recover the fluorescence signal or resolution observed at the natural focal plane. Instead of uncorrected residual aberrations, this lack of 100% recovery was because pixel crosstalk decreased SLM efficiency with increasing defocus, leading to smaller fraction of energy being delivered to focus further away from the natural focal plane. This poses an ultimate limit on SLM-based remote focusing even for microscope systems equipped with AO. For the same focal shifts, higher-NA system required defocus patterns with larger phase gradients and suffered more severe reduction in SLM efficiency and the resulting drop in signal and resolution. To improve the performance of liquid-crystal-SLM-based axial scanning system, methods compensating for pixel crosstalk can be applied to improve SLM

efficiency [90, 91]. Everything else being equal, a SLM with higher pixel counts should give superior performance. Alternatively, a deformable mirror can be used to generate remote focusing as well as correct its associated aberrations.

Given that arbitrary values may be chosen for focal shifts during image collection, we came up with two interpolation approaches based on Zernike decomposition and phase gradient analysis, respectively. We thereby only needed to measure the corrective wavefronts at several focal shift positions, from which we could calculate the corrective wavefronts for all other focal shift positions on demand. Given that the divergence-induced aberrations should remain unchanged for each microscope objective, the same set of corrective patterns only need to be acquired once and can be used repeatedly for all subsequent experiments.

We tested the performance of this aberration-free single-objective remote focusing approach for *in vivo* imaging of the mouse brain. For both 0.8-NA and 1.05-NA objectives, correction of the divergence-induced aberrations improved the signal and contrast of the images of neuronal structures. It should be pointed out here that although the remote focusing process was aberration-free, the *in vivo* images themselves were not, because the aberrations from the brain tissue itself were not removed. Adding the corrective wavefronts for the sample-induced aberrations and the divergence-induced aberrations at each imaging depth, one would obtain images of the best quality throughout the tissue volume.

In this work, we used a liquid crystal SLM for divergence control and aberration correction, instead of a DM. Our SLM had 512×512 pixels and was phase-wrapped to generate wavefronts of more than 110 waves peak-to-valley. It allowed a larger axial scanning range than DMs of similar cost, whose axial range is mainly limited by its stroke [86]. Our SLM has a refresh rate of 100 Hz, lower than that of typical DMs. However, liquid crystal SLMs of kilohertz frame rate are becoming available, which once synchronized with frame acquisition, would allow aberration-free fast volumetric imaging at high spatial resolution.

Chapter 3

In vivo retinal imaging by adaptive optical two-photon fluorescence microscopy[1]

3.1 Introduction

Being part of central nervous system, retina is the only neural tissue whose physiology and pathology can be non-invasively probed by optical microscopy. Among all microscopies, 2PFM provides unique benefits for retinal imaging with its intrinsic optical sectioning capability. However, high-resolution visualization of subcellular features can hardly be achieved by two-photon *in vivo* imaging due to severe aberrations induced by the optics of the mouse eye. As a result, the vast majority of studies have been carried out *ex vivo* on dissected retinas, preventing longitudinal investigations of retinal pathology under physiological conditions. AO is a collection of technologies that actively measure and correct for optical aberrations [15], and has been applied to optical microscopy for high-resolution imaging of neural tissues [13, 98]. It has also been combined with ophthalmological imaging modalities to restore diffraction-limited imaging performance for human retina [99, 100]. Because of the severe aberrations of the mouse eye, AO has also been applied to *in vivo* imaging of the mouse retina [20, 101–107]. However, there are contradictions in the reported spatial resolutions [20, 101–107], characteristics and magnitude of aberration [20, 101–103, 106, 107], and the effectiveness of AO [20, 102, 103, 106, 107]. These discrepancies have led to confusions over the imaging performance achievable with conventional 2PFM and the necessity of AO for microvascular and cellular investigations of retinal physiology.

The aims of this work are to optimize the design of a 2PFM for in vivo imaging of the mouse retina, characterize mouse ocular aberration, develop a guideline for adaptive

[1] Adapted from "Zhang, Q., Yang, Y., Cao, K., Chen, W., Paidi, S., Xia, C., Kramer, R., Gong, X., & Ji, N. (2022). Retinal microvascular and neuronal pathologies probed in vivo by adaptive optical two-photon fluorescence microscopy [Manuscript submitted for publication]."

optical 2PFM (AO-2PFM) imaging, and demonstrate its applications to retinal pathology and pharmacology. Using a carefully engineered 2PFM and following an optimized sample preparation procedure, we demonstrated that although AO substantially improved image brightness, contrast, and resolution, capillary and 2D cellular resolution imaging performance was achievable through the mouse eye without AO. For subcellular and synaptic, as well as 3D cellular resolution imaging of the mouse retina, AO was essential, and we proposed strategies to maximize its impact on image quality improvement. We extended the application of AO-2PFM to mouse retinal pathology and pharmacology by imaging the retinas of two transgenic models with over-grown blood vessels and retinal degeneration, respectively. In the over-grown vessel model, AO enabled us to, for the first time, characterize retinal vascular lesions with sub-capillary details over multiple days and track microglial migration in vivo. In the retina-degeneration model, AO allowed high-fidelity interrogation of pharmacologically modified hyperactivity of retinal ganglion cells (RGC), indicating AO-2PFM as a promising tool evaluating retinal pharmacology *in vivo*. Together, by systematically optimizing and applying AO-2PFM to in vivo mouse retinal imaging, our work represents an important advancement in enabling high-resolution longitudinal studies of retinal pathology and pharmacology for disease diagnosis and treatment.

3.2 AO-2PFM for *in vivo* mouse retinal imaging

A home-built 2-photon fluorescence microscope equipped with a segmented deformable mirror (DM) and a Shack-Hartmann (SH) sensor [35] was modified for *in vivo* mouse retinal imaging by replacing the objective lens with an add-on eye imaging module [20, 108] (Fig. 3.1A, Materials and Methods). The module consisted of an electrically tunable lens (ETL) whose adaptive surface was conjugated to the DM, a turning mirror, and two lens groups (L7 and L8) that relayed the adaptive surface of the ETL to the pupil of the mouse eye. With this design, the optics of the mouse eye focused 920 nm light onto the retina to excite fluorescent markers and collected the emitted fluorescence for detection. The ETL allowed us to adjust the focal plane in the mouse eye without translating the mouse [109] or optics [110] in the imaging system. For all experiments, system aberrations in the 2-photon illumination path were measured with a modal AO method and corrected before image acquisition (Materials and Methods; "No AO" images: system aberration correction only).

To ensure optimal performance, we thoroughly characterized our AO-2PFM. We investigated how ETL current and mouse eye placement (with a longitudinal displacement of up to 4 mm in typical experiments) impacted imaging performance (Fig. 3.2). We found that aberrations introduced by the ETL at different currents minimally affected image quality and that axial focal shift varied linearly with ETL current while field-of-view (FOV) size remained mostly constant. We also optimized sample preparation procedure. We discovered that a custom-designed 0-diopter contact lens (CL; design parameters in Fig. 3.3A) in combination with a single application of eye gel between the CL and the cornea reduced

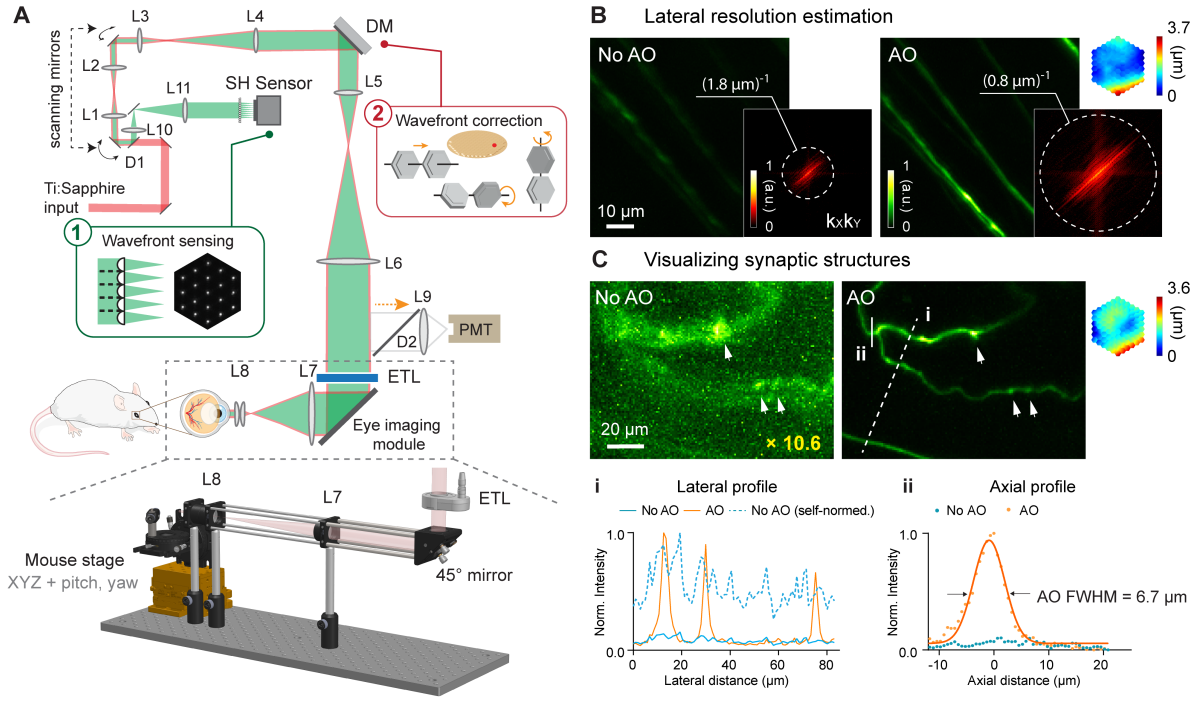

Figure 3.1: Adaptive optical two-photon fluorescence microscopy (AO-2PFM) for diffraction-limited imaging of the mouse retina *in vivo*. (A) Schematics of AO-2PFM. Inset 1: direct wavefront measurement by a Shack-Hartmann (SH) sensor composed of a lenslet array and a camera. Inset 2: wavefront correction with a deformable mirror composed of 163 segments with piston, tip, and tilt controls. Grey dashed box: eye imaging module. Bottom: 3D assembly of eye imaging module. L, lens; D, dichroic mirror; DM, deformable mirror; PMT, photomultiplier tube; ETL, electrically tunable lens. (B) Maximum intensity projections (MIPs) of image stacks ($72 \times 72 \times 25\ \mu m^3$) of retinal ganglion cell (RGC) axons measured without and with AO, respectively, normalized to AO image. Insets: $k_x k_y$ spatial frequency representation of the images and corrective wavefront. (C) MIPs of image stacks ($132 \times 97 \times 32\ \mu m^3$) of fine RGC processes measured without and with AO, respectively, normalized to AO image. 'No AO' image brightness artificially increased by 10.6× for better visualization. White arrowheads: synaptic structures. Inset: corrective wavefront. Bottom: i: lateral signal profiles along white dashed line; ii: axial signal profiles of process ii (white arrow).

aberrations, improved wavefront sensing, and prevented cataract formation for hours (Fig. 3.3).

In order to achieve diffraction-limited imaging of the mouse retina *in vivo*, we measured and corrected ocular aberrations with a direct wavefront sensing method [17, 18], utilizing the SH sensor for wavefront measurement and the DM for wavefront correction (Fig. 3.1A). Briefly, a 3D-localized fluorescence 'guide star' was formed in the retina via 2-photon excitation and scanned over a user-defined 2D area with galvanometer scanning mirrors. The emitted fluorescence was collected and, after being descanned by the same pair of scanning mirrors, directed to the SH sensor. The now stationary fluorescence wavefront was segmented by a lenslet array and focused onto a camera, forming an SH image composed of an array of foci (Fig. 3.1A, inset 1). Local phase slopes of wavefront segments were calculated from the displacements of the foci from those taken without aberrations. Assuming spatially continuous aberrations, we computationally reconstructed the wavefront from the phase slopes [87]. We then applied a corrective wavefront, opposite to the measured aberrations, to the DM by controlling the tip, tilt, and piston of each segment (Fig. 3.1A, inset 2) so that mouse ocular aberrations could be canceled out, ensuring diffraction-limited focusing of the 2-photon excitation light on the mouse retina.

All *in vivo* imaging experiments were conducted in anesthetized mice with dilated pupil (Materials and Methods). In most experiments, an area of 19 $\times$ 19 μm^2 of the retina was scanned for 3-10 seconds for wavefront sensing. To estimate the spatial resolution of our AO-2PFM for *in vivo* mouse retinal imaging, we imaged Thy1-GFP line M transgenic mice that had green fluorescent protein (GFP) expressed in a subset of RGCs [111]. The image taken without AO showed dim and distorted RGC axons; after aberration correction, we achieved an 8.6$\times$ increase in signal and proper visualization of the fine RGC axons (Fig. 3.1B). The spatial frequency space representations of the images indicated that AO enhanced the ability of the imaging system to acquire higher resolution information and led to a lateral resolution that was better than $\sim$0.8 μm (Fig. 3.1B, insets). For some thin RGC processes (Fig. 3.1C), restoring diffraction-limited resolution led to an increase in signal (by 10.6$\times$) and contrast (Fig. 3.1C, i), and, for the first time, enabled *in vivo* 2PFM visualization of synaptic structures in the mouse retina (Fig. 3.1C, white arrows). From the axial profile of a thin process (Fig. 3.1C, ii), we estimated the axial resolution after AO correction to be 6.7 μm. Both the lateral and axial resolution estimations were close to the theoretical diffraction-limited resolution for a fully-dilated 0.49 numerical aperture mouse eye [112].

3.3 *In vivo* imaging of retinal vasculature

Retinal vasculature supports the normal physiological functions of the retina. Abnormalities in retinal vasculature morphology and physiology serve as important biomarkers for various diseases [113–116]. Therefore, *in vivo* characterization of retinal vasculature, especially at the microvasculature level, is of great physiological and clinical importance. Utilizing either confocal microscopy [102, 107] or 2PFM [20, 117, 118], previous publications have achieved

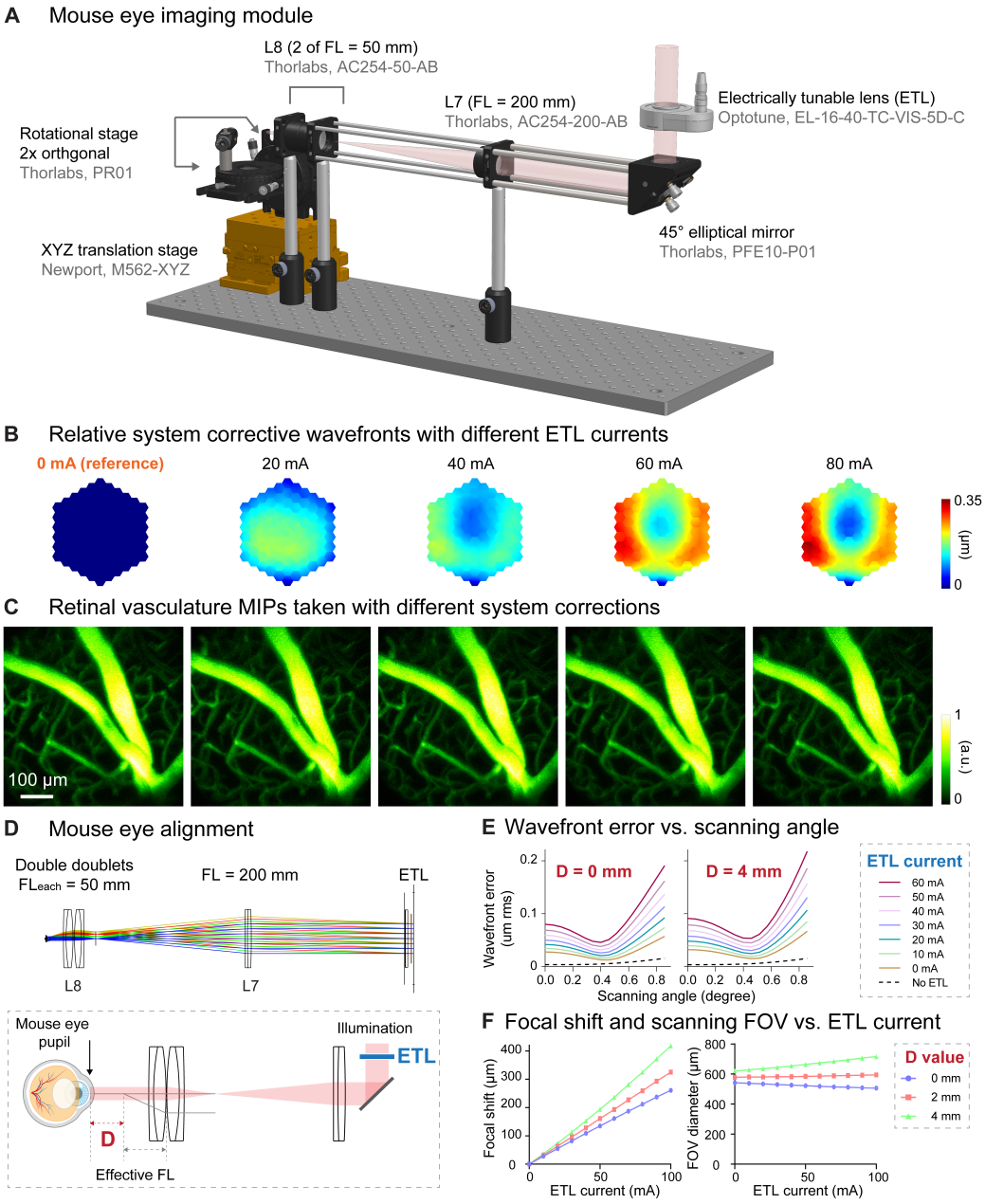

Figure 3.2: Characterization of aberrations introduced by ETL and alignment. (A) 3D rendering of the eye imaging module. (B) Additional corrective wavefronts for system aberrations measured with 0, 20, 40, 60, and 80 mA ETL currents, relative to the corrective wavefront measured with 0 ETL current. (C) MIPs of dye-injected retinal vasculature image stacks ($550 \times 550 \times 127 \mu m^3$) measured with corresponding system corrections in (B). (D) Top: Zemax ray tracing of the eye imaging module. Bottom: illustration of mouse eye alignment (not to scale). D: distance between the mouse eye pupil and L8 focal plane. (E) Wavefront errors versus scanning angle (at the ETL) for different ETL currents with the mouse eye placed at D = 0 mm and D = 4 mm, respectively, obtained by ray tracing. (F) Relative focal shift and imaging field-of-view (FOV) versus ETL current at different D values, obtained by ray tracing.

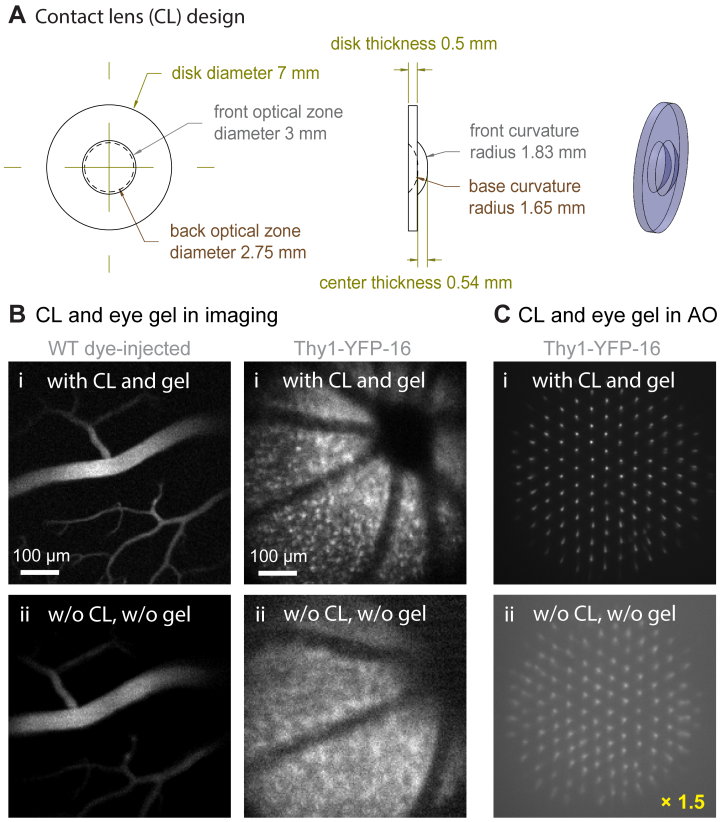

Figure 3.3: Contact lens and eye gel application improve image and wavefront sensing quality. (A) Design of the customized contact lens (CL). (B) 2PFM single-plane images of (left) retinal vasculature and (right) retinal cells acquired (i) with CL and eye gel and (ii) without CL or eye gel. All images taken with system aberration correction and normalized to (i). WT: wildtype. (C) Shack-Hartmann (SH) sensor images acquired from the Thy1-YFP-16 mouse retina in (B), normalized to SH image in (i). Brightness of SH image in (ii) artificially increased by 1.5× for better visualization.

in vivo visualization of retinal microvasculature through either full correction of the mouse eye aberrations [20, 102, 107], partial correction of the anterior optics of the mouse eye [118], or stringent selection of imaging lenses [117]. These prior demonstration-of-principle experiments suggest that in order to image retinal microvasculature *in vivo*, mouse eye aberrations need to be corrected, either fully or partially. With our optimized imaging system, we aimed to determine whether aberration correction was indeed essential for visualizing microvasculature. Furthermore, we proceeded to systematically characterize the spatial dependence of mouse eye aberrations and how large a FOV can benefit from a single AO correction.

To verify the necessity of AO in resolving mouse retinal microvasculature and characterize mouse eye induced aberrations, we performed *in vivo* 2PFM angiography by retro-orbitally injecting dextran-conjugated fluorescein isothiocyanate (FITC) into the non-imaged eye. Aberrations were measured with fluorescence emitted from vessels in the superficial plexus

(red asterisk, Fig. 3.4A; wavefront sensing area: 19 × 19 μm^2). After AO correction, we observed a 2-10× enhancement in signal (Fig. 3.4B,C). Comparing the line signal profiles (along the orange dashed lines, Fig. 3.4A,B), we found that AO improved signal for all vessels while its impact on signal of smaller capillaries (Fig. 3.4C, black asterisks; 6-10× improvement) was more substantial than on larger vessels (Fig. 3.4C, black circles; 2-3× improvement). Despite the substantial signal improvements enabled by AO, we found that most capillaries, due to their size and sparse distribution in space, could be resolved in 3D without AO by our optimized 2PFM, albeit at reduced contrast and resolution (Fig. 3.4D,E). Our results indicate that a properly designed 2PFM is capable of acquiring retinal angiograms at the level of individual capillaries.

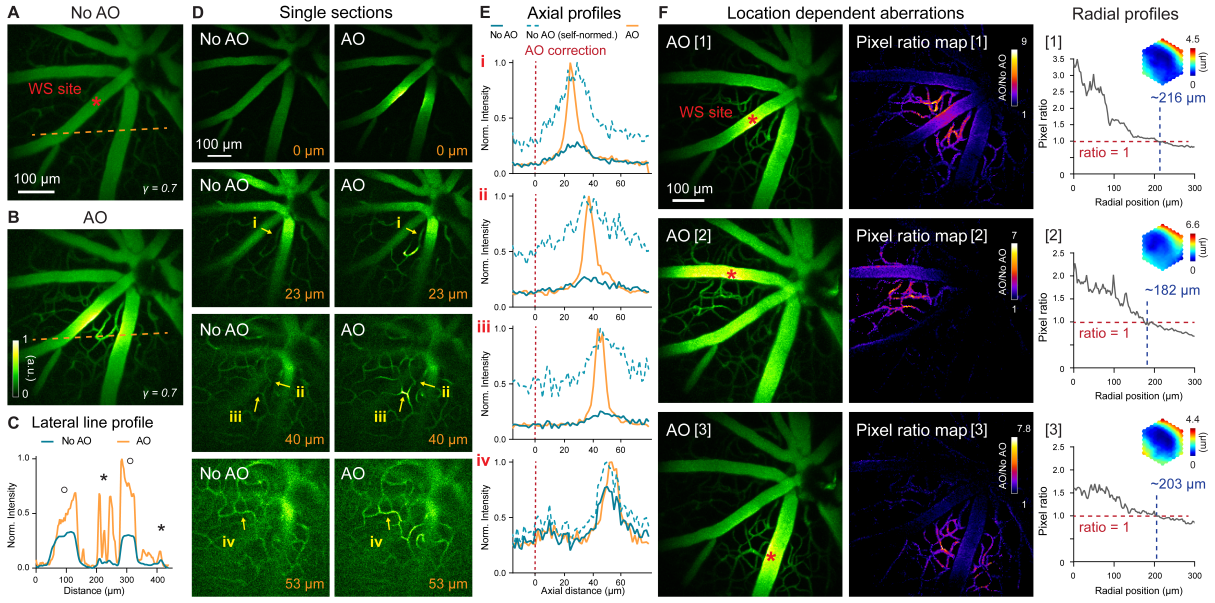

Figure 3.4: ***In vivo*** **imaging of mouse retinal vasculature with AO-2PFM.** (A,B) MIPs of image stacks (580 × 580 × 128 μm^3) of vasculature measured (A) without and (B) with AO, respectively, normalized to AO image. Red asterisk: center of a 19 × 19 μm^2 wavefront sensing (WS) area. (C) Lateral line profiles along orange dashed lines in A and B. Black circles: large vessels; black asterisks: capillaries. (D) Single image planes at 0, 23, 40, and 53 μm below the superficial vascular plexus acquired without and with AO correction performed at the superficial plexus (0 μm), normalized to AO image. (E) Axial profiles of capillary structures (i-iv in D). Red dashed lines: depth of wavefront sensing area. (F) Left: MIPs of image stacks (580 × 580 × 110 μm^3) acquired with WS performed at different locations in the FOV (red asterisks). Middle: AO/No AO pixel ratio maps. Right: radially averaged profiles of pixel ratio maps, centered at WS sites. Insets: corrective wavefronts. MIPs and pixel ratio maps individually normalized.

We further evaluated how the mouse ocular aberrations varied with imaging depth and field position. We found that AO performed at the superficial plexus was beneficial for imaging deeper layers, with the correction at superficial depth improving signal, resolution, and contrast of deeper vasculature (Figs. 3.4D,E). This result indicated that most aberra-

tions of the mouse eye arose from cornea and crystalline lens, instead of retina. Because the crystalline lens of the mouse eye has a gradient refractive index distribution [119, 120], ocular aberrations should also be field dependent [121, 122]. Field-dependent aberrations might also be introduced when the mouse eye was positioned off-axis with respect to the eye imaging module. We therefore examined how aberrations varied with FOV position and characterized the area within which a single correction led to substantial signal improvement. We performed AO at different locations of the superficial plexus in the FOV (Fig. 3.4F, left column, red asterisks) and compared their performance. The "AO/No AO" pixel ratio maps (Fig. 3.4F, middle column) exhibited field-dependent signal increase with larger gain achieved at pixels closer to the locations of aberration measurements. We quantified the effective area of AO in terms of signal improvement by calculating the radially averaged profiles of these pixel ratio maps (Fig. 3.4F, right column; origins at the wavefront sensing locations). We found signal improvement ("AO/No AO" pixel ratio ≥ 1) within a radius of ~ 216 μm when AO was performed at the FOV center of this mouse (Fig. 3.4F, [1]). For off-center locations, this radius was slightly smaller (Fig. 3.4F, [2] and [3]).

3.4 Cellular imaging of neurons in the mouse retina

The mouse retina consists of multiple layers of neurons with different cell types and distinct physiological properties. In the early stage of retinal diseases, abnormal morphology and function are usually confined to specific cell types within a single layer [123]. Therefore, for microscopic investigations of retinal physiology and pathology, it is essential to resolve cells in 3D. We evaluated whether our optimized 2PFM was capable of 3D cellular resolution imaging without correcting the severe aberrations of the mouse eye.

For this purpose, we imaged the densely fluorescent Thy1-YFP-16 mouse retina *in vivo*, where all bipolar cells, amacrine cells, and retinal ganglion cells were labeled with yellow fluorescence protein [111] (YFP). A single AO correction acquired by scanning a 19×19 μm^2 area (centered on the red asterisk in Fig. 3.5A) substantially improved signal and resolution (Fig. 3.5A,B), recovering higher spatial frequency information in both lateral and axial images (Fig. 3.5C,D). The resolution enhancement was especially striking along the axial direction, allowing retinal layers to be more clearly differentiated by better resolving neurons at different depths (Fig. 3.5A,B, XZ images). This improvement in axial resolution is especially important for functional imaging, because it minimizes neuropil contamination and ensures accurate characterization of the functional properties of neurons [88, 93, 124]. Therefore, AO was necessary for 3D cellular resolution imaging of retinal neurons *in vivo*. In the lateral image planes, our optimized 2PFM design and mouse preparation allowed the identification of individual neurons without AO, albeit at lower signal and poorer resolution than those achieved with AO, for inner nuclear layer, inner plexiform layer, and ganglion cell layer (Fig. 3.5E). In contrast, subcellular processes could not be visualized without aberration correction (e.g., processes in the inner plexiform layer, Fig. 3.5E, middle column).

Similar to our vascular imaging results, the Thy1-YFP-16 mouse eye exhibited field-dependent aberrations. For areas away from the AO measurement location (e.g., blue dashed box in Fig. 3.5A), although resolution improvement remained, the correction acquired at the FOV center (Fig. 3.5F, Central AO) did not increase signal strength as much as the locally acquired correction (centered on the blue asterisk in Fig. 3.5A; Fig. 3.5F, Local AO). For the Thy1-YFP-16 mouse, the effective area of AO performed at the FOV center was estimated from the "AO/No AO" ratio map (Fig. 3.5G) to have a radius of 185 μm (Fig. 3.5H).

3.5 Effective area of AO correction for 3D cellular resolution imaging

Imaging retinal vascular and neuronal structures, we found that the spatially-varying aberrations of the mouse eye limited the effective area for AO correction that was acquired by sensing wavefront from a small region of the retina (e.g., 19 $\times$ 19 μm^2 for Figs. 3.13.43.5). Although this approach succeeded in resolving synaptic features (Fig. 3.1C) and neuronal processes (Fig. 3.5E,F), for applications requiring 3D neuronal population imaging, synaptic resolution can be sacrificed in favor of cellular resolution imaging capability over larger FOVs. The latter can be achieved by correcting only for global mouse eye aberrations measured by scanning a larger retinal region for wavefront sensing.

As a demonstration, for a 580 $\times$ 580 μm^2 FOV, we measured aberrations from areas of 19 $\times$ 19, 95 $\times$ 95, 190 $\times$ 190, and 380 $\times$ 380 μm^2 (Fig. 3.6A, i-iv, yellow dashed boxes) and obtained differing corrective wavefronts resulting from the spatially varying aberrations. Quantifying and comparing AO effectiveness by their "AO/No AO" pixel ratio maps (Fig. 3.6A), we found that correcting aberrations from smaller areas provided greater local signal improvement but exhibited faster decay in signal improvement over distance (Fig. 3.6B, i, ii). This was because the corrective wavefront acquired from a small FOV completely cancelled out the local aberrations and led to diffraction-limited imaging of local structures. For structures away from the wavefront sensing region and thus experiencing different aberrations, however, the same corrective wavefront led to substantial residual aberrations that degraded AO performance. In contrast, correcting aberrations from a larger area reduced signal improvement in the center of the area but enlarged the overall area within which signal was enhanced, which now extended over the entire imaging FOV (Fig. 3.6B, iii, iv). Here, the wavefront measured from scanning the guide star over a larger FOV averaged out the local variations and represented the wavefront distortions common to all field positions. As a result, even though the improvement at the center of the wavefront sensing area was not as large, by removing the common aberrations from the entire FOV, this approach led to a larger effective area for AO correction.

Importantly, this approach enabled large-scale imaging of the retina with 3D cellular resolution, as indicated by retinal cell images taken from the center and edge locations

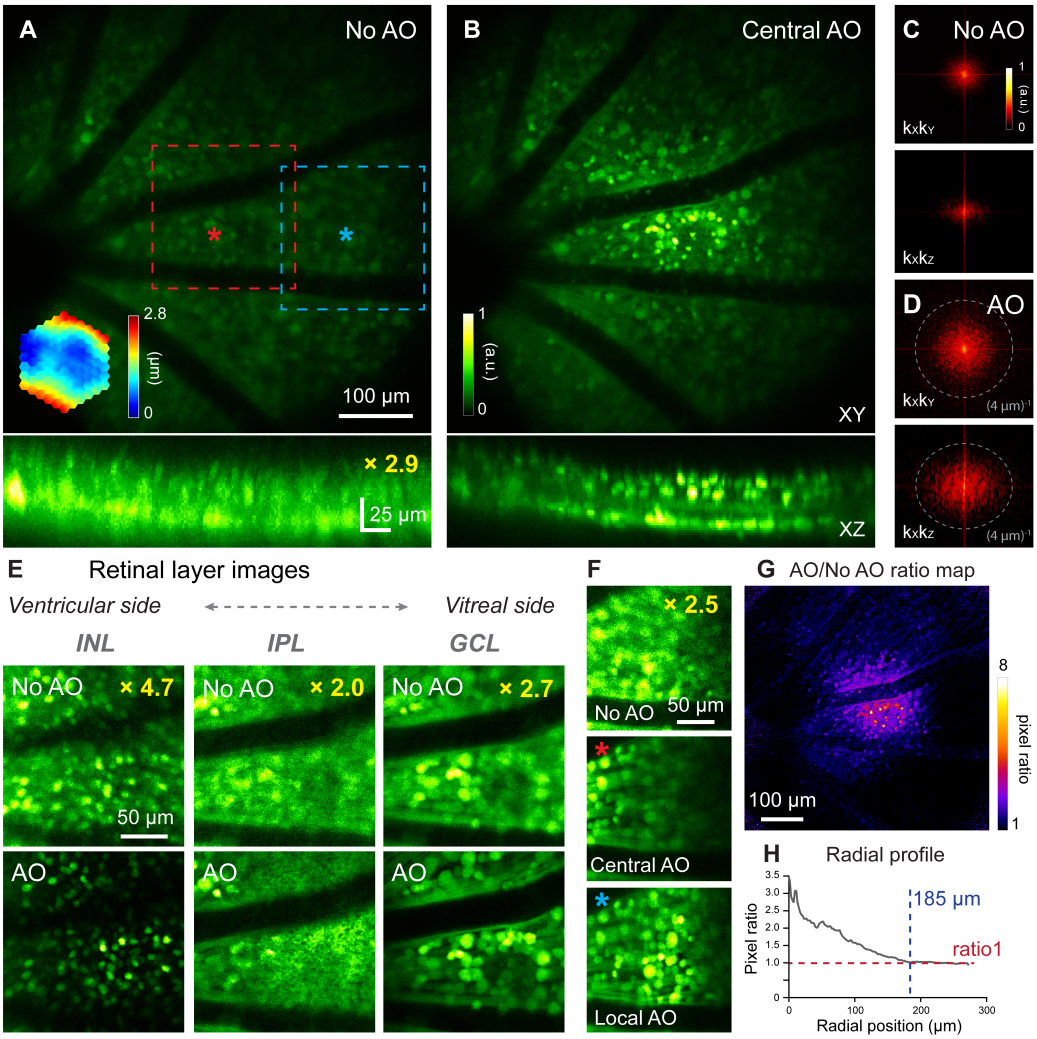

Figure 3.5: ***In vivo*** **imaging of mouse retinal neurons with AO-2PFM.** (A,B) MIPs of image stacks ($580 \times 580 \times 80\ \mu m^3$) of a Thy1-YFP-16 retina, measured (A) without and (B) with AO, respectively, normalized to AO image. Red asterisk: center of a $19 \times 19\ \mu m^2$ WS area. Top: lateral (XY) MIPs. Bottom: axial (XZ) MIPs; 'No AO' image brightness artificially increased by 2.9× for visualization. (C,D) $k_x k_y$ and $k_x k_z$ spatial frequency representation of images in (A,B). (E) Images of different retinal layers within the red dashed box in A acquired (top) without and (bottom) with AO, respectively, normalized to AO image. INL: inner nuclear layer; IPL: inner plexiform layer; GCL: ganglion cell layer. INL/GCL: MIPs of 4.9/7.8-μm-thick image stacks; IPL: single image plane. 'No AO' image brightness artificially increased for visualization (gains shown in each image). (F) Single image planes in GCL at FOV edge (blue dashed box in A) acquired (top) without AO, (middle) with central AO (WS area centered at red asterisk in A), and (bottom) with local AO (WS area centered at blue asterisk in A), respectively. Images normalized to local AO image. 'No AO' image brightness artificially increased by 2.5× for visualization. (G) AO/No AO pixel ratio map. (H) Radially averaged profile of pixel ratio map, centered at red asterisk in A.

(Fig. 3.6C). A more localized wavefront correction (e.g., AO [i], Fig. 3.6C) gave rise to sharper images at the scanning center (Fig. 3.6C, insets a), while a more global wavefront measurement (e.g., AO [iv], Fig. 3.6C) benefited more the visualization of neurons towards the edge of the FOV (Fig. 3.6C, insets b and c). Moreover, with global corrections, neuronal images at the center of the area maintained cellular resolution despite reduction in signal gain (Fig. 3.6C, insets a). Our results suggest that for diffraction-limited imaging of fine structures within a small FOV, a localized wavefront measurement is required, whereas a global wavefront measurement is preferable for 3D cellular resolution imaging over large FOVs.

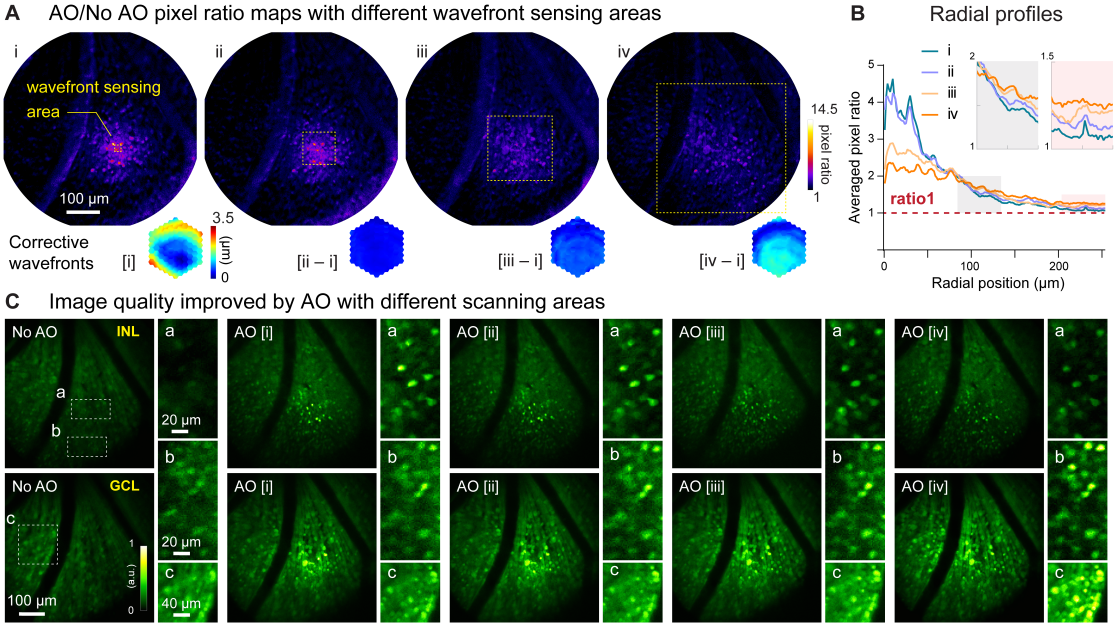

Figure 3.6: Larger WS areas enlarges the effective region of AO correction for 3D cellular resolution imaging. (A) Top: AO/NoAO pixel ratio maps for corrections with differently sized WS areas (yellow dashed boxes; i, 19 × 19 μm^2; ii, 95 × 95 μm^2; iii, 190 × 190 μm^2; iv, 380 × 380 μm^2). Bottom: (for [i]) corrective wavefront and (for [ii-iv]) difference wavefronts between [ii-iv] corrective wavefronts and [i] corrective wavefront. (B) Radially averaged profiles of pixel ratio maps in (A). Insets: zoomed-in views of shaded areas. (C) Single image planes acquired (top) from INL and (bottom) GCL without and with AO using corrective wavefronts [i-iv], respectively. Insets: zoomed-in views of areas at FOV (a) center and (b,c) edge. All images normalized to AO images (AO [i] for inset a; AO [iv] for inset b,c).

3.6 Identification of abnormal capillaries in a pathological mouse model

Having demonstrated the effectiveness of our AO-2PFM in improving signal, contrast, and spatial resolution for *in vivo* retinal imaging, we utilized our system to study retinal microvascular pathology, using age-related macular degeneration (AMD), a leading cause of visual impairment and vision loss [125], as an example. One important subtype of AMD, retinal angiomatous proliferation (RAP), is characterized by capillary proliferation that originates from the sensory retina and extends into the subretinal space [126]. Replicating the characteristic phenotypes of human RAP, a transgenic mouse model, the very low-density lipoprotein receptor knockout (VLDLR-KO) mouse, has been employed to study the underlying mechanism of RAP. In this model, the gene encoding VLDLR, which mediates anti-angiogenic signaling in retinal vasculature, is knocked out, leading to overgrown intraretinal vasculature and subretinal neovascularization [127, 128]. Fluorescein angiography revealed extensive focal vascular leakage in the VLDLR-KO mouse [127–130], but lacks spatial resolution and optical sectioning capability to identify the 3D location and characterize the structure of the vascular lesions *in vivo*.

We utilized AO-2PFM to image *in vivo* the retina of VLDLR-KO/Sca1-GFP and their wildtype control WT/Sca1-GFP mice, both with vascular epithelial cells in the retina labeled with GFP55. In order to detect microscopic capillary pathologies, we used 19×19 μm^2 wavefront sensing area to achieve diffraction-limited imaging performance, which led to high-resolution images of endothelial cell linings of retinal vessels in both mouse lines (Figs. 5A,B). Interestingly, in the VLDLR-KO/Sca1-GFP retina, images acquired with AO revealed open-ended vessel terminals (Fig. 3.7A, yellow asterisks, insets i-ii), which were not observed in the WT/Sca1-GFP retina (Fig. 3.7B). We further confirmed the presence of such microvascular lesions using *ex vivo* 2PFM imaging of dissected VLDLR-KO/Sca1-GFP retinas (Fig. 3.8). Whereas similarly structured open-ended capillaries were observed in the VLDLR-KO/Sca1-GFP retina, consistent with the *in vivo* investigation, vessel terminals in the wildtype control had close-ended morphology with their ends capped by epithelial cells.

We hypothesized that lesions observed in the VLDLR-KO/Sca1-GFP retina were the locations of dye leakage. To test this hypothesis, enabled by AO, we first located an open-ended lesion in a VLDLR-KO/Sca1-GFP mouse retina (Fig. 3.7C, orange box, inset). Then we retro-orbitally injected the green fluorescent dye FITC into the non-imaged eye, which labeled the blood plasma within the retinal vasculature (Fig. 3.7D). Immediately after dye injection, we observed dye leakage around the lesion site (Fig. 3.7D, orange dashed area). A control experiment was carried out by introducing FITC into the healthy WT/Sca1-GFP mouse retina retro-orbitally, where neither abnormal capillaries nor dye leakage were observed (Fig. 3.7E).

To further study the association between dye leakage and microvascular lesions, we injected the NIR dye Evans Blue (EB) into the retinal vasculature and performed dual-color 2-photon imaging of the VLDLR-KO retina. Similarly to the experiments with FITC, we

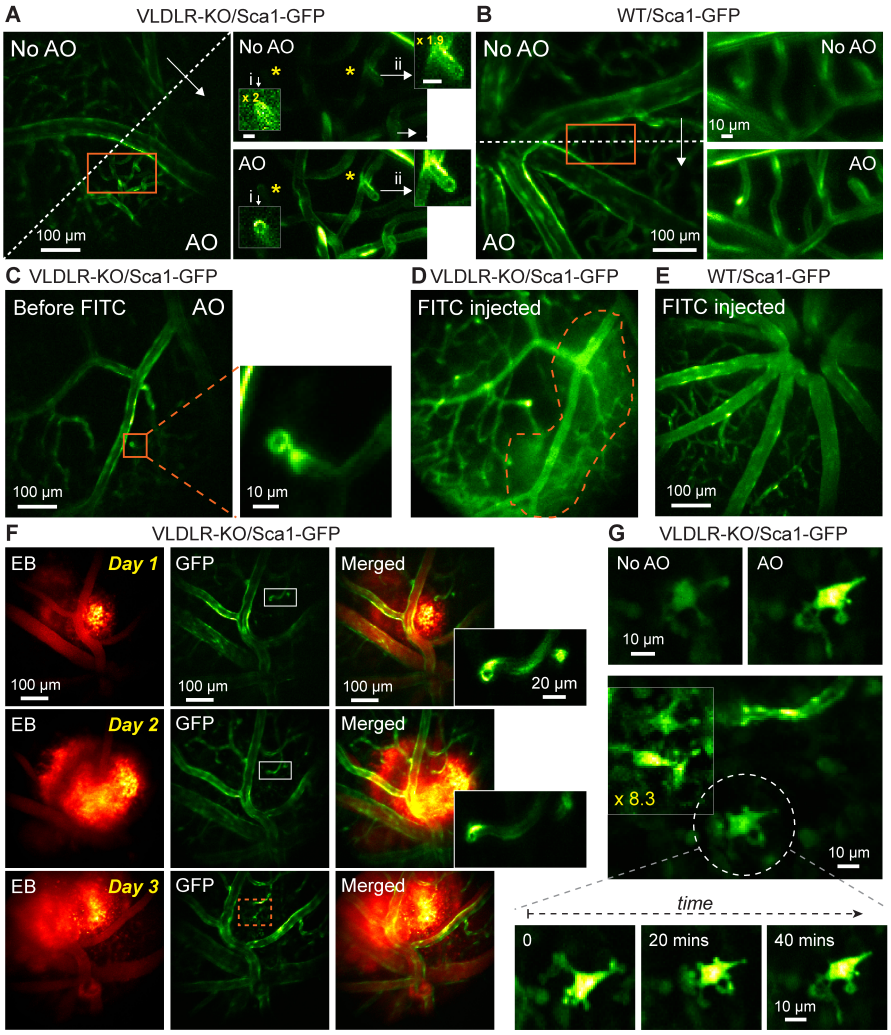

Figure 3.7: *In vivo* vasculature imaging in pathological and healthy retinas. (A,B) Left: MIPs of image stacks of (A) VLDLR-KO/Sca1-GFP ($580 \times 580 \times 94\ \mu m^3$) and (B) WT/Sca1-GFP ($520 \times 520 \times 120\ \mu m^3$) mouse retinas, measured (arrow start) without and (arrow end) with AO. Asterisks: open-ended capillary lesions. Insets: zoomed-in views individually normalized for better visualization. 'No AO' inset brightness artificially increased for visualization (gains shown in inset). (C) A single image plane of a VLDLR-KO/Sca1-GFP mouse retina before FITC injection. Inset: MIP of a zoomed-in image stack ($58 \times 58 \times 8.2\ \mu m^3$) showing open-ended capillary lesion (orange box). (D) The same FOV in (C) after FITC injection. Dashed region: area with heightened fluorescence outside the vasculature. (E) MIP of an image stack ($580 \times 580 \times 150\ \mu m^3$) of a WT/Sca1-GFP mouse retina after FITC injection. (F) Retinal images taken on (top) day 1, (middle) day 2, and (bottom) day 3 after Evans Blue (EB) injection. Left: near-infrared channel showing EB-labeled vasculature and tissue staining (MIP of a $580 \times 580 \times 166\ \mu m^3$ volume). Middle: green channel showing GFP-labeled vasculature (single planes). Right: merged images. Insets: zoomed-in views of gray rectangles from the GFP images (single sections). (G) Microglia observed in EB-injected VLDLR-KO/Sca1-GFP mouse retina on day 3 near the lesion site (orange dashed box in F). Top: microglia imaged without and with AO. Middle: multiple microglia in the leaking region. Signal in the boxed region was artificially increased by 8.3× for visualization. Bottom: time-lapse images of the microglia in white dashed circle. All images are single planes. Wavefront sensing area: $19 \times 19\ \mu m^2$. *In vivo* data in this Figure were obtained from 3 VLDLR-KO and 2 WT mice.

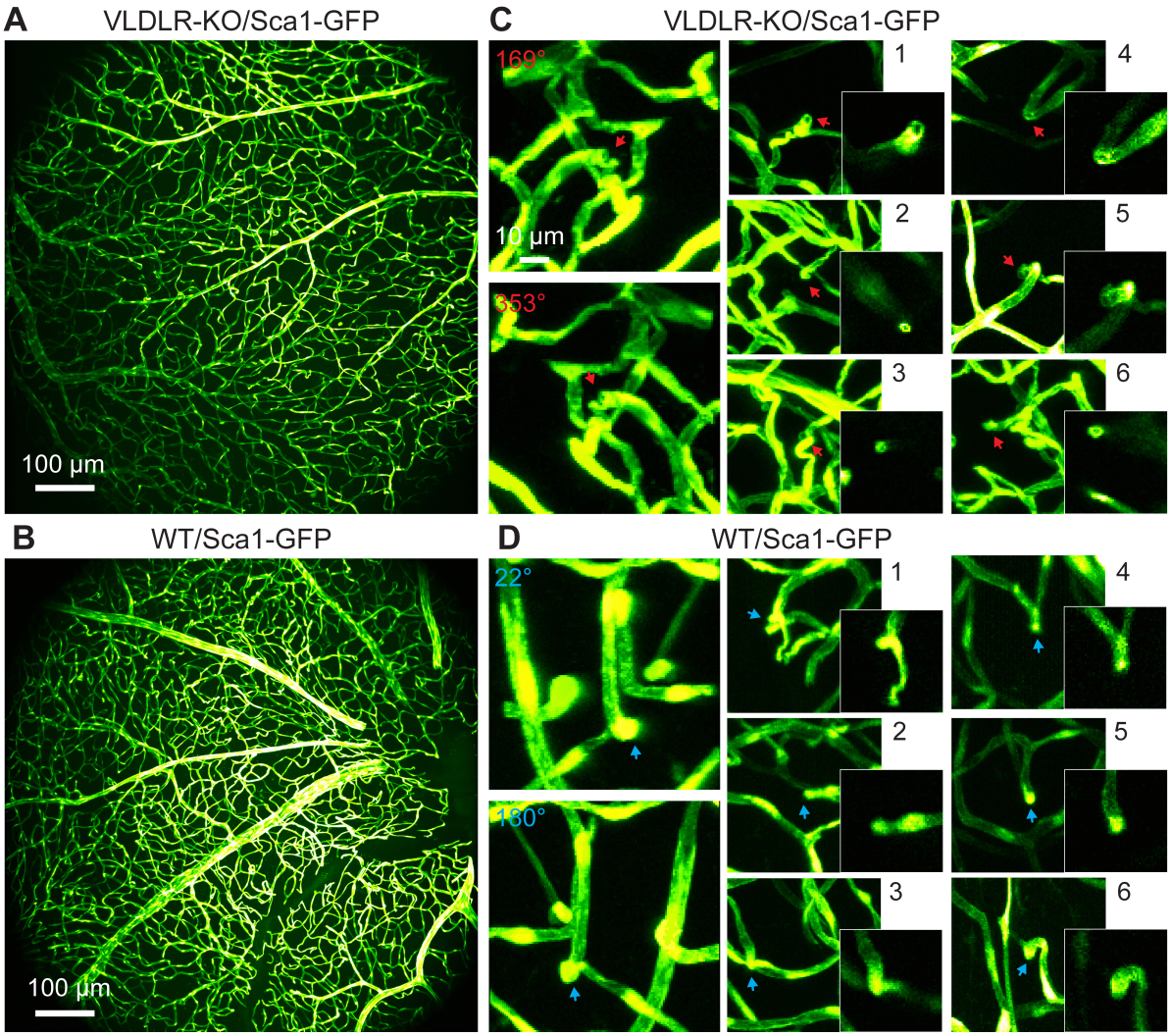

Figure 3.8: *Ex vivo* 2PFM imaging of dissected VLDLR-KO/Sca1-GFP and WT/Sca1-GFP mouse retinas. (A,B) *Ex vivo* MIPs of image stacks from (A) VLDLR-KO/Sca1-GFP (690 × 690 × 82 μm^3) and (B) WT/Sca1-GFP (690 × 690 × 71 μm^3) mouse retinas. (C) Top: 3D projected view of an example capillary opening (red arrow) displayed at viewing angles of 169° and 353°, respectively. Bottom: MIPs of 6 more FOVs showing open-ended capillary terminals (red arrows). Insets: single-plane zoomed-in images. (D) Top: 3D projected view of an example closed-ended capillary (blue arrow) displayed at viewing angles of 180° and 22°, respectively. Bottom: MIPs of 6 more FOVs showing normal capillary structures (blue arrows). Insets: single-plane zoomed-in images. Image contrast was adjusted individually for better visualization.

observed leakage in the knockout mouse retina, with EB persistently staining retinal tissue and the stained volume expanding over three days of consecutive imaging (Fig. 3.7F). We observed capillary lesions (Fig. 3.7F, insets) in the leaking area, indicating a spatial correlation between dye leakage and capillary abnormalities. Moreover, on the third day, we observed microglia within the dye-stained retinal volume that did not show up in previous two days (Fig. 3.7G), suggesting that the leakage of EB triggered local immune response and recruited microglia to the impacted area. In addition, with AO-2PFM, we were able to track morphological changes in the processes of the same microglia at subcellular resolution (Fig. 3.7G, bottom). Control experiment in WT/Sca1-GFP retina showed local small-scale EB leakage (Fig. 3.9), probably resulting from normal remodeling of the retinal vasculature2. Our findings revealed, for the first time, the microscopic morphological details of vasculature lesions and suggested that these open-ended capillary lesions served as intraretinal origins of vascular leakage in the VLDLR knockout mouse. Here AO was essential for 2PFM to achieve high-resolution identification of microvasculature lesions *in vivo*. Together with our optimized sample preparation, AO-2PFM also allowed us to track these lesions, dye leakage, and associated immune response longitudinally, making it possible to investigate the development and progression of vasculature-associated diseases at subcellular resolution *in vivo*.

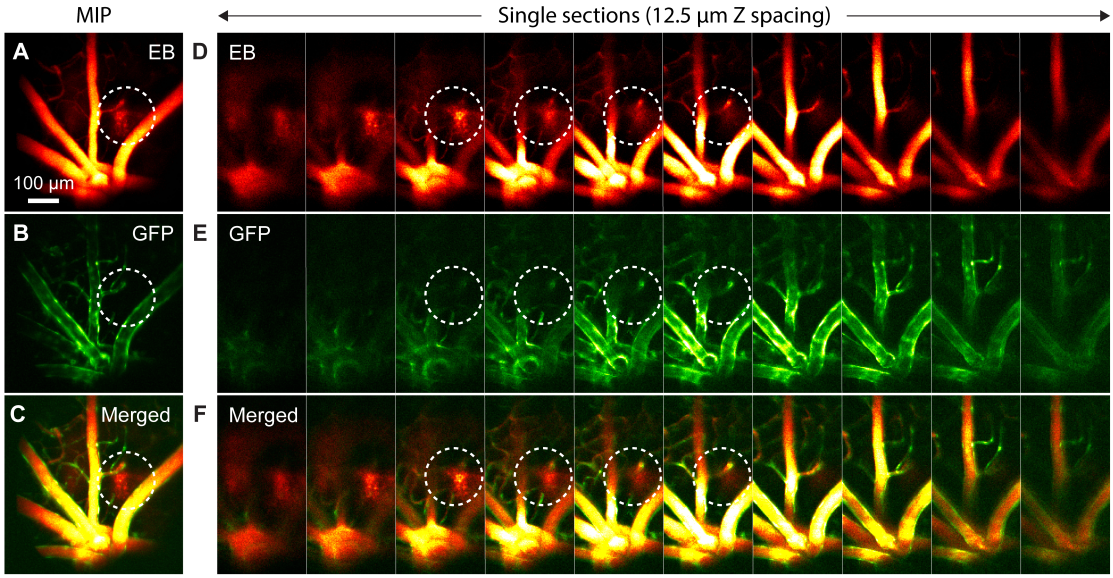

Figure 3.9: ***In vivo*** **AO-2PFM imaging of Evans Blue (EB) leakage in healthy retina.** (A-C) MIPs of image stacks of ($580 \times 580 \times 130$ μm^3) WT/Sca1-GFP retina measured in the (A) near-infrared EB and (B) green GFP channels, and (C) merged images. (D-F) Single-plane images from (A-C) with 12.5 μm^3 Z step. White dashed circles: EB leakage areas.

3.7 Retinal pharmacology imaging

With the 3D cellular resolution imaging capability enabled by AO-2PFM, we can now image the functional activity of retinal neurons with high fidelity in healthy or diseased retina *in vivo* using activity sensors such as the genetically encoded calcium indicator GCaMP6s56.

As a demonstration, we studied how pharmacological manipulation affects RGC activity *in vivo* in a mouse model of retinal degeneration. As the afferent neurons of the retina, RGCs deliver retinal circuit output to the rest of the brain and play a crucial role in visual perception. RGCs in the rd1 mouse, the oldest and most widely studied animal model of retinal degeneration [131], become hyperactive after photoreceptor death caused by a mutation in the Pde6b gene [132, 133]. Recent studies have suggested that RGC hyperactivity masks light-evoked signals initiated by surviving photoreceptors and impedes remaining light-elicited behaviors [133, 134]. Studying RGC hyperactivity therefore is of great importance both for understanding the pathology of retinal degeneration and for developing pharmacological therapies [135]. However, RGC hyperactivity has been only studied *ex vivo* on dissected retinas [133, 135], preventing longitudinal evaluation of degeneration progression and therapeutic approaches.

Here we characterized RGC hyperactivity *in vivo* and studied the effect of Lidocaine, a use-dependent Na+ channel blocker, on alleviating hyperactivity of RGCs in the rd1-Thy1-GCaMP6s mouse using AO-2PFM and calcium imaging. Because RGC hyperactivity is usually studied by *ex vivo* tools such as multi-electrode array (MEA) or single cell electrophysiology recordings, to establish the calcium signature of RGC hyperactivity, we first carried out simultaneous cell-attached and *ex vivo* 2PFM calcium recordings of hyperactive alpha RGCs in a dissected rd1 mouse retina (Fig. 3.11A). Consistent with previous reports on *ex vivo* retina [133–135], RGC hyperactivity was observed as high-frequency action potentials. In terms of calcium signaling (quantified as calcium response magnitude DF/F, with F being baseline brightness and DF being the difference from baseline brightness), hyperactivity was correlated with a heightened DF/F of the GCaMP6s-expressing soma. A temporally varying firing rate led to fluctuations in the DF/F of its calcium signal. After $\sim$20 seconds of 2% Lidocaine bath perfusion, spontaneous spiking from the RGC was largely suppressed with a DF/F close to 0. After artificial cerebrospinal fluid (ACSF) washout, RGC hyperactivity partially recovered, which was associated with an increase of DF/F magnitude. The observed time course and suppressive effect of Lidocaine application on RGC hyperactivity were consistent with *ex vivo* multi-electrode array (MEA) recordings (Fig. 3.10A,B). The characteristics of the corresponding calcium responses were also observed in 2-photon population imaging of multiple RGCs in dissected rd1 retina (Fig. 3.11B), with the brightness and DF/F of the GCaMP6s-expressing neurons reduced by Lidocaine application and followed by partial or full recovery after washout.

Having confirmed that RGC hyperactivity was associated with heighted calcium levels, we next performed AO-2PFM calcium imaging to directly study how Lidocaine affected RGC hyperactivity *in vivo*. Through the rd1-Thy1-GCaMP6s mouse eye, AO increased

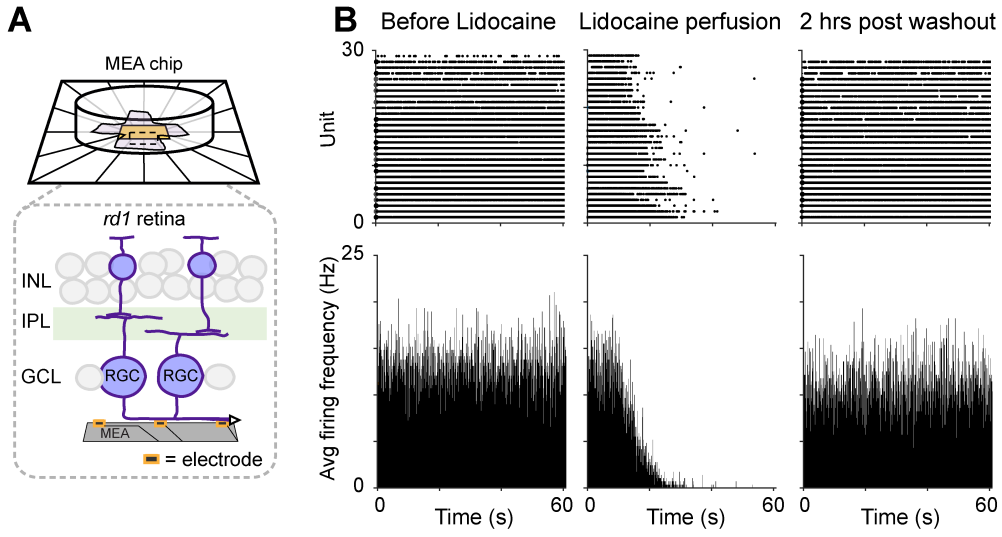

Figure 3.10: *Ex vivo* multielectrode array (MEA) recordings of Lidocaine-modified RGC hyperactivity in rd1-Thy1-GCaMP6s mouse retina. (A) MEA setup for RGC spontaneous spike activity recording. Inset: illustration of retina placement relative to MEA. (B) Raster and average firing frequency plots of RGCs in dissected rd1 mouse retina (left) before and (middle) right after Lidocaine bath perfusion, and (right) 2 hours post washout, respectively.

RGC brightness by on average 4× and enabled high-resolution visualization of both RGC somata and their processes (Fig. 3.11C). The signal increase enabled by AO was particularly important for the rd1-Thy1-GCaMP6s mouse, because the RGCs here had dimmer fluorescence than the other lines that we investigated. For these RGCs, correcting the eye-induced aberration was essential for their visualization and high-fidelity functional investigations at cellular resolution *in vivo*. To maximize the fluorescence signal, we performed AO with a small ($19 \times 19\ \mu m^2$) wavefront sensing area. Before injecting Lidocaine, we observed slow fluctuations in the brightness of GCaMP6s-expressing RGCs (Fig. 3.11D, i), similar to the slow dynamic events in RGC calcium traces measured *ex vivo*. One minute after retro-orbital injection of Lidocaine into the non-imaged eye, hyperactivities from these cells were substantially inhibited for an hour as indicated by the reduction of RGC GCaMP6s fluorescence brightness (Fig. 3.11D, ii and iii). Imaging the same RGCs 60 mins after injection (Fig. 3.11D, iv), we detected partial to complete recovery of RGC brightness, consistent with our *ex vivo* recordings after washing out. Here, by studying the suppression effects of Lidocaine on RGC hyperactivity within living mice, we demonstrated that AO-2PFM can monitor the pathology and pharmacology of retinal diseases at high resolution *in vivo*.

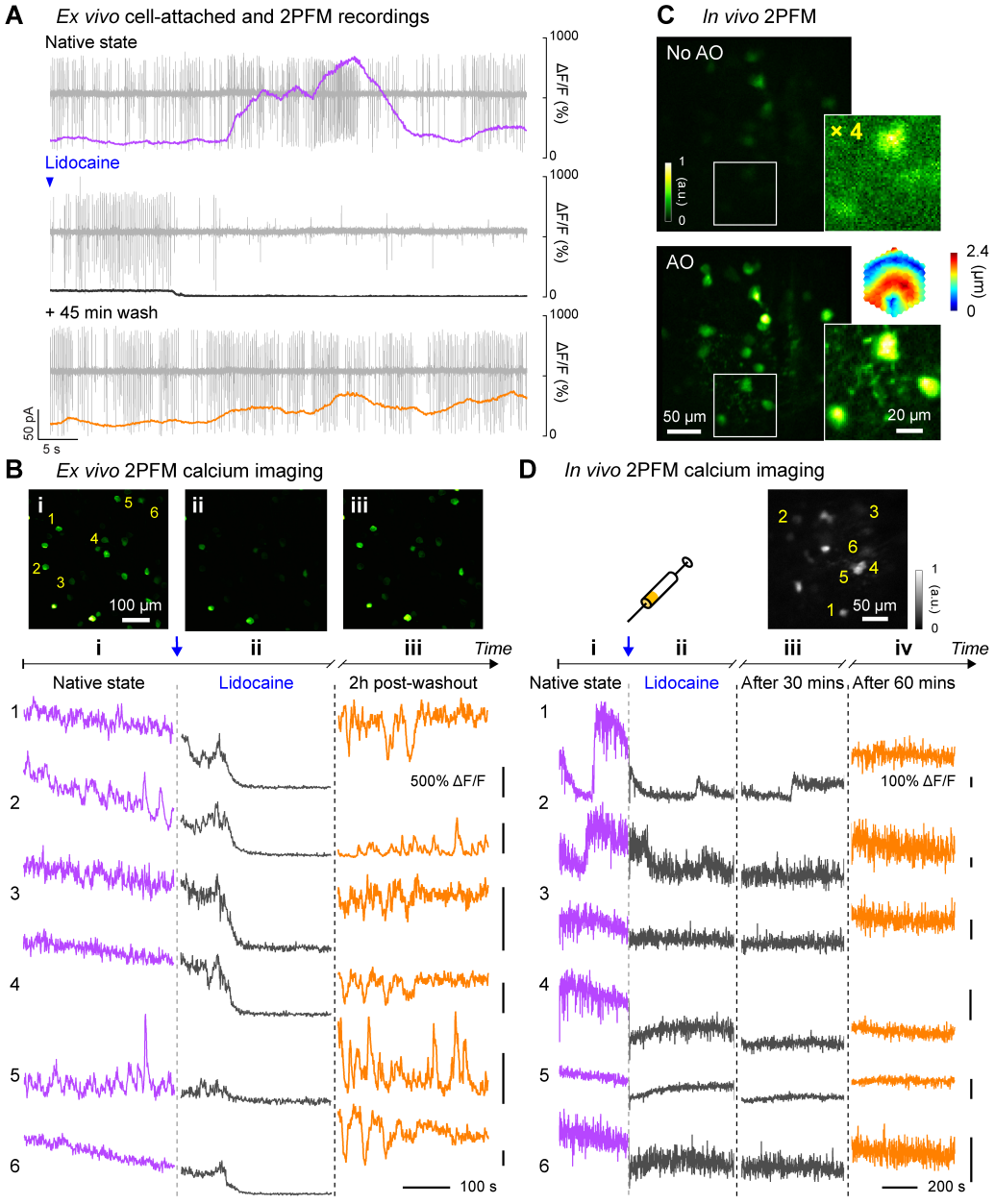

Figure 3.11: *In vivo* calcium imaging of Lidocaine-modified RGC hyperactivity in rd1-Thy1-GCaMP6s mouse retina. (A) Simultaneous cell-attached and 2PFM calcium recordings of a RGC before, during, and 45 mins after Lidocaine treatment. Representative data from ¿ 3 cells. (B) Top: average intensity projections of *ex vivo* 2PFM images of RGCs in a dissected retina (i) before, (ii) right after, and (iii) 2 hours after Lidocaine treatment, normalized to the left image. Bottom: *Ex vivo* calcium dynamics of 6 RGCs therein. Representative data from $>$ 3 retinas. (C) *In vivo* single image planes of RGCs acquired without and with AO, respectively, normalized to AO images. Insets: zoomed-in views and corrective wavefront; 'No AO' inset brightness artificially increased by 4.0$\times$ for visualization. Representative data from $>$ 3 retinas. (D) *In vivo* calcium dynamics of 6 RGCs (i) before, (ii) right after, (iii) 30 minutes after, and (iv) 60 minutes after Lidocaine treatment, respectively. Wavefront sensing area: 19 $\times$ 19 μm^2. Representative data from 1 retina.

3.8 Materials and methods

Animal use

All animal experiments were conducted according to the National Institutes of Health guidelines for animal research. Procedures and protocols were approved by the Institutional Animal Care and Use Committee at the University of California, Berkeley.

AO two-photon fluorescence microscope (AO-2PFM)

The AO-2PFM was built upon a homebuilt 2PFM (Fig. 3.1A) incorporated with a direct-wavefront-sensing-based AO module, as described in detail previously [35]. Briefly, 920-nm output from a femtosecond Ti:Sapphire laser (Coherent, Chameleon Ultra II) was expanded (2×, Thorlabs, GBE02-B) after a Pockel Cell (ConOptics, 350-80-LA-02-BK). The beam was then scanned with a pair of optically conjugated (by L1-L2, FL = 85 mm; Edmund Optics, 49-359-INK) galvanometer mirrors (Cambridge Technology, 6215H). A pair of achromatic lenses (L3-L4, FL = 85 and 300 mm; Edmund Optics, 49-359-INK and 49-368-INK) relayed the galvos to the DM (Iris AO, PTT489). The focal plane position of two-photon excitation in the mouse retina was controlled by an electrically tunable lens (ETL; Optotune, EL-16-40-TC-VIS-5D-C), which was conjugated to the DM (by L5-L6, FL = 175 and 400 mm; Edmund Optics, 49-363-INK and Newport, PAC090). The ETL was then relayed to the pupil of the mouse eye by L7 (FL = 200; Thorlabs, AC254-200-AB) and L8, which was composed of two identical lenses (FL = 50 mm; Thorlabs, AC254-050-AB). The two 50-mm-FL lenses in L8 were used together as a 25-mm-FL lens, and they were mounted with their curved surfaces facing and almost touching each other (Fig. 3.2A,D) to minimize aberrations during large-angle scanning.For 2PFM imaging, the emitted fluorescence from the mouse retina was collected by the mouse eye, travelled through L8-L7 and the ETL, reflected by a dichroic mirror (D2; Semrock, Di02-R785-25×36), focused by a lens (L9, FL = 75 mm; Thorlabs, LB1309-A), and detected by a photomultiplier tube (PMT, Hamamatsu, H7422-40). For direct wavefront sensing, D2 was moved out of the light path and the emitted fluorescence was descanned by the galvo pair, reflected by a dichroic mirror (D1; Semrock, Di03-R785-t3-25×36),and relayed to a Shack-Hartmann (SH) sensor by a pair of lenses (L10-L11, FL = 60 and 175 mm; Edmund Optics, 47-638-INK and 47-644-INK). The SH sensor was composed of a lenslet array (Advanced Microoptic System GmbH, APH-Q-P500-R21.1) and a camera (Hamamatsu, Orca Flash 4.0) that was placed at the focal plane of the lenslet array. Wavefront aberrations were measured from the shifts of SH pattern foci, reconstructed with custom MATLAB code, and the corresponding corrective pattern was then applied to the DM.

System correction

Before imaging the mouse retina, system aberration caused by imperfect and/or misaligned optics was corrected. Due to the path difference between the two-photon illumination and the fluorescence wavefront sensing paths [136], system correction was performed with a modal-based optimization approach [107]. Specifically, with 0 mA applied to the ETL, we imaged a fluorescent lens tissue sample at the focal plane of L7 and applied 11 values (-0.1 $\sim$ 0.1 μm rms at an increment of 0.02) for each of the first 21 Zernike modes excluding piston, tip, tilt, and defocus. The optimal value for each Zernike mode was determined by maximizing the fluorescence intensity of the sample and it was applied to the DM before proceeding to the next Zernike mode. An SH pattern was obtained with system aberration corrected and was used as the SH reference for calculating sample-induced aberrations. All images taken with system correction were indicated in the main text as "No AO".

To change the focal plane within the retina, we varied the electric current applied to the ETL. We characterized how system aberrations varied with the ETL current (Fig. 3.2). We carried out system correction with 0 mA ETL current applied. Additional aberrations introduced by setting ETL current to 20, 40, 60, and 80 mA were negligible (Fig. 3.2B) compared with eye-induced aberrations and minimally affected *in vivo* imaging (Fig. 3.2C). We also evaluated how system aberrations varied with the distance D between the mouse eye pupil and the imaging module (Fig. 3.2D). Using Zemax® for ray tracing, we found its effect to be similarly minimal (Fig. 3.2E). Our typical *in vivo* retinal imaging was performed with 10$\sim$60 mA of ETL currents and 2$\sim$4 mm D values (Fig. 3.2D). Simulating the mouse eye as an ideal lens behind a 0-diopter contact lens (Fig. 3.3A) made of PMMA (1.49 refractive index) and 0.5-mm-thick eye gel (1.33 refractive index), we calculated the focal shift and FOV for different ETL current using Zemax® and found a linear focal shift with ETL current and relatively constant FOV during 3D imaging (Fig. 3.2F). Imaging FOV and axial shift were determined from Zemax® simulation for D = 2 mm.

***In vivo* imaging**

All mice (Wild-type C57BL/6J and Thy1-YFP-16, the Jackson laboratory; VLDLR-KO/Sca1-GFP and WT/Sca1-GFP, Gong lab; GCaMP6s-rd1, Kramer lab) were at least 8 weeks old at the time of imaging. *In vivo* imaging was carried out on mice under isoflurane anesthesia ($\sim$ 1.0% by volume in O_2). Prior to imaging, the mouse pupil was dilated with one drop of 2.5% phenylephrine hydrochloride (Paragon BioTeck, Inc) and one drop of 1% tropicamide (Akorn, Inc). A 0-diopter customized rigid contact lens (Advanced Vision Technologies) was placed on the eye, with eye gel (Genteal) applied in between the eye and the contact lens to prevent cornea drying and clouding. Excessive eye gel was removed by gently pressing the contact lens onto the mouse eyeball. One single application of eye gel was sufficient in keeping the cornea moist for a 2$\sim$4-hour imaging session. During imaging, mice were stabilized on a bite-bar on a 3D translational stage with two rotational degrees of freedom (Thorlabs, PR01) and the body temperature was maintained with a heating pad (Kent Scien-

tific, RT-0515). The mouse head was carefully aligned to make the eye perpendicular to the illumination beam, minimizing off-axis aberrations and illumination clipping by the contact lens and mouse pupil. Fluorescent dyes were injected retro-orbitally into the non-imaged eye. In wild-type mice, 40-80 μL of 5% (w/v) 2M-Da dextran-conjugated FITC was injected for vasculature visualization. In some VLDLR-KO/Sca1-GFP mice, 30-40 μL of 5 mg/mL FITC or 5 mg/mL Evans Blue were injected. To generate bright enough fluorescent guide star for direct wavefront sensing in the weakly-fluorescent mouse line rd1-Thy1-GCaMP6s, 20-40 μL of 5 mg/mL Evans Blue was injected. To suppress RGC hyperactivity in rd1-Thy1-GCaMP6s mouse retina, we retro-orbitally injected 10 μL of 2% Lidocaine into the non-imaged eye.

Retina dissection

Mice were first euthanized by isoflurane overdose followed by cervical dislocation. Then the eyes were removed, and the retinas were isolated and immersed in standard oxygenated (95% O_2, 5% CO_2) artificial cerebrospinal fluid (ACSF) at room temperature and pH 7.2.

Multielectrode array (MEA) recordings

Isolated *ex vivo* rd1-Thy1-GCaMP6s retinas were cut into three pieces. Each piece was mounted onto a 60-electrode MEA chip (60ThinMEA200/300iR0ITO, Multichannel Systems) with the inner retina facing the array, so that RGCs were in close contact with electrodes. The chip was connected to an amplifier (MEA1060, Multichannel Systems) for wide-band extracellular recording of multi-unit activity. Before the onset of recording, the retina was perfused with oxygenated ACSF at $34°C$ for 30 min with a flowrate of 1 mL/min. For pharmacological blockade of actional potentials, Lidocaine (2% in saline) was applied to the bath during corresponding recordings. Washout of lidocaine was performed by continuously perfusing oxygenated ACSF at $34°C$ over the course of two hours with a flowrate of 1 mL/min. Recorded activity from RGCs were high-pass filtered at 200 Hz, digitized at 20 kHz, and analyzed offline. Extracellular spikes were defined as transient signals with peak deflection of >3.5 standard deviations from the root mean square of background signal. Because individual electrodes can detect spikes from multiple RGCs, we utilized principal component analysis to sort unique units (Offline Sorter v3, Plexon), which accepted units having interspike intervals >1 ms and each unit compiled into a raster plot. The analysis code for processing sorted spike data into rasters is available online (https://github.com/kookstance/Multielectrode-array).

Cell attached recordings of alpha-RGCs in rd1-Thy1-GCaMP6s retinas

Isolated *ex vivo* rd1-Thy1-GCaMP6s retinas were mounted onto filter paper (0.45 mm nitrocellulose membranes, MF-Millipore) with an optical window with the ganglion cell layer facing up. RGCs were visualized with DODT contrast infrared optics (Luigs and Neumann) and were targeted for whole cell recording with glass electrodes (4-6 MΩ) filled with ACSF.

Loose- (< 1 GΩ) and tight-seal patches (> 1 GΩ) were obtained under voltage clamp with the command voltage set to maintain an amplifier current of 0 pA. Input resistance and series resistance were monitored throughout recording to ensure stable recording quality and cell health.

Image processing and analysis

All image processing, visualization, and analysis were performed in ImageJ (NIH). To remove motion-induced artifacts, image registration (TurboReg and StackReg plugins) was performed.

3.9 Discussion

By optimizing optical design and sample preparation and using direct wavefront sensing AO to correct mouse eye aberrations, we demonstrated here the first *in vivo* visualization of retinal synaptic structures, the first *in vivo* identification of capillary lesions with sub-capillary details, and the first *in vivo* detection of RGC hyperactivity and its suppression by pharmacological reagents.

To image mouse retina *in vivo* with 2PFM, one can either utilize a standard objective lens [101, 117] or the mouse eye's optics itself [20, 105] to focus the excitation light and collect the fluorescence emission. The former approach requires long-working-distance objective lenses and, more importantly, suffers from severe aberrations caused by the refractive power of the ocular optics (mostly crystalline lens, as cornea was typically flattened in these systems). For this reason, to achieve the best image quality and the largest FOV size, using mouse eye itself as the focusing element as implemented here is preferable.

Among the studies that used the mouse eye optics for imaging, discrepancies exist in how large the mouse ocular aberrations are and how essential AO is for vasculature and cellular imaging in the mouse retina. For the multiple mouse strains investigated here (i.e., wild-type (C57BL/6), Thy1-GFP line M, Thy1-YFP-16, VLDLR-KO/Sca1-GFP, WT/Sca1-GFP, and rd1-Thy1-GCaMP6s), we found that their ocular aberrations were typically within the range of 3$\sim$5 μm peak-to-valley (P-V; after excluding tip, tilt, and defocus) and 0.4$\sim$0.8 μm rms without notable differences in severity across strains. While consistent with most previously reported values[103, 107], our study differs significantly from a recent AO-2PFM study, which reported extremely large aberrations (e.g., 12-25 μm P-V26) and found AO to be essential for resolving microvasculature and cell bodies in 2D or differentiating retinal layers *in vivo*. In contrast, with our carefully designed microscope and system aberration correction procedure, we achieved capillary visualization, 2D single-cell resolution, and retinal layer differentiation by only correcting system aberrations ('No AO' in our case). Given that our system aberrations were much smaller than mouse ocular aberrations, our study indicated that a well-engineered 2PFM like ours should be sufficient for *in vivo* retinal imaging applications requiring only capillary and 2D cellular resolution.

One factor that strongly impacted image and wavefront sensing quality was the sample preparation procedure. We found that our specially designed 0-diopter contact lens encircled with a supportive flat base were essential for high-quality imaging by 2PFM without AO (Fig. 3.3). Similar improvement in imaging quality by 0-diopter contact lens was reported previously for *in vivo* optical coherence tomography imaging of the rat retina, where it was hypothesized that the application of the contact lens smoothed corneal defects and reduced wavefront error of the anterior segment of the eye [137]. The supportive flat base encircling the optical zone of our contact lens [138] and the gel completely separated the eye surface from air and prevented cataract formation for hours. Together, they enabled high-quality SH images and accurate corrective wavefronts to be acquired throughout the experiment.

Incorporating direct-wavefront-sensing-based AO with 2PFM, we found that location-dependent aberrations led to local improvement in the mouse retina *in vivo*. To enlarge the high-resolution area enabled by AO, one way is to stitch images from smaller areas, each with its own local AO correction44,45,64. However, this procedure can be time-consuming and thus nonideal for *in vivo* functional studies. By scanning differently sized areas for wavefront sensing, we identified a trade-off between AO performance (i.e., resolution and signal enhancement) and effective area. We demonstrated that a single corrective wavefront acquired by scanning the guide star over a more extended area led to 3D cellular resolution imaging over a larger retinal volume, simplifying the procedure for future functional studies of neuronal populations in the retina. It is worth noting that, instead of incorporating scan lenses optimized for large scanning angles, our homebuilt 2PFM system utilized regular achromatic doublet lenses, which reduced cost but limited the overall imaging FOV of our microscope. The effective AO area and imaging FOV would be further increased by incorporating high-performance scan lenses.

To study retinal pathologies for physiological and clinical insights, it is ideal to conduct longitudinal investigations *in vivo*. Importantly, to probe microscopic early-stage pathologies, high spatial resolution is needed. In human applications, investigation of retinal vascular abnormalities are limited to capillary resolution65,66. Sub-capillary morphology and dynamics of the mouse retina were recently observed by light-sheet microscopy, however with *ex vivo* preparations67. To our knowledge, sub-capillary features had not been observed in the living mouse eye previously. In this work, applying AO-2PFM, we studied retinal vasculature in a pathological mouse model with over-grown blood vessels at sub-capillary details *in vivo*. Recovering diffraction-limited resolution, AO enabled us to identify capillary lesions as open-ended terminals that were associated with dye leakage in 2-photon fluorescence angiograms. Moreover, the repeatable and reliable AO performance allowed us to track the same retinal region over multiple days and discover lesion-associated immune response and microglia migration at subcellular resolution. Our results show far-reaching potential of AO-2PFM for mechanistic understanding and early diagnosis of retinal diseases.

We also applied our AO-2PFM to *in vivo* activity imaging of RGCs in a mouse model of retinal degeneration. Due to the dimmer brightness of the fluorescence indicator in this model, AO was essential in increasing signal strength and enabling high-sensitivity interrogation of the effects of pharmacological manipulation on RGC hyperactivity. Traditionally,

pharmacological effects on retina are studied by electrophysiological and imaging tools on *ex vivo* retinal preparation, or *in vivo* by indirect assessments downstream in the visual pathway or through behavior test60. Taking retinal degeneration as an example, treatment-induced photosensitization enhancement has been mainly evaluated through electrophysiology or *ex vivo* imaging of dissected retinas. AO-2PFM enabled us to evaluate how pathological RGC hyperactivity was suppressed by an example pharmacological agent, lidocaine, at single cell level noninvasively. Together with the capability for longitudinal investigations discussed above, we envision that the AO-enabled high-sensitivity subcellular and cellular 2PFM imaging would become a highly enabling technology for pathological and pharmacological investigations of the mouse retina *in vivo*.

Chapter 4

Precise measurements of neuronal activity in V1 by two-photon *in vivo* imaging[1]

4.1 Introduction

As one of the most valuable sensory modalities and neurological systems, vision has received substantial attention in brain studies. Although experiments have been conducted extensively yielding numerous discoveries on how our brain integrates, processes and relays the visual signals, the process by which the information is encoded and decoded by neurons in cortical circuitry is still under explored. Existing data of neuronal activity in response to visual stimuli are typically obtained from anaesthetized animals by electrophysiological recordings of unknown cell types and laminar locations. With the limited size and density of microelectrodes, such recordings failed to track the large neuronal population activity simultaneously. Compared to electrophysiology, *in vivo* calcium imaging by 2PFM provides superior spatial resolution with cell-type specificity and the ability to monitor the neural circuitry dynamics across hundreds to thousands of neurons. Furthermore, with multi-color imaging using a combination of fluorescent proteins whose emissions can be separated, 2PFM also allows neuroscientists to characterize the neuronal circuit dynamics as well as synaptic dynamics, e.g. V1 neurons and their thalamocortical afferent inputs. My research focuses on characterizing V1 dynamics by 2PFM to support and validate related V1 models. First, I collected large-scale data sets by measuring the orientation tuning properties of cortical neurons in V1 and their thalamic inputs. Next, I analyzed the data to investigate the correlations in activity among neurons and the spatial organization of their tuning properties.

[1]Adapted from "Yu, P., Yang, Y., Gozel, O., Oldenburg, I., Dipoppa, M,., Rossi, F., Miller, K., Adesnik, H., Ji, N., & Doiron, B. (2022). Circuit-Based Framework for Fine Spatial Scale Clustering of Orientation Tuning in Mouse V1 [Manuscript in preparation]."

4.2 Measuring fine spatial scale clustering of orientation tuning in L2/3 and L4 of mouse V1

In this section, I present how we imaged neuronal activity in V1 and investigated the spatial organization of orientation tuning in V1 by 2PFM.

As a major feature of V1 neurons, orientation selectivity (OS) has raised significant attentions among neuroscientists since it was discovered by Hubel and Wiesel in 1963 [72]. Unlike higher mammals (such as primates and cats) in which the OS of V1 neurons are spatially organized in columnar maps [139–141], the orientation preferences in rodents was believed to have no clear spatial organization, and rather form a "salt-and-pepper" map [139, 142]. However, recent studies [75, 143] revisited this problem and challenged the view of unordered spatial layout of OS in mouse. The studies characterized the correlative tuning properties among mouse V1 neurons and found that the tuning similarities of neuron pairs are statistically dependent on their cortical distance forming a spatial clustering, rather than a strict salt-and-pepper map. However, the spatial scale of the clustering is still unclear: either spread over hundreds of microns [75], or limited to the scale of tens of microns [143]. The aim of this work is to resolve this controversy by using 2PFM to accurately characterize the orientation tuning similarity in mouse V1. We found significant tuning similarities among nearby neurons localized within $\sim 20\ \mu m$ in both L2/3 and L4. It decays as a function of the horizontal cortical distance with a spatial width $\lambda \sim 7\ \mu m$. We discovered that the controversy over the spatial width in the literature can be explained by the improper neuropil subtraction leading to spurious correlations among neurons. We investigated the problem of neuropil contamination by collecting data from L2/3 neurons expressing nuclear-targeted GCaMP6s.

4.2.1 Micro-clustered organization of orientation tuning

To investigate the spatial organization of orientation tuning in V1, we presented circular sinusoidal gratings drifting in 12 directions (at 30° increments) to awake mice. Each grating stimulus was repeated 10 times in a pseudorandom sequence, interleaved by a period of uniform blank screen (see Methods). We first recorded visually evoked calcium responses of neurons in V1 L2/3 expressing cytosolic GCaMP6s in wild-type mice (Fig. 4.1). For each image sequence, neurons were detected and outlined by Suite2p [77] with overlapped neurons manually removed (Fig. 4.1A). The calcium transient $\Delta F(t)/F_0$ was calculated for each neuron with an optimal neuropil subtraction method (as described in the next section). This signal was averaged over the 10 trials to obtain the visual response to each stimulus angle and compose the tuning curve. The tuning curves were fitted with a bimodal Gaussian function (Fig. 4.1B). Strongly responsive neurons (max trial-averaged $\Delta F(t)/F_0 > 0.1$) with significant angular preference across the 12 directions (one-way ANOVA test $p < 0.05$) and well fitted tuning curves (see Methods) were included as orientation selective for further analysis of spatial organization. Among 9936 L2/3 neurons recorded from 10 imaging

planes in 2 mice, 22.6% were labeled as OS with the preferred orientations distributed over the full range of stimulus from 0° to 180° (upper panel, Fig. 4.1B). In middle panel of Fig. 4.1B, we present tuning curves of 15 randomly selected neurons normalized relative to their preferred direction, demonstrating varying tuning shapes across different neurons. The neuronal tuning properties were quantified by calculating their orientation selectivity index (OSI, see Methods). The OSI distribution of OS neurons indicates robust orientation selectivity in mouse V1 with a mean value near 0.44, matching past reports [73, 144–147].

An orientation selectivity map for each image plane was constructed with OS neurons color-coded by their preferred orientation (Fig. 4.1A). Visual inspection suggests no clear spatial organization, i.e. a salt-and-pepper map, as previously believed [73, 144]. However, recent studies demonstrated tuning correlations of V1 neurons [75, 143] with the spatial scale still under debate. To resolve the controversy, we carefully characterized the orientation tuning similarity between each pair of neurons (Fig. 4.1D, E). We first quantified the tuning curve correlations between neuron pairs versus their horizontal cortical distance, by calculating the dot product of their tuning curves (Fig. 4.1D). Unlike a salt-and-pepper map assuming independent tuning similarity of cortical distance, our result shows that the tuning curve correlation is strong among neighboring neuron pairs ($< 10\ \mu m$), but quickly decays to zero when the distance is greater than $\sim 20\ \mu m$. We then calculated the difference of preferred orientation angles between each neuron pair versus their distance (Fig. 4.1E). Consistent with tuning curve correlations, we observed a similar trend: the curve in Fig. 4.1E starts from a small preferred angle difference (high similarity) and converges to 45° (low similarity) with the increasing distance. The two curves in Fig. 4.1D, E were exponentially fitted with spatial widths of $\lambda \sim 7\ \mu m$. Our tests suggest strong and significant correlations among neighboring neurons, rather than a strict salt-and-pepper map. We call this spatial organization a "micro-cluster" with "micro" emphasizing the small spatial scale typically overlooked in the literature.

L2/3 neurons receive feedforward projection from L4 neurons in addition to recurrent projection from other L2/3 neurons. We therefore asked whether the micro-clustered structure is an inherited property from a similar spatial organization in L4. To separate L4 neurons from other neurons in V1, we used Scnn1a-Tg3-Cre transgenic line [148] to specifically label L4 with Cre-dependent cytosolic GCaMP6s. We used the same experimental pipeline and data analysis methods to characterize L4 neuron tuning properties (Fig. 4.2). Among 4684 L4 neurons recorded from 18 imaging planes in 2 mice, 56.6% neurons were labeled as OS and used for spatial organization analysis (Fig. 4.2A-C). Similar to what we observed in L2/3, L4 neuron pairs also have strong correlations (Fig. 4.2D) and similar preferred orientation angles (Fig. 4.2E) when they are close to each other. The micro-cluster structure was observed in L4 as well indicating the inheritance of the spatial organization from L4 to L2/3. The spatial width of the "cluster" in L4 ($\lambda \sim 9\ \mu m$, Fig. 4.2D, E) is slightly larger than L2/3 ($\lambda \sim 7\ \mu m$, Fig. 4.1D, E), which suggests that the recurrent circuitry in L2/3 plays a non-trivial functional role, rather than unconsciously inhering the pattern from L4 circuits.

To better characterize and visualize the micro-clusters, we picked out each group of

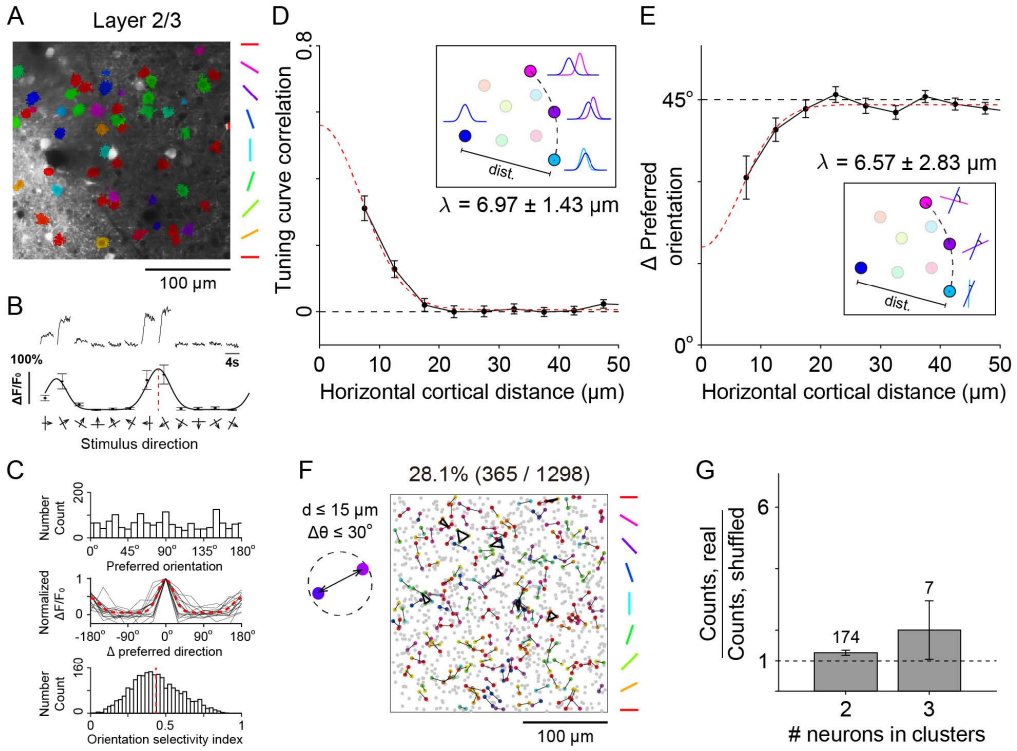

Figure 4.1: Micro-clustered spatial organization of orientation tuning over a fine spatial scale in L2/3 of mouse V1. (A) An example fluorescence image plane of cytosolic GCaMP6s L2/3. Neurons are color coded by their preferred orientations. (B) Calcium responses to the visual stimuli for an example OS neuron in L2/3. Top: Trial-averaged calcium transients in response to 10 repeats of 12 directions of drifting gratings. Bottom: Time-averaged calcium transients of the top panel (tuning curve). Red dashed line indicates the preferred direction. (C) Top: distribution of the preferred orientation of all L2/3 orientation selective (OS) neurons (n = 2246). Middle: normalized tuning curves relative to preferred directions of 15 random selected neurons (gray) and the average of all L2/3 OS neurons (red). Bottom: distribution of orientation selectivity index (OSI) for all L2/3 OS neurons. Red dashed line indicated the mean value (0.435). (D) Tuning curve correlation of neuron pairs as a function of their horizontal cortical distance (black) and the exponential fitted curve (red) with fitting function $A \cdot \exp(-d^2/2\lambda^2) + b$, where λ is the spatial width. Inset: illustration of the tuning curve correlations for multiple pairs of neurons with the same distance. (E) The difference of preferred orientation angles of neuron pairs as a function of their horizontal cortical distance (black) and the exponential fitted curve (red). λ: the same as in (D). Inset: illustration of difference of preferred orientation angles for multiple neuron pairs with the same horizontal cortical distance. (F) L2/3 OS neurons that belong to any micro-clusters (distance $< 15\ \mu m$ and preferred orientation difference $< 30°$) are interconnected with black lines and colored-coded by their preferred orientations. Gray dots are neurons that don't belong to any micro-clusters. Neurons from different imaging planes and different mice were vertically stacked. The number above the figure indicates the proportion of neurons within any micro-clusters. (G) The ratios of actual counts of L2/3 micro-clusters (numbers above the bars) of different sizes (2: pair; 3: triplet) to that of randomly shuffled data.

neurons that can form a micro-cluster and interconnected them (Fig. 4.1F, G; Fig. 4.2F, G). Each neuron in the group should have similar preferred orientation angle (Δ Pref. angle $< 30°$) to others and close (distance < 15 μm) to at least one another neuron. Most of such group were composed of either 2 neurons (pair) or 3 neurons (triplet). We observed that $\sim 28\%$ of neurons in L2/3 and L4 were identified as a member of one micro-cluster (Fig. 4.1F; Fig. 4.2F). We counted the number of pairs and triplets in L2/3 and L4 (Fig. 4.1G; Fig. 4.2G), which is significantly higher than shuffled data. This analysis further demonstrates the micro-clustered spatial organization of orientation tuning and contradicts salt-and-pepper map.

4.2.2 Neuropil subtraction for characterizing the spatial scale of clustering

Despite the fact that the spatially correlative tuning properties in V1 have already been discovered, research groups have disagreed on the scale of the spatial clustering as either spread over hundreds of microns [75] or limited to tens of microns [143]. After carefully examining our data analysis pipeline, we believe the controversy was caused by improper neuropil correction methods when extracting calcium transients from the image sequence. In 2PFM imaging, the recorded fluorescence signals from cell bodies are contaminated by the surrounding neuropils, such as axons and dendrites [74]. Therefore, neuropil subtraction is essential for having precise measurements of neuronal activity. As we explain below, underestimating or overestimating neuropil signals could alter the calculated tuning properties of neurons and lead to strong but spurious correlations over both a small and a long spatial range.

Our neuropil subtraction method was adopted from Dipoppa et al [78]. To estimate the neuropil signals, we defined a square neuropil mask extending 30 μm from each cell's center. The neuropil signal is calculated as the averaged signal in the mask excluding pixels from any detected cells. The neuropil signals were subtracted from the raw traces weighted by a neuropil coefficient α (Fig. 4.3A, B): $F(t) = F(t)_{raw} - \alpha \cdot \Delta F(t)_{neuropil}$ (Fig. 4.3C, see Methods). A typical range for the neuropil coefficient is $[0, 2]$, where 0 means no subtraction. The value of α can either be specified based on heuristics [76, 149] or estimated by optimization algorithms [78, 150, 151]. Different algorithms tend to produce different values of α. Before seeking an optimal neuropil coefficient, we first explored how tuning properties of neurons and their correlations are affected by α.

We performed neuropil subtraction as described above on the L2/3 datasets with neurons expressing cytosolic GCaMP6s. With different neuropil coefficients from 0 to 1.25, we plotted the OS map (Fig. 4.3G) and the tuning curve correlation versus the cortical distance (Fig. 4.3H). The spatial clustering appears for all values of α but with different strength and spatial range. When $\alpha = 0$, which means no subtraction, we observed a broad clustering over hundreds of microns on the OS map. Consistent with our visual inspection, the tuning curve correlations between neuron pairs are strong and don't decay much as the increasing

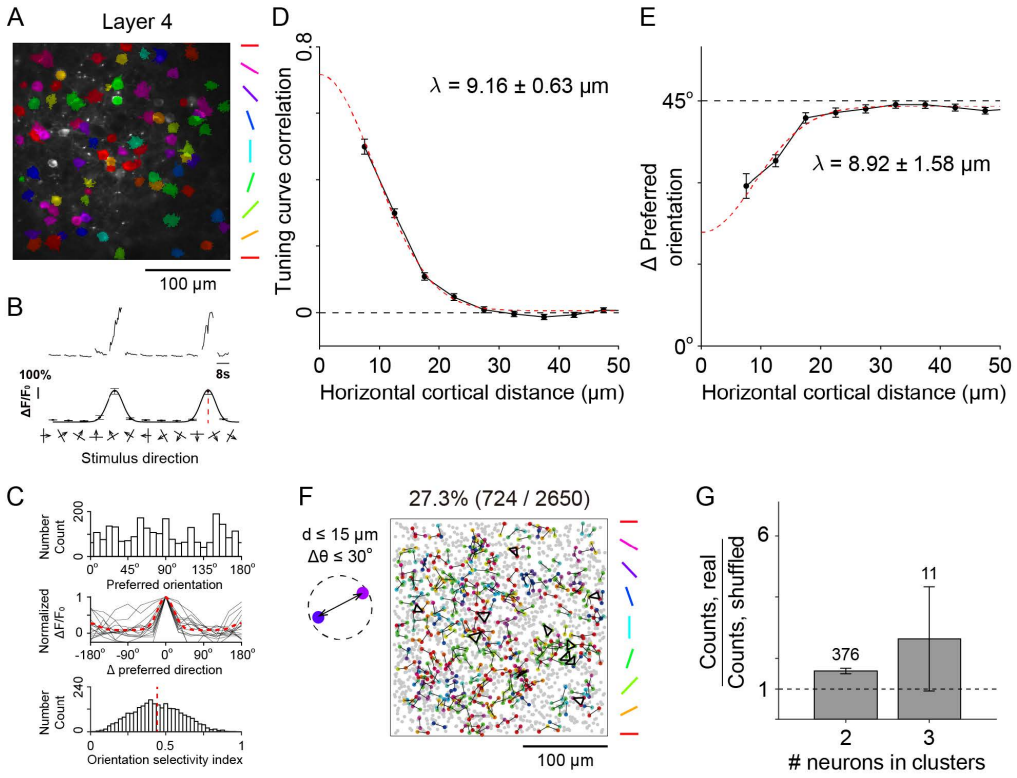

Figure 4.2: Micro-clustered spatial organization of orientation tuning over a fine spatial scale in L4 of mouse V1. (A) An example fluorescence image plane of cytosolic GCaMP6s L4. Neurons are color coded by their preferred orientations. (B) Calcium responses to the visual stimuli for an example OS neuron in L4. Top: Trial-averaged calcium transients in response to 10 repeats of 12 directions of drifting gratings. Bottom: Time-averaged calcium transients of the top panel (tuning curve). Red dashed line indicates the preferred direction. (C) Top: distribution of the preferred orientation of all L4 OS neurons (n = 2650). Middle: normalized tuning curves relative to preferred directions of 15 random selected neurons (gray) and the average of all L4 OS neurons (red). Bottom: distribution of OSI for all L4 OS neurons. Red dashed line indicated the mean value (0.443). (D) Tuning curve correlation of neuron pairs as a function of their horizontal cortical distance (black) and the exponential fitted curve (red) with fitting function $A \cdot \exp(-d^2/2\lambda^2) + b$, where λ is the spatial width. Inset: illustration of the tuning curve correlations for multiple pairs of neurons with the same distance. (E) The difference of preferred orientation angles of neuron pairs as a function of their horizontal cortical distance (black) and the exponential fitted curve (red). λ: the same as in (D). Inset: illustration of difference of preferred orientation angles for multiple neuron pairs with the same horizontal cortical distance. (F) L4 OS neurons that belong to any micro-clusters (distance $<$ 15 μm and preferred orientation difference $< 30°$) are interconnected with black lines and colored-coded by their preferred orientations. Gray dots are neurons that don't belong to any micro-clusters. Neurons from different imaging planes and different mice were vertically stacked. The number above the figure indicates the proportion of neurons within any micro-clusters. (G) The ratios of actual counts of L4 micro-clusters (numbers above the bars) of different sizes (2: pair; 3: triplet) to that of randomly shuffled data.

distance. As α increases, however, the spatial scale of both the clustering on the OS map and the correlation diminished with many neurons changing their preferred orientation angles. At alpha equals to 1, the tuning curve correlation decays to zero over hundreds of microns. Further increasing α (e.g. $\alpha = 1.25$) produces non-zero tuning curve correlation over large scales as smaller α values. Similar trend was observed in L4 datasets as well.

Given how the tuning properties of V1 neurons appear to depend on neuropil coefficients, we must be careful to find an optimal value of α to characterize the spatial scale of tuning clustering. Rather than rely on untested neuropil subtraction methods, we collected ground-truth data where neuropil contamination does not exist by expressing nuclear-targeted GCaMP6s. Unlike cytosolic GCaMP which transduces indicator expression in both cell bodies and neuronal processes, nuclear-targeted GCaMP confines the fluorescence signals to the cell nucleus only. Therefore, with absence of neuropil signals in the nuclear-targeted datasets, neuropil subtraction is unnecessary for measuring accurate calcium transients.

We labeled neurons in wildtype mouse V1 L2/3 with nuclear-targeted GCaMP6s, and performed the same experiments as described above (see Methods). To verify that nuclear-targeted GCaMP6s eliminates neuropil signal contamination, we applied the same neuropil subtraction methods with varied neuropil coefficient α. As expected, subtracting the minimal neuropil signal with coefficients from 0 to 1 does not change the tuning properties of the neurons (Fig. 4.3I), nor does it change the tuning curve correlation (Fig. 4.3J). Examining only neuron pairs with horizontal distances $< 50\ \mu m$, the tuning curve correlation decays with increasing cortical distance and converges to 0 (Fig. 4.3K, orange curve). This "decay-to-zero" property provides us a guidance on how to choose the neuropil factor. Looking back at our cytosolic GCaMP6s L2/3 data, the coefficient $\alpha = 1$ was chosen to make the correlation curve decay to zero (Fig. 4.3K, blue curve). This value optimally removes the neuropil fluorescence and recovers the true neuronal activity, as evidenced by the tuning curve correlation matching that of the nuclear-targeted dataset. We applied the same method on the cytosolic L4 data and obtained an estimated neuropil coefficient $\alpha = 1$ as well. Notably, the optimal value may differ from 1 for other datasets with different imaging conditions. For example, axially elongated excitation focus due to optical aberrations or the system of low NA may lead to more severe neuropil contamination and thus larger optimal coefficients [93, 124].

4.3 Preliminary data: Two-color imaging of thalamic axons and V1 L2/3 neurons

In this section, we demonstrated our ability to functionally image dLGN boutons and L2/3 neurons simultaneously by 2PFM two-color imaging (Fig. 4.4). This technique will be used in the future to correlate the neuronal activity of V1 neurons and their thalamocortical afferent inputs and examine the related V1 models.

To label dLGN and V1 neurons separately, 30 nL of AAV9-syn-NES-jRGECO1a ($\sim$

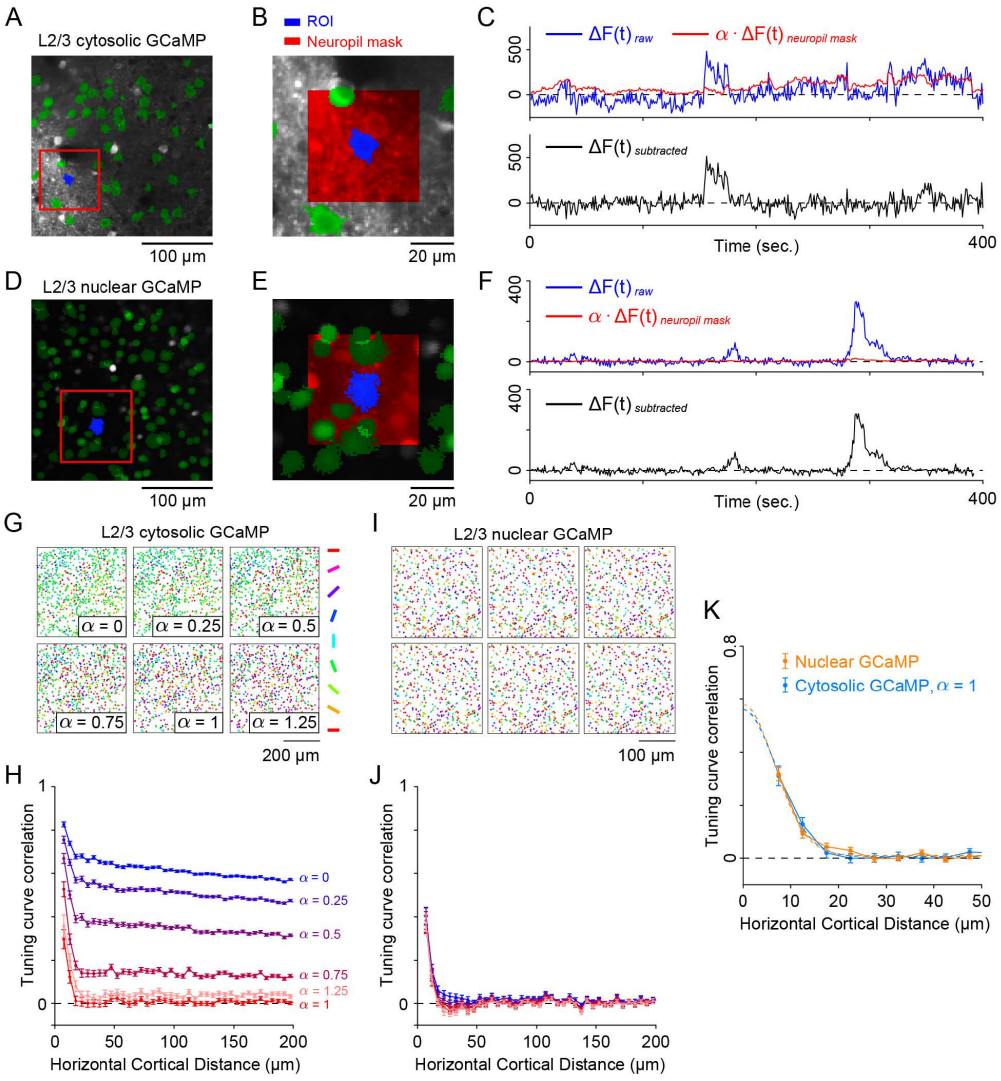

Figure 4.3: The effect of neuropil subtraction on micro-clustered organization. (A-C, G-H) Cytosolic GCaMP6s L2/3 data. (D-F, I-J) Nuclear-targeted GCaMP6s L2/3 data. (A, D) An example of a fluorescence imaging plane of V1 L2/3. (B, E) Zoom-in view of the red box in panel A and D respectively. For every neuron (blue), a neuropil mask (red) was defined as a square region from the center of the neuron excluding any other neurons (green) in the square. (C, F) Top: $\Delta F(t)$ traces of the raw fluorescence signal (blue) and the neuropil signal (red, with $\alpha = 1$). Bottom: calcium transients after neuropil subtraction: $\Delta F(t)_{subtracted} = \Delta F(t)_{raw} - \alpha \cdot \Delta F(t)_{neuropil}$. (G, I) OS maps with neurons color-coded by their preferred orientations for different neuropil coefficients α from 0 to 1 at 0.25 increments. Neurons from different imaging planes and different mice were stacked. (H, J) Tuning curve correlation of neuron pairs as a function of cortical distance for different neuropil coefficients α. (K) Zoom-in view of the curve in H and J (with $\alpha = 1$) for cytosolic data (blue) and nuclear data (orange), respectively, within 50 μm distance.

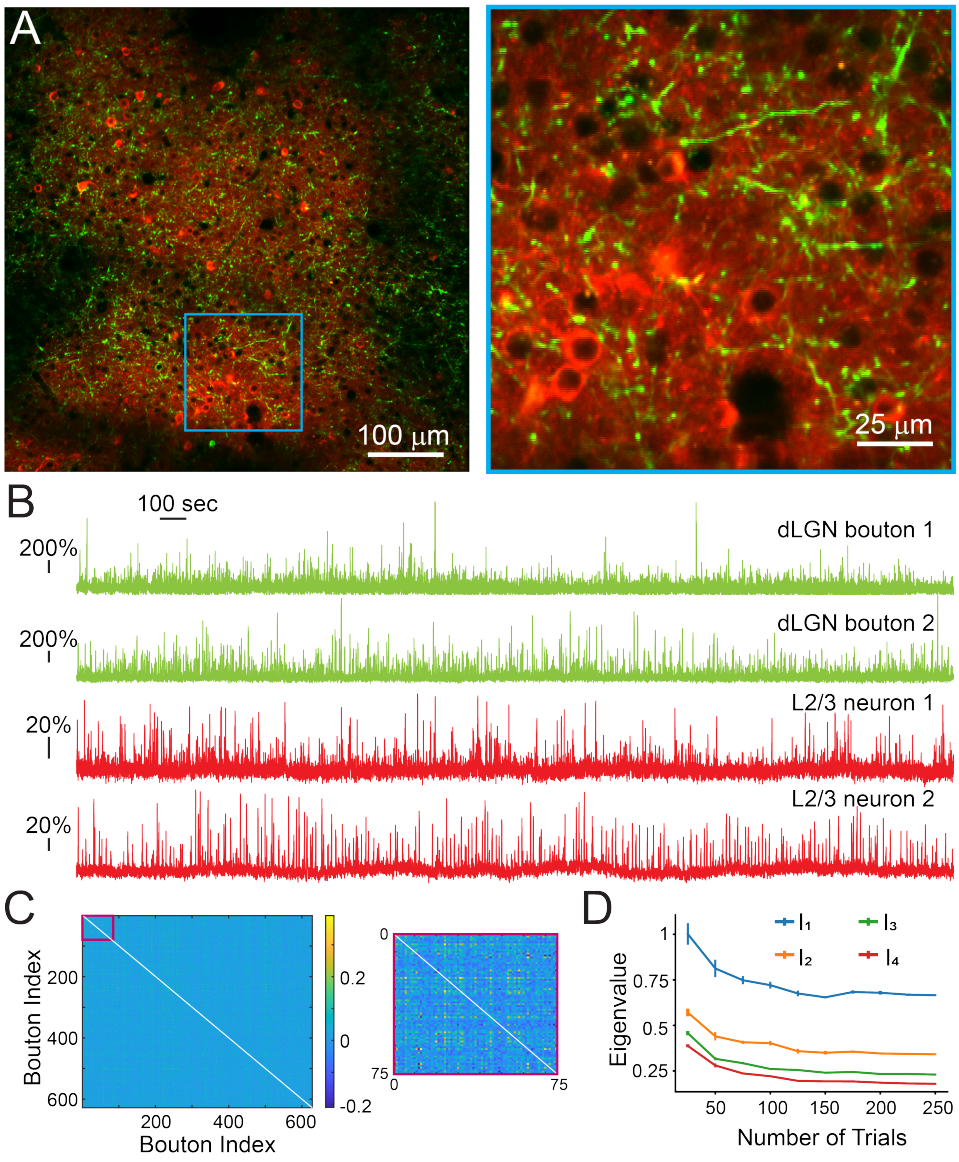

Figure 4.4: Preliminary data of two-color *In vivo* imaging. (A) Simultaneous imaging of GCaMP6s thalamic axons (green) and jRGECO V1 L2/3 neurons (red). Right: zoomed-in view of the region in the blue box. (B) Calcium transients of 4 randomly selected dLGN boutons and L2/3 neurons in response to drifting gratings at 4 angles (horizontal, vertical and 2 diagonals). (C) Covariance matrix for trial-to-trial dLGN bouton activity. Correlation coefficients are indicated by the color. Right: zoomed-in view of the region in the red box. (D) Top 4 eigenvalues of the matrix in (B) as a function of the number of repeats/trials for each visual stimulus.

1.8×10^{13} infectious units per ml) were injected into V1 of wildtype mice to label L2/3 neurons at each injection site (left hemisphere, -0.2 to 1.0 mm to Lambda; 2.2 to 2.8 mm lateral from midline; 0.3 mm below pia; 9 injection sites with $\sim$300 μm apart), and 30 nl of AAV2/1-syn-GAP43-GCaMP6s ($\sim 1.2 \times 10^{13}$ infectious units per ml) were injected into dLGN (left hemisphere, 2.3 mm anterior to Lambda; 2.3mm lateral from midline; 2.35, 2.55, 2.75 mm below pia).

We excited both fluorophores with 920nm light, and the emission light was spectrally separated with a dichroic mirror, filtered by bandpass filters (525/50 nm for GCaMP6s and 609/70 nm for jRGECO) and detected by two different PMTs. Mice were presented with sinusoidal gratings drifting in 4 directions (horizontal, vertical and two diagonals). Each direction was repeated 250 times in a pseudorandom sequence (Other experimental settings are the same as described in Methods: visual stimulation). Images of thalamic axons and V1 L2/3 neurons (Fig. 4.4A) were acquired at 100 μm to 300 μm below dura with pixel size of 0.3 μm and frame rate of 7.6 Hz. Calcium transients for boutons and neurons were extracted (Fig. 4.4B) from the image sequence. The covariance matrix for trial-to-trial dLGN bouton activity was plotted (Fig. 4.4C). Further analysis on the eigenvalues of the matrix (Fig. 4.4D) demonstrates that a large number of repeats/trials (>150) is necessary for discovering the underlying patterns from the extensive activity data.

The ability of two-color imaging with 2PFM enables us to functionally image V1 neurons and thalamic axon projections simultaneously. Future work includes the examination of whether the observed neuronal activity properties in V1, e.g. spatial clustering of tuning and noise correlations, are inherited from the feedforward inputs or emerge from the recurrent circuit itself. More experiments will be conducted to validate V1 circuit models.

4.4 Methods

Mice

All animal procedures and protocols were approved by the Institutional Animal Care and Use Committee at the University of California, Berkeley (AUP-2020-06-13343). Wild-type mice (C57BL/6J) and Scnn1a-Tg3-Cre mice older than 2 months were used for in vivo functional imaging of L2/3 and L4 neurons in V1, respectively. Male and female mice were equally represented, and no sex differences were observed.

Virus injection and cranial window implant

Craniotomy and virus injection were performed on adult mice following established procedures [88]. Buprenorphine (0.33 μL/g) was administered subcutaneously at the start of the surgery. Mice were anesthetized with 1%-2% isoflurane in oxygen throughout the surgery. A 3-mm craniotomy was made over the primary visual cortex (V1) for optical access. The dura was left intact. Virus injection was performed using a glass pipetted beveled at 45° with a 15-20 μm opening and backfilled with mineral oil. Viral solution was loaded and injected into

the cortex 300-350 μm below dura with a hydraulic manipulator (MO10; Narishige). 30 nL of AAV2/1-syn-GCaMP6s ($\sim 3 \times 10^{13}$ GC/mL) or AAV2/1-Syn-H2B-GCaMP6s ($\sim 5 \times 10^{12}$ GC/mL) solution were injected into wild-type mice to express GCaMP6s in the cytosol or the nucleus, respectively. 30 nL of AAV2/1-syn-FLEX-GCaMP6s ($\sim 1 \times 10^{13}$ GC/mL) solution was injected into V1 of Scnn-Tg3-Cre mice to express GCaMP6s cytosolically in L4 excitatory neurons in V1. A cranial window made of a No.1.5 coverslip was placed over the craniotomy and glued in place with Vetbond (Vetbond; 3M). A titanium headbar was attached to the skull with cyanoacrylate glue and dental acrylic. Meloxicam was given (1 μL/g) subcutaneously after the surgery.

In vivo two-photon imaging

In vivo two-photon imaging was performed 2-4 weeks after the surgery. All imaging recordings were carried out on awake mice that were habituated for head fixation and body constraint. Two-photon calcium imaging was conducted using a Thorlabs Bergamo® II multiphoton microscope. Hardware control and data acquisition were performed using the ThorImage software. Fluorescence from GCaMP6s was excited by a titanium–sapphire laser (Chameleon Ultra II, Coherent Inc.) at 920 nm. The laser beam was focused by a Nikon 16×, 0.8 NA water-dipping objective. The emitted two-photon fluorescence was collected by the same objective, spectrally filtered by a bandpass filter (525/50 nm) and detected by a photomultiplier tube (PMT). The post-objective power was varied between 20 and 80 mW, depending on the imaging depth. Typical images had 1024 × 1024 pixels at 0.7-1 μm/pixel and a frame rate of 7.6 Hz. Data of L2/3 neurons were acquired from 34 imaging planes of 10 mice at imaging depths between 110 and 290 μm below dura. Data of L4 neurons were acquired from 44 imaging planes of 5 mice at imaging depths between 220 and 460 μm below dura.

Visual stimulation

Visual stimuli were generated by custom-written MATLAB® codes using Psychtoolbox [152] and displayed on a screen (Samsung Galaxy Tablet). To measure the orientation tuning properties of neurons, circular sinusoidal gratings drifting in 12 directions (at 30° increments) were presented on a screen 8 cm away from the right eye of the mouse, covering 70° × 70° of visual space. Each grating stimulus was repeated 10 times in a pseudorandom sequence. The gratings was displayed in the blue channel of the screen to stimulate the blue opsin of the mouse retina [153]. Each stimulus lasted for 10 seconds, with a uniform blue screen displayed for the first 3 and last 2 seconds and a drifting grating presented for the middle 5 seconds. The gratings had 100% contrast, a spatial frequency of 0.07 cycles per degree, and a temporal frequency of 2 cycles per second. The onset of each visual stimulus was marked by the appearance of a small patch of bright pixels that was detected by a photodetector (Thorlabs, PDA10A2) to trigger image acquisition.

Mouse behavioral monitoring and analysis

We performed two-photon imaging on awake mice with head fixed and body constrained. Studies show [154] that the rapid variations in behavioral state may affect both sensory-evoked and spontaneous neural activities. Therefore, we also tracked the animal's pupil size and facial movement for some experiments. We illuminated the animal's face and eye by infrared LEDs and recorded the behaviors by a camera (Mako U-130B) with an infrared filter. We synchronize the behavioral monitoring and the two-photon image acquisition by using the same photodetector trigger and forcing them to have the same frame rate.

Custom-written MATLAB® codes were used to analyze mouse pupil changes and facial movements. The pupil of each frame was outlined based on the algorithm of Circular Hough Transform. This approach is not very robust in the presence of cornea reflection and whisker arousal, we thus developed a GUI to allow users manually correct the misdrawn pupils. The video of facial movements was decomposed by principal component analysis (PCA) with the first 500 principal components extracted. These behavioral analysis will be used for future investigation of behavioral-evoked neural activities.

Data analysis pipeline

Calcium imaging data was processed by custom-written MATLAB® codes. Time-lapse image sequences were registered with a rigid-motion correction algorithm [155]. Regions of interest (ROIs) representing individual cortical neurons were detected and outlined for each image sequence by Suite2p [77]. Overlapped ROIs were manually removed in Suite2p GUI before further processing. Raw fluorescence signal for each neuron, $F(t)_{raw}$, was extracted as the average value of the pixels within the ROI representing the neuron. To extract the neuropil signal, a square neuropil mask extending 30 μm from each neuron's center (i.e., the center of mass of all pixels within the ROI) was defined. The neuropil signal of each neuron, $F(t)_{neuropil}$, was the average value of pixels within the neuropil but outside the ROIs identified as neurons. Defining the baseline fluorescence of the neuropil, $F_{0,neuropil}$, as the mode of signal distribution of $F(t)_{neuropil}$, we then calculated the neuropil contamination signal as $\Delta F(t)_{neuropil} = F(t)_{neuropil} - F_{0,neuropil}$. We subtracted the neuropil contamination signal, weighted by a neuropil coefficient α, from the raw fluorescence signal of each neuron to acquire the neuronal calcium signal as $F(t) = F(t)_{raw} - \alpha \cdot \Delta F(t)_{neuropil}$. Defining the baseline fluorescence of the neuron, F_0, as the mode of signal distribution of $F(t)$, we calculated the calcium transient as $\Delta F(t)/F_0 = (F(t) - F_0)/F_0$. For simplification, α is uniform for all cells. For each ROI, the response to each stimulus direction was defined as the average $\Delta F/F_0$ during the time window of stimulus presentation across totally 10 trials. Thus, we defined the direction tuning curve $r(\theta)$ across totally 12 stimulus directions for each ROI. For ROIs considered to be responsive (maximum $\Delta F/F_0$ of tuning curve above 0.1), and with significantly different responses across stimuli directions (one-way ANOVA test, P <

0.05), we fit their direction tuning curves $r(\theta)$ with a bimodal Gaussian function:

$$r(\theta) = A_{pref.} \cdot \exp(-\frac{ang(\theta - \theta_{pref})^2}{2\sigma^2}) + A_{oppo.} \cdot \exp(-\frac{ang(\theta - \theta_{pref} + \pi)^2}{2\sigma^2}) + A_0$$

where $\theta_{pref.}$ is the preferred direction, $A_{pref.}$ and $A_{oppo.}$ are the responses at the preferred direction and the opposite preferred direction (i.e. $\theta_{pref.} - \pi$) respectively. The function $ang(\Delta\theta) = min(|\Delta\theta|, |\Delta\theta - 2\pi|, |\Delta\theta + 2\pi|)$ wraps periodic angular values onto the interval $[0, 2\pi]$. A_0 is the constant offset. σ is the width of each Gaussian peak. The preferred orientation is defined as $mod(\theta_{pref.}, \pi)$. To determine the goodness of fit, we calculated the residual sum of squares of fitting error E, as well as the coefficient of determination R2:

$$E = \sum_{\theta} (r_{measured}(\theta) - r_{fitted}(\theta))^2$$

$$R^2 = 1 - \frac{\sum_{\theta}(r_{measured}(\theta) - r_{fitted}(\theta))^2}{\frac{n-1}{n}\sum_{\theta}(r_{measured}(\theta) - \langle r_{measured}(\theta)\rangle)^2}$$

where $r_{measured}(\theta)$ and $r_{fitted}(\theta)$ are the experimental measured and fitted responses at direction θ respectively. $\langle\cdot\rangle$ is the mean response across θ. Only when $E < 0.4$ and $R^2 > 0.6$ the ROI was defined as well fit to the bimodal Gaussian function. And only when ROIs with tuning curves that were 1) responsive; 2) significant anisotropic across the 12 direction; 3) well fit to the bimodal Gaussian function, we define those ROIs as orientation selective (OS).

To quantify neuronal tuning we defined orientation selectivity index (OSI) for OS ROIs:

$$OSI = \frac{|\sum_k r(\theta_k)\exp(2i\theta_k)|}{\sum_k r(\theta_k)}$$

where k is the index among 12 directions, and $r(\theta)$ is the tuning curve. $OSI = 0$ means no selectivity, and $OSI = 1$ means perfect selectivity.

To calculate the distance dependent functions of tuning curve correlations, we compute the cortical distance (defined as the distance between the center of mass of their cell bodies), and the correlation coefficient (i.e. normalized dot product) of tuning curves for all pairs of OS neurons. We then defined distance bins start from 5 μm with interval of 5 μm, i.e. 5 - 10 μm, 10 - 15 μm, etc.), and calculated the mean value and standard error of correlation values within all these bins for the error bar plots. Similar methods were used for the distance dependent functions of the difference between preferred orientation angles ($\Delta\theta$).

Neuropil subtraction

The ground-truth data collected by expressing nuclear-targeted GCaMP6s in V1 L2/3 provided us a guidance on how to choose the neuropil factor: the tuning curve correlation should decay to zero over tens of microns; or the difference of preferred orientation angles of neuron pairs should converges to 45°. With this requirement, we tested multiple neuropil subtraction methods used in past studies on one example L2/3 dataset (Fig. 4.5). Disappointingly,

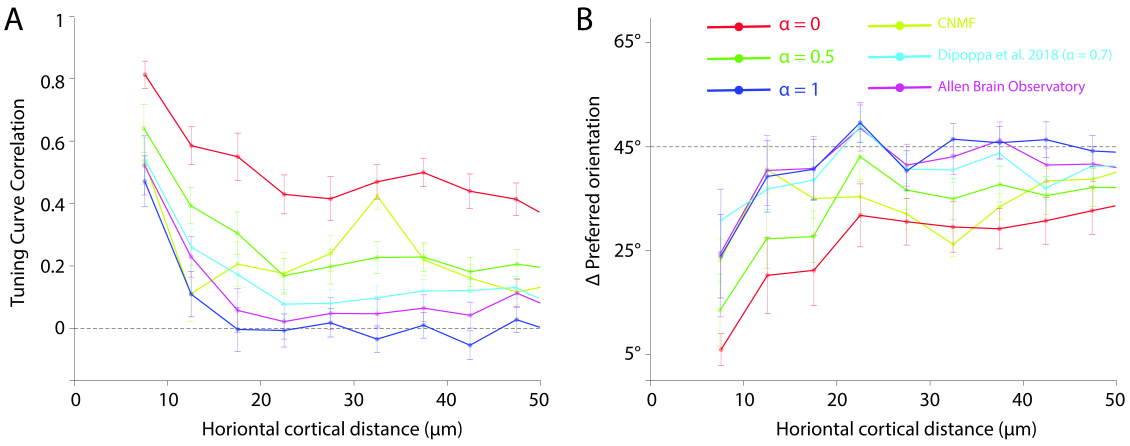

Figure 4.5: Comparison of different neuropil subtraction methods. (A) Tuning curve correlation of neuron pairs as a function of their horizontal cortical distance for different neuropil subtraction methods. (B) The difference of preferred orientation angles of neuron pairs as a function of their horizontal cortical distance for different neuropil subtraction methods.

for this dataset none of those methods produce reliable results that match the ground-truth data except when the coefficient α was set to 1.

We compared the following neuropil subtraction methods as well as setting the value ($\alpha = 0, 0.5, 1$):

1. **Constrained Nonnegative Matrix Factorization (CNMF)**: CNMF [151, 156, 157] detects neurons by factorizing the data matrix Y (the original 3D stack is first transformed into a 2D matrix) to three matrices, A (spatial footprints), C (temporal dynamics) and B (background): $Y = AC + B$, with constraints of (1) spatial locality and sparsity on A and (2) non-negative and sparsity on C. B models the time-varied background signals which are contributed by out-of-focus fluorescence and neuropil activities. The global fluctuation of the background is captured by enforcing B to be a low-rank non-negative matrix. By matrix decomposition of the image sequence, the calcium transients sans neuropil contamination are extracted into C.

2. **Method of Dipoppa et al. 2018 [78]**: the neuropil signal is extracted by a defined neuropil mask as described above. For each neuron, this method plots the scatter plot of the time-varying raw signal F_{raw} vs. neuropil signal $F_{neuropil}$ (1 point every timestamp). The lower 5% percentile of the scatter plot are linearly fitted to get α_i. The neuropil coefficient α is computed as the average of α_i over all neurons: $\alpha = \langle \alpha_i \rangle$. For the example dataset used in Fig. 4.5, $\alpha = 0.7$.

3. **Method of Allen Brain Observatory [150]**: The measured raw fluorescence is modeled as the summation of ROI and neuropil fluorescence signals: $F_{raw} = F_{cell} + \alpha \cdot F_{neuropil}$. For a given ROI with known F_{raw} and $F_{neuropil}$ (extracted by a defined

neuropil mask as described above), this algorithm first computes F_{cell} with a fixed value of α, for a range of α values by minimizing $\sum_t |F_{cell} + \alpha \cdot F_{neuropil} - F_{raw}|^2 + \lambda |L F_{cell}|^2$, where λ is set to 0.05 and L is the discrete first derivative (to enforce smoothness of F_{cell}). With all of the (α, F_{cell}) pairs, it selected the one that minimizes the error $\sum_t |F_{cell} + \alpha \cdot F_{neuropil} - F_{raw}|^2$. The estimated neuropil coefficient α varies from cell to cell. For the example dataset used in Fig. 4.5, the coefficient was distributed broadly between 0 to 2 with an average 0.83.

Chapter 5

Conclusion

Although 2PFM has many advantages over conventional fluorescence microscopy, the imaging performance is still limited by optical aberrations induced by the sample and imaging system, which prevents high-resolution imaging of fine structures in thick samples. The Ji lab has developed AO methods by which the aberrations can be measured *in vivo* and corrected by shaping the wavefront of the excitation light. The dissertation discusses our recent progress on applying adaptive optical two-photon fluorescence microscopy to high-precision *in vivo* imaging of the mouse visual pathway.

Chapter 2 presents how indirect-wavefront-sensing-based AO is applied to divergence-based remote focusing. Remote focusing is a collection of techniques to scan the focal spot without moving the microscope objective or the sample. One popular implementation of remote focusing is by controlling the divergence of excitation light. Such divergence-based approach, however, achieves fast volumetric imaging in microscopy at the expense of image quality, because it introduces optical aberrations to the imaging process. Here, we systematically characterized the image distortion and optical aberration induced by divergence-based remote focusing over large focal shift ranges with microscope objectives of different NAs. We demonstrated that indirect-wavefront-sensing-based AO can fully correct the divergence-induced aberrations. Despite substantially increasing the signal and resolution of 2PFM images, the fluorescence signal was not fully recovered to the level observed in the natural focal plane. This is due to decreasing SLM efficiency with increasing defocus, leading to smaller fraction of energy being delivered to focus farther away from the natural focal plane. Together, our findings indicates both how remote focusing with divergence control can achieve its optimal performance and the limitation of such performance with a liquid-crystal-SLM-based axial scanning system.

Chapter 3 presents a method for *in vivo* mouse retinal imaging with direct-wavefront-sensing-based AO-2PFM. To achieve the best image quality and the largest FOV size, we used mouse eye itself as the focusing element of 2PFM. Furthermore, AO is used to correct ocular aberrations and achieve high-resolution vasculature and cellular imaging of the retina. We found that the ocular aberration is location-dependent but larger wavefront sensing area can improve for global AO performance. We applied our AO-2PFM to *in vivo* retinal phys-

iological and pharmacological studies. We studied retinal capillary lesions in a pathological mouse model with over-grown blood vessels. We also investigated the RGC hyperactivity in a mouse model of retinal degeneracy. Our work represents an important advancement in enabling high-resolution longitudinal studies of retinal pathology and pharmacology for disease diagnosis and treatment.

Chapter 4 discusses the applications of 2PFM on mouse neuronal activity imaging. 2PFM provides superior spatial resolution with cell-type specificity and the ability to monitor the neural circuitry dynamics. We utilized 2PFM to characterize the neuronal activities of neurons and the thalamocortical afferents in V1 to support and validate theoretical neural models. We investigated the spatial organization of orientation tuning in mouse V1, which has long been debated in the literature. We measured the tuning properties of neurons in V1 L2/3 and L4 in response to visual stimuli. We found that they form micro-clusters of neurons with similar orientation preference. Given that the spatial scale of the clustering depends sensitively on the neuropil subtraction method, we collected ground-truth data where neuropil contamination is eliminated by only expressing GCaMP6s in the nuclei. We also presented preliminary data of functionally imaging dLGN boutons and L2/3 neurons simultaneously. These data will be used to investigate whether the observed activity patterns in V1 are inherited from the thalamic inputs or are emergent properties of the V1 circuit itself.

In conclusion, the thesis described how advanced 2PFM techniques involving AO and remote focusing can be used for high-precision measurement of neuronal structure and function in the mouse visual pathway. We expect that these studies will impact both future experimental and theoretical investigations of visual pathway with advanced 2PFM technologies.

Bibliography

[1] Winifried Denk, James H Strickler, and Watt W Webb. "Two-photon laser scanning fluorescence microscopy". In: *Science* 248.4951 (1990), pp. 73–76.

[2] Marvin Minsky. "Memoir on inventing the confocal scanning microscope". In: (1996).

[3] José-Angel Conchello and Jeff W Lichtman. "Optical sectioning microscopy". In: *Nature methods* 2.12 (2005), pp. 920–931.

[4] Mark AA Neil, Rimas Juškaitis, and Tony Wilson. "Method of obtaining optical sectioning by using structured light in a conventional microscope". In: *Optics letters* 22.24 (1997), pp. 1905–1907.

[5] Daryl Lim, Kengyeh K Chu, and Jerome Mertz. "Wide-field fluorescence sectioning with hybrid speckle and uniform-illumination microscopy". In: *Optics letters* 33.16 (2008), pp. 1819–1821.

[6] Dal Hyung Kim et al. "Pan-neuronal calcium imaging with cellular resolution in freely swimming zebrafish". In: *Nature methods* 14.11 (2017), pp. 1107–1114.

[7] Karel Svoboda et al. "In vivo dendritic calcium dynamics in neocortical pyramidal neurons". In: *Nature* 385.6612 (1997), pp. 161–165.

[8] Christoph Stosiek et al. "In vivo two-photon calcium imaging of neuronal networks". In: *Proceedings of the National Academy of Sciences* 100.12 (2003), pp. 7319–7324.

[9] Fritjof Helmchen and Winfried Denk. "Deep tissue two-photon microscopy". In: *Nature methods* 2.12 (2005), pp. 932–940.

[10] Horace W Babcock. "The possibility of compensating astronomical seeing". In: *Publications of the Astronomical Society of the Pacific* 65.386 (1953), pp. 229–236.

[11] Horace W Babcock. "Adaptive optics revisited". In: *Science* 249.4966 (1990), pp. 253–257.

[12] Robert K Tyson and Benjamin West Frazier. *Principles of adaptive optics*. CRC press, 2022.

[13] Na Ji. "Adaptive optical fluorescence microscopy". In: *Nature methods* 14.4 (2017), pp. 374–380.

[14] Martin J Booth. "Adaptive optical microscopy: the ongoing quest for a perfect image". In: *Light: Science & Applications* 3.4 (2014), e165–e165.

[15] Karen M Hampson et al. "Adaptive optics for high-resolution imaging". In: *Nature Reviews Methods Primers* 1.1 (2021), pp. 1–26.

[16] Na Ji, Jeremy Freeman, and Spencer L Smith. "Technologies for imaging neural activity in large volumes". In: *Nature neuroscience* 19.9 (2016), pp. 1154–1164.

[17] Kai Wang et al. "Rapid adaptive optical recovery of optimal resolution over large volumes". In: *nature methods* 11.6 (2014), pp. 625–628.

[18] Kai Wang et al. "Direct wavefront sensing for high-resolution in vivo imaging in scattering tissue". In: *Nature communications* 6.1 (2015), pp. 1–6.

[19] Rui Liu et al. "Direct wavefront sensing enables functional imaging of infragranular axons and spines". In: *Nature methods* 16.7 (2019), pp. 615–618.

[20] Zhongya Qin et al. "Adaptive optics two-photon microscopy enables near-diffraction-limited and functional retinal imaging in vivo". In: *Light: Science & Applications* 9.1 (2020), pp. 1–11.

[21] Congping Chen et al. "High-resolution two-photon transcranial imaging of brain using direct wavefront sensing". In: *Photonics Research* 9.6 (2021), pp. 1144–1156.

[22] Ben Platt and RV Shack. "Production and use of a lenticular Hartmann screen". In: *J. Opt. Soc. A* 61 (1971).

[23] Ben C Platt and Roland Shack. *History and principles of Shack-Hartmann wavefront sensing*. 2001.

[24] Na Ji, Daniel E Milkie, and Eric Betzig. "Adaptive optics via pupil segmentation for high-resolution imaging in biological tissues". In: *Nature methods* 7.2 (2010), pp. 141–147.

[25] Daniel E Milkie, Eric Betzig, and Na Ji. "Pupil-segmentation-based adaptive optical microscopy with full-pupil illumination". In: *Optics letters* 36.21 (2011), pp. 4206–4208.

[26] Cristina Rodríguez et al. "An adaptive optics module for deep tissue multiphoton imaging in vivo". In: *Nature methods* 18.10 (2021), pp. 1259–1264.

[27] Martin J Booth et al. "Adaptive aberration correction in a confocal microscope". In: *Proceedings of the National Academy of Sciences* 99.9 (2002), pp. 5788–5792.

[28] Delphine Débarre et al. "Image-based adaptive optics for two-photon microscopy". In: *Optics letters* 34.16 (2009), pp. 2495–2497.

[29] Delphine Débarre, Martin J Booth, and Tony Wilson. "Image based adaptive optics through optimisation of low spatial frequencies". In: *Optics Express* 15.13 (2007), pp. 8176–8190.

[30] James R Fienup. "Reconstruction of an object from the modulus of its Fourier transform". In: *Optics letters* 3.1 (1978), pp. 27–29.

[31] Reinier Doelman, Nguyen H Thao, and Michel Verhaegen. "Solving large-scale general phase retrieval problems via a sequence of convex relaxations". In: *JOSA A* 35.8 (2018), pp. 1410–1419.

[32] Benjamin P Cumming and Min Gu. "Direct determination of aberration functions in microscopy by an artificial neural network". In: *Optics Express* 28.10 (2020), pp. 14511–14521.

[33] PA Khorin et al. "Neural networks application to determine the types and magnitude of aberrations from the pattern of the point spread function out of the focal plane". In: *Journal of Physics: Conference Series*. Vol. 2086. 1. IOP Publishing. 2021, p. 012148.

[34] Ivan Vishniakou and Johannes D Seelig. "Wavefront correction for adaptive optics with reflected light and deep neural networks". In: *Optics Express* 28.10 (2020), pp. 15459–15471.

[35] Ziwei Li et al. "Fast widefield imaging of neuronal structure and function with optical sectioning in vivo". In: *Science advances* 6.19 (2020), eaaz3870.

[36] Marco Dal Maschio et al. "Three-dimensional in vivo scanning microscopy with inertia-free focus control". In: *Optics letters* 36.17 (2011), pp. 3503–3505.

[37] Benjamin F Grewe et al. "Fast two-layer two-photon imaging of neuronal cell populations using an electrically tunable lens". In: *Biomedical optics express* 2.7 (2011), pp. 2035–2046.

[38] Gaddum Duemani Reddy et al. "Three-dimensional random access multiphoton microscopy for functional imaging of neuronal activity". In: *Nature neuroscience* 11.6 (2008), pp. 713–720.

[39] Paul A Kirkby, KM Naga Srinivas Nadella, and R Angus Silver. "A compact acousto-optic lens for 2D and 3D femtosecond based 2-photon microscopy". In: *Optics express* 18.13 (2010), pp. 13720–13744.

[40] Edward J Botcherby et al. "Aberration-free optical refocusing in high numerical aperture microscopy". In: *Optics letters* 32.14 (2007).

[41] Edward J Botcherby et al. "An optical technique for remote focusing in microscopy". In: *Optics Communications* 281.4 (2008), pp. 880–887.

[42] Edward J Botcherby et al. "Aberration-free three-dimensional multiphoton imaging of neuronal activity at kHz rates". In: *Proceedings of the National Academy of Sciences* 109.8 (2012), pp. 2919–2924.

[43] Rui Liu et al. "Aberration-free multi-plane imaging of neural activity from the mammalian brain using a fast-switching liquid crystal spatial light modulator". In: *Biomedical Optics Express* 10.10 (2019), pp. 5059–5080.

[44] Yuhan Yang et al. "Adaptive optics enables aberration-free single-objective remote focusing for two-photon fluorescence microscopy". In: *Biomedical Optics Express* 12.1 (2021), pp. 354–366.

[45] Jaime Grutzendler and Wen-Biao Gan. "Two-photon imaging of synaptic plasticity and pathology in the living mouse brain". In: *NeuroRx* 3.4 (2006), pp. 489–496.

[46] Anthony Holtmaat and Karel Svoboda. "Experience-dependent structural synaptic plasticity in the mammalian brain". In: *Nature Reviews Neuroscience* 10.9 (2009), pp. 647–658.

[47] Xinzhu Yu and Yi Zuo. "Spine plasticity in the motor cortex". In: *Current opinion in neurobiology* 21.1 (2011), pp. 169–174.

[48] Dimitrios Davalos et al. "Stable in vivo imaging of densely populated glia, axons and blood vessels in the mouse spinal cord using two-photon microscopy". In: *Journal of neuroscience methods* 169.1 (2008), pp. 1–7.

[49] Ricardo Mostany and Carlos Portera-Cailliau. "A method for 2-photon imaging of blood flow in the neocortex through a cranial window". In: *J Vis Exp* 12 (2008).

[50] David Kleinfeld et al. "Fluctuations and stimulus-induced changes in blood flow observed in individual capillaries in layers 2 through 4 of rat neocortex". In: *Proceedings of the National Academy of Sciences* 95.26 (1998), pp. 15741–15746.

[51] Axel Nimmerjahn, Frank Kirchhoff, and Fritjof Helmchen. "Resting microglial cells are highly dynamic surveillants of brain parenchyma in vivo". In: *Science* 308.5726 (2005), pp. 1314–1318.

[52] Patrick J Drew et al. "Chronic optical access through a polished and reinforced thinned skull". In: *Nature methods* 7.12 (2010), pp. 981–984.

[53] Ricardo Augusto de Melo Reis, Hércules Rezende Freitas, and Fernando Garcia De Mello. "Cell calcium imaging as a reliable method to study neuron–glial circuits". In: *Frontiers in Neuroscience* 14 (2020), p. 569361.

[54] Thomas Hendel et al. "Fluorescence changes of genetic calcium indicators and OGB-1 correlated with neural activity and calcium in vivo and in vitro". In: *Journal of Neuroscience* 28.29 (2008), pp. 7399–7411.

[55] Rex Kerr et al. "Optical imaging of calcium transients in neurons and pharyngeal muscle of C. elegans". In: *Neuron* 26.3 (2000), pp. 583–594.

[56] Christine Grienberger and Arthur Konnerth. "Imaging calcium in neurons". In: *Neuron* 73.5 (2012), pp. 862–885.

[57] Eric R Kandel et al. *Principles of neural science*. Vol. 4. McGraw-hill New York, 2000.

[58] Senthil Selvam, Tejas Kumar, and Marcus Fruttiger. "Retinal vasculature development in health and disease". In: *Progress in retinal and eye research* 63 (2018), pp. 1–19.

[59] Charles P Wilkinson et al. *Ryan's Retina*. Elsevier Health Sciences, 2017.

[60] Carol Yim-lui Cheung et al. "Imaging retina to study dementia and stroke". In: *Progress in retinal and eye research* 57 (2017), pp. 89–107.

[61] Anat London, Inbal Benhar, and Michal Schwartz. "The retina as a window to the brain—from eye research to CNS disorders". In: *Nature Reviews Neurology* 9.1 (2013), pp. 44–53.

[62] Judith Lechner, Olivia E O'Leary, and Alan W Stitt. "The pathology associated with diabetic retinopathy". In: *Vision research* 139 (2017), pp. 7–14.

[63] Elena Ivanova et al. "Retina-specific targeting of pericytes reveals structural diversity and enables control of capillary blood flow". In: *Journal of Comparative Neurology* 529.6 (2021), pp. 1121–1134.

[64] Andrew Jo et al. "Intersectional strategies for targeting amacrine and ganglion cell types in the mouse retina". In: *Frontiers in neural circuits* 12 (2018), p. 66.

[65] Emily M Martersteck et al. "Diverse central projection patterns of retinal ganglion cells". In: *Cell reports* 18.8 (2017), pp. 2058–2072.

[66] Elisa Eme-Scolan and Samantha J Dando. "Tools and approaches for studying microglia in vivo". In: *Frontiers in Immunology* 11 (2020), p. 583647.

[67] Thomas Euler, Peter B Detwiler, and Winfried Denk. "Directionally selective calcium signals in dendrites of starburst amacrine cells". In: *Nature* 418.6900 (2002), pp. 845–852.

[68] Tom Baden et al. "The functional diversity of retinal ganglion cells in the mouse". In: *Nature* 529.7586 (2016), pp. 345–350.

[69] Elena García de la Cera et al. "Optical aberrations in the mouse eye". In: *Vision research* 46.16 (2006), pp. 2546–2553.

[70] Mark Bear, Barry Connors, and Michael A Paradiso. *Neuroscience: Exploring the Brain, Enhanced Edition: Exploring the Brain*. Jones & Bartlett Learning, 2020. Chap. 9, 10.

[71] Benjamin Scholl et al. "Emergence of orientation selectivity in the mammalian visual pathway". In: *Journal of Neuroscience* 33.26 (2013), pp. 10616–10624.

[72] David H Hubel and Torsten N Wiesel. "Receptive fields, binocular interaction and functional architecture in the cat's visual cortex". In: *The Journal of physiology* 160.1 (1962), p. 106.

[73] Kenichi Ohki et al. "Functional imaging with cellular resolution reveals precise micro-architecture in visual cortex". In: *Nature* 433.7026 (2005), pp. 597–603.

[74] Werner Gobel and Fritjof Helmchen. "In vivo calcium imaging of neural network function". In: *Physiology* 22.6 (2007), pp. 358–365.

[75] Dario L Ringach et al. "Spatial clustering of tuning in mouse primary visual cortex". In: *Nature communications* 7.1 (2016), pp. 1–9.

[76] Satoru Kondo and Kenichi Ohki. "Laminar differences in the orientation selectivity of geniculate afferents in mouse primary visual cortex". In: *Nature Neuroscience* 19.2 (2016), pp. 316–319.

[77] Marius Pachitariu et al. "Suite2p: beyond 10,000 neurons with standard two-photon microscopy". In: *BioRxiv* (2017), p. 061507.

[78] Mario Dipoppa et al. "Vision and locomotion shape the interactions between neuron types in mouse visual cortex". In: *Neuron* 98.3 (2018), pp. 602–615.

[79] M Blum et al. "Compact optical design solutions using focus tunable lenses". In: *Optical Design and Engineering IV*. Vol. 8167. SPIE. 2011, pp. 274–282.

[80] Alexandre Mermillod-Blondin, Euan McLeod, and Craig B Arnold. "High-speed varifocal imaging with a tunable acoustic gradient index of refraction lens". In: *Optics letters* 33.18 (2008), pp. 2146–2148.

[81] Wafa Amir et al. "Simultaneous imaging of multiple focal planes using a two-photon scanning microscope". In: *Optics letters* 32.12 (2007), pp. 1731–1733.

[82] Gaddum D Reddy and Peter Saggau. "Fast three-dimensional laser scanning scheme using acousto-optic deflectors". In: *Journal of biomedical optics* 10.6 (2005), p. 064038.

[83] Ariel Kaplan, Nir Friedman, and Nir Davidson. "Acousto-optic lens with very fast focus scanning". In: *Optics letters* 26.14 (2001), pp. 1078–1080.

[84] Mantas Žurauskas et al. "Rapid adaptive remote focusing microscope for sensing of volumetric neural activity". In: *Biomedical optics express* 8.10 (2017), pp. 4369–4379.

[85] Bernard Richards and Emil Wolf. "Electromagnetic diffraction in optical systems, II. Structure of the image field in an aplanatic system". In: *Proceedings of the Royal Society of London. Series A. Mathematical and Physical Sciences* 253.1274 (1959), pp. 358–379.

[86] William J Shain et al. "Extended depth-of-field microscopy with a high-speed deformable mirror". In: *Optics letters* 42.5 (2017), pp. 995–998.

[87] Sophia I Panagopoulou and Daniel P Neal. *Zonal matrix iterative method for wavefront reconstruction from gradient measurements*. 2005.

[88] Wenzhi Sun et al. "Thalamus provides layer 4 of primary visual cortex with orientation- and direction-tuned inputs". In: *Nature neuroscience* 19.2 (2016), pp. 308–315.

[89] Rui Liu et al. "Direct phase measurement in zonal wavefront reconstruction using multidither coherent optical adaptive technique". In: *Optics express* 22.2 (2014), pp. 1619–1628.

[90] Simon Moser, Monika Ritsch-Marte, and Gregor Thalhammer. "Model-based compensation of pixel crosstalk in liquid crystal spatial light modulators". In: *Optics express* 27.18 (2019), pp. 25046–25063.

[91] Martin Persson, David Engström, and Mattias Goksör. "Reducing the effect of pixel crosstalk in phase only spatial light modulators". In: *Optics express* 20.20 (2012), pp. 22334–22343.

[92] Tsai-Wen Chen et al. "Ultrasensitive fluorescent proteins for imaging neuronal activity". In: *Nature* 499.7458 (2013), pp. 295–300.

[93] Na Ji, Takashi R Sato, and Eric Betzig. "Characterization and adaptive optical correction of aberrations during in vivo imaging in the mouse cortex". In: *Proceedings of the National Academy of Sciences* 109.1 (2012), pp. 22–27.

[94] Yuhan Yang. *AO pattern interpolation tools for remote focusing*. Version 1.0.0. Dec. 2020. URL: `https://github.com/yuhany1024/AO_interpolation`.

[95] Virendra N Mahajan and Guang-ming Dai. "Orthonormal polynomials in wavefront analysis: analytical solution". In: *JOSA A* 24.9 (2007), pp. 2994–3016.

[96] Miguel Arevallilo Herráez et al. "Fast two-dimensional phase-unwrapping algorithm based on sorting by reliability following a noncontinuous path". In: *Applied optics* 41.35 (2002), pp. 7437–7444.

[97] M. F. Kasim. *Fast 2D phase unwrapping implementation in MATLAB*. Version 1.0.0. Dec. 2017. URL: `https://github.com/mfkasim91/unwrap_phase/`.

[98] Cristina Rodríguez and Na Ji. "Adaptive optical microscopy for neurobiology". In: *Current opinion in neurobiology* 50 (2018), pp. 83–91.

[99] Junzhong Liang, David R Williams, and Donald T Miller. "Supernormal vision and high-resolution retinal imaging through adaptive optics". In: *JOSA A* 14.11 (1997), pp. 2884–2892.

[100] Engin Akyol et al. "Adaptive optics: principles and applications in ophthalmology". In: *Eye* 35.1 (2021), pp. 244–264.

[101] Grazyna Palczewska et al. "Noninvasive two-photon microscopy imaging of mouse retina and retinal pigment epithelium through the pupil of the eye". In: *Nature medicine* 20.7 (2014), pp. 785–789.

[102] David P Biss et al. "In vivo fluorescent imaging of the mouse retina using adaptive optics". In: *Optics letters* 32.6 (2007), pp. 659–661.

[103] Clemens Alt et al. "An adaptive-optics scanning laser ophthalmoscope for imaging murine retinal microstructure". In: *Ophthalmic Technologies XX*. Vol. 7550. SPIE. 2010, pp. 202–212.

[104] Ying Geng et al. "Adaptive optics retinal imaging in the living mouse eye". In: *Biomedical optics express* 3.4 (2012), pp. 715–734.

[105] Robin Sharma et al. "In vivo two-photon imaging of the mouse retina". In: *Biomedical optics express* 4.8 (2013), pp. 1285–1293.

[106] Daniel J Wahl et al. "Wavefront sensorless adaptive optics fluorescence biomicroscope for in vivo retinal imaging in mice". In: *Biomedical optics express* 7.1 (2016), pp. 1–12.

[107] Daniel J Wahl et al. "Adaptive optics in the mouse eye: wavefront sensing based vs. image-guided aberration correction". In: *Biomedical Optics Express* 10.9 (2019), pp. 4757–4774.

[108] Ireneusz Grulkowski et al. "Swept source optical coherence tomography and tunable lens technology for comprehensive imaging and biometry of the whole eye". In: *Optica* 5.1 (2018), pp. 52–59.

[109] Yifan Jian, Robert J Zawadzki, and Marinko V Sarunic. "Adaptive optics optical coherence tomography for in vivo mouse retinal imaging". In: *Journal of biomedical optics* 18.5 (2013), p. 056007.

[110] Ryan P McNabb et al. "Wide-field whole eye OCT system with demonstration of quantitative retinal curvature estimation". In: *Biomedical Optics Express* 10.1 (2019), pp. 338–355.

[111] Guoping Feng et al. "Imaging neuronal subsets in transgenic mice expressing multiple spectral variants of GFP". In: *Neuron* 28.1 (2000), pp. 41–51.

[112] Ying Geng et al. "Optical properties of the mouse eye". In: *Biomedical optics express* 2.4 (2011), pp. 717–738.

[113] Niall Patton et al. "Retinal vascular image analysis as a potential screening tool for cerebrovascular disease: a rationale based on homology between cerebral and retinal microvasculatures". In: *Journal of anatomy* 206.4 (2005), pp. 319–348.

[114] Shawn Frost et al. "Retinal vascular biomarkers for early detection and monitoring of Alzheimer's disease". In: *Translational psychiatry* 3.2 (2013), e233–e233.

[115] M Kamran Ikram et al. "Retinal vascular caliber as a biomarker for diabetes microvascular complications". In: *Diabetes care* 36.3 (2013), pp. 750–759.

[116] Gerald Liew et al. "Retinal vascular imaging: a new tool in microvascular disease research". In: *Circulation: Cardiovascular Imaging* 1.2 (2008), pp. 156–161.

[117] Adi Schejter Bar-Noam, Nairouz Farah, and Shy Shoham. "Correction-free remotely scanned two-photon in vivo mouse retinal imaging". In: *Light: Science & Applications* 5.1 (2016), e16007–e16007.

[118] Zelun Wang, Sean McCracken, and Philip R Williams. "Transpupillary Two-Photon In Vivo Imaging of the Mouse Retina". In: *JoVE (Journal of Visualized Experiments)* 168 (2021), e61970.

[119] MC Campbell and A Hughes. "An analytic, gradient index schematic lens and eye for the rat which predicts aberrations for finite pupils." In: *Vision Research* (1981).

[120] S Remtulla and PE Hallett. "A schematic eye for the mouse, and comparisons with the rat". In: *Vision research* 25.1 (1985), pp. 21–31.

[121] Chen Wang and Na Ji. "Pupil-segmentation-based adaptive optical correction of a high-numerical-aperture gradient refractive index lens for two-photon fluorescence endoscopy". In: *Optics letters* 37.11 (2012), pp. 2001–2003.

[122] Chen Wang and Na Ji. "Characterization and improvement of three-dimensional imaging performance of GRIN-lens-based two-photon fluorescence endomicroscopes with adaptive optics". In: *Optics Express* 21.22 (2013), pp. 27142–27154.

[123] Mrinalini Hoon et al. “Functional architecture of the retina: development and disease”. In: *Progress in retinal and eye research* 42 (2014), pp. 44–84.

[124] Chen Wang et al. “Multiplexed aberration measurement for deep tissue imaging in vivo”. In: *Nature methods* 11.10 (2014), pp. 1037–1040.

[125] Laurence S Lim et al. “Age-related macular degeneration”. In: *The Lancet* 379.9827 (2012), pp. 1728–1738.

[126] Lawrence A Yannuzzi et al. “Retinal angiomatous proliferation in age–related macular degeneration”. In: *Retina* 32 (2012), pp. 416–434.

[127] John R Heckenlively et al. “Mouse model of subretinal neovascularization with choroidal anastomosis”. In: *Retina* 23.4 (2003), pp. 518–522.

[128] Wenzheng Hu et al. “Expression of VLDLR in the retina and evolution of subretinal neovascularization in the knockout mouse model’s retinal angiomatous proliferation”. In: *Investigative ophthalmology & visual science* 49.1 (2008), pp. 407–415.

[129] Chao Li et al. “Biochemical alterations in the retinas of very low-density lipoprotein receptor knockout mice: an animal model of retinal angiomatous proliferation”. In: *Archives of ophthalmology* 125.6 (2007), pp. 795–803.

[130] Chun-hong Xia et al. “Deletion of LRP5 in VLDLR knockout mice inhibits retinal neovascularization”. In: *PLoS One* 8.9 (2013), e75186.

[131] B Chang et al. “Retinal degeneration mutants in the mouse”. In: *Vision research* 42.4 (2002), pp. 517–525.

[132] Chris Sekirnjak et al. “Changes in physiological properties of rat ganglion cells during retinal degeneration”. In: *Journal of neurophysiology* 105.5 (2011), pp. 2560–2571.

[133] Michael Telias et al. “Retinoic acid induces hyperactivity, and blocking its receptor unmasks light responses and augments vision in retinal degeneration”. In: *Neuron* 102.3 (2019), pp. 574–586.

[134] Michael Telias et al. “Retinoic acid inhibitors mitigate vision loss in a mouse model of retinal degeneration”. In: *Science advances* 8.11 (2022), eabm4643.

[135] Kevin J Cao et al. “Cyclodextrin-Assisted Delivery of Azobenzene Photoswitches for Uniform and Long-Term Restoration of Light Responses in Degenerated Retinas of Blind Mice”. In: *Advanced Therapeutics* 4.9 (2021), p. 2100127.

[136] Yusufu N Sulai and Alfredo Dubra. “Non-common path aberration correction in an adaptive optics scanning ophthalmoscope”. In: *Biomedical optics express* 5.9 (2014), pp. 3059–3073.

[137] Xiaojing Liu et al. “Effect of contact lens on optical coherence tomography imaging of rodent retina”. In: *Current eye research* 38.12 (2013), pp. 1235–1240.

[138] Wataru Ikeda, Tomoya Nakatani, and Akiyoshi Uemura. “Cataract-preventing contact lens for in vivo imaging of mouse retina”. In: *Biotechniques* 65.2 (2018), pp. 101–104.

[139] Matthias Kaschube. "Neural maps versus salt-and-pepper organization in visual cortex". In: *Current opinion in neurobiology* 24 (2014), pp. 95–102.

[140] Kenichi Ohki et al. "Highly ordered arrangement of single neurons in orientation pinwheels". In: *Nature* 442.7105 (2006), pp. 925–928.

[141] Ian Nauhaus et al. "Orthogonal micro-organization of orientation and spatial frequency in primate primary visual cortex". In: *Nature neuroscience* 15.12 (2012), pp. 1683–1690.

[142] Ye Li et al. "Clonally related visual cortical neurons show similar stimulus feature selectivity". In: *Nature* 486.7401 (2012), pp. 118–121.

[143] Satoru Kondo, Takashi Yoshida, and Kenichi Ohki. "Mixed functional microarchitectures for orientation selectivity in the mouse primary visual cortex". In: *Nature communications* 7.1 (2016), pp. 1–16.

[144] Stephen D Van Hooser et al. "Orientation selectivity without orientation maps in visual cortex of a highly visual mammal". In: *Journal of Neuroscience* 25.1 (2005), pp. 19–28.

[145] Vincent Bonin et al. "Local diversity and fine-scale organization of receptive fields in mouse visual cortex". In: *Journal of Neuroscience* 31.50 (2011), pp. 18506–18521.

[146] Andrew YY Tan et al. "Orientation selectivity of synaptic input to neurons in mouse and cat primary visual cortex". In: *Journal of Neuroscience* 31.34 (2011), pp. 12339–12350.

[147] Oleg Polyakov et al. "Passive mechanical forces control cell-shape change during Drosophila ventral furrow formation". In: *Biophysical journal* 107.4 (2014), pp. 998–1010.

[148] Linda Madisen et al. "A robust and high-throughput Cre reporting and characterization system for the whole mouse brain". In: *Nature neuroscience* 13.1 (2010), pp. 133–140.

[149] Simon P Peron et al. "A cellular resolution map of barrel cortex activity during tactile behavior". In: *Neuron* 86.3 (2015), pp. 783–799.

[150] Saskia EJ de Vries et al. "A large-scale standardized physiological survey reveals functional organization of the mouse visual cortex". In: *Nature neuroscience* 23.1 (2020), pp. 138–151.

[151] Pengcheng Zhou et al. "Efficient and accurate extraction of in vivo calcium signals from microendoscopic video data". In: *elife* 7 (2018), e28728.

[152] David H Brainard and Spatial Vision. "The psychophysics toolbox". In: *Spatial vision* 10.4 (1997), pp. 433–436.

[153] Zhongchao Tan et al. "Neuronal representation of ultraviolet visual stimuli in mouse primary visual cortex". In: *Scientific reports* 5.1 (2015), pp. 1–15.

[154] Matthew J McGinley et al. "Waking state: rapid variations modulate neural and behavioral responses". In: *Neuron* 87.6 (2015), pp. 1143–1161.

[155] Eftychios A Pnevmatikakis and Andrea Giovannucci. "NoRMCorre: An online algorithm for piecewise rigid motion correction of calcium imaging data". In: *Journal of neuroscience methods* 291 (2017), pp. 83–94.

[156] Eftychios A Pnevmatikakis et al. "Simultaneous denoising, deconvolution, and demixing of calcium imaging data". In: *Neuron* 89.2 (2016), pp. 285–299.

[157] Guanghan Meng. *High-throughput volumetric imaging of neural dynamics in vivo*. University of California, Berkeley, 2021.